Doctoral Dissertation
博士論文

Interferometer Locking Scheme for Advanced Gravitational-Wave Detectors and Beyond
(現在および将来の重力波検出器の干渉計の動作点引き込み法)

A Dissertation Submitted for the Degree of Doctor of Philosophy
December 2019
令和元年 12 月博士 (理学) 申請

Department of Physics, Graduate School of Science,
The University of Tokyo
東京大学大学院理学系研究科
物理学専攻

Yutaro Enomoto
榎本 雄太郎

Abstract

Direct observations of gravitational waves (GWs) by currently-operating ground-based interferometric detectors have brought unique astrophysical information, particularly on compact stars and gravity theories. It is expected that the planned detectors, namely the third generation detectors, which are about ten times more sensitive than the current detectors, will provide further information in these fields. Current GW detectors, such as Advanced LIGO, Advanced Virgo, and KAGRA, require multiply-coupled optical cavities to be controlled at their resonances. Thus the lock acquisition process, where all the cavities are brought to their operation points against the cross-coupling of the cavities, is essential for their operation and astrophysical observation. In particular, it is the most challenging to achieve the resonances of the arm cavities, because the kilometer-long arms result in narrow frequency linewidths; the arm cavity provides meaningful error signals only within its linewidth. In the third generation detectors, which will have longer arms leading to narrower linewidths, the lock acquisition process will be even more challenging. In lock acquisition of Advanced LIGO, a scheme called arm length stabilization (ALS) has been used, where auxiliary lasers having different wavelength from that of the main laser independently control the arms within their linewidths in a decoupled way. However, it is not trivial to scale up the system of Advanced LIGO to the third generation detectors due to the configuration of the system; optical fibers having the same length to the arms are involved, and thus to scale it up would increase optical phase noise and loss in the fibers.

To address this issue, a new type of the ALS system was designed for KAGRA. The new configuration is simple with significantly shorter fiber length and thus it is compatible with the third generation detectors. Along with a design study on the noise performance, an experimental test of the new ALS system was performed in KAGRA. The test revealed that the residual fluctuations of the arm cavities were evaluated to be less than 5 Hz in terms of root mean square, which are smaller than the linewidth of the arm. With this level of the noise performance, lock acquisition of the Fabry–Perot Michelson interferometer of KAGRA was achieved using the ALS system, which was the major milestone toward KAGRA joining the network observation. This achievement demonstrated that the system is ready for bringing the KAGRA full interferometer to the operation mode as soon as the other part of the interferometer is available.

Lock acquisition of third generation detectors was discussed for the first time. Utilizing the results obtained in KAGRA, the performance of the ALS system in third generation detectors was extrapolated. Necessary modifications to the

KAGRA ALS system were also discussed. The results indicated that lock acquisition of third generation detectors will be feasible by applying the KAGRA ALS system. We also point out that a new scheme with a sub-carrier field will make the lock acquisition process more reliable.

ACKNOWLEDGMENTS

This work has been supported by many people and groups. Here I would like to express my gratitude to them.

I am grateful to my supervisor Masaki Ando for his support. First of all, he accepted me as a graduate student when I changed the laboratory. He gave me freedom in research activities so that I could study what I want to study. His comments on my presentations always inspired me with something new.

I am also grateful to my former supervisor Seiji Kawamura. Thanks to him, I entered the field of gravitational-wave physics. He showed me how interesting this field is. His attitude for discussions with other people has been a guide to me. Discussions with him have been always fun to me.

I thank Kiwamu Izumi for his support and advice. He suggested that I worked in KAGRA and studied lock acquisition in the gravitational-wave detectors. He has always supported our experiments. His visit to the site always moved the experiments forward. It was my pleasure that I could work with him and learn from him; it has been precious time. Talks with him via phone calls were great help to me. He helped me improve the draft of the dissertation.

I also thank Yuta Michimura for his support and advice. It was the works on the main-interferometer simulation with him that made me decide to work on KAGRA. He supported our experiments, in particular in designing the main-interferometer setup and preparing necessary items. His attitude on research reminded me of importance of stopping once and thinking quantitatively. He gave me constructive comments to improve the draft of the dissertation.

I would like to also thank the following people for their tremendous supports.

Ryosuke Sugimoto and Kazuya Yokogawa worked with me on the implementation of the arm length stabilization system in KAGRA. My work could not be accomplished without their efforts. Together with Kiwamu, the realization of the system is the success of every single person of our team *All Green*. Thanks

to Masayuki Nakano, I started working in KAGRA back in 2015. I am sure that I could not have continued the research without him. He has been always my role model. His great effort enabled us to lock the Fabry–Perot Michelson interferometer. Takahiro Yamamoto greatly helped us with the interferometer commissioning work, which was indispensable to accomplish my work. He is literally the guardian of the control room. Takaaki Yokozawa supported me a lot. He kindly entered the mine with me even if it was only for turning on a single switch. I do not forget that he helped me to look for a "wanted" box throughout the mine for half a day.

Masatake Ohashi greatly supported our research activities. He flexibly made systems and rules to improve the working environment upon our frank requests. Yoshio Saito and Takashi Uchiyama arranged the schedule of the site work. Thanks to them, I was able to have time for my research. Yoshiki Moriwaki and Kazuhiro Yamamoto supported our work, especially in University of Toyama. Thanks to their support, I was able to perform preliminary measurements for fixing the experimental design. Moriwaki-sensei also made significant efforts on the preparation of the optical components.

Shinji Miyoki supported me a lot. It would not be possible without him to first lock the X arm cavity. His suggestion was always useful. I learned from him importance of trying something quickly without worrying it. Yoichi Aso and Osamu Miyakawa organized the commissioning team. Their suggestions taught me where to go. Keiko Kokeyama supported the work particularly from the input optics system. I learned from her that it is important to change setups for making progress without being afraid. Takayuki Tomaru supported the work particularly from the cryogenic suspension system. I was impressed by his speediness in experiments. Takafumi Ushiba also helped us also from the cryogenic suspension system. He gave me a fruitful suggestion also on schemes of wavelength conversion. Tomotada Akutsu supported the work from a variety of aspects. I learned basics of experiments from him such as importance of making a log entry and necessity of preparing items beforehand. Tatsuki Washimi gave me new knowledges. In particular, we were able to reduce the level of 60 Hz noise by a factor of more than ten thanks to his suggestion. Eiichi Hirose supported the work mainly from the point of the core optics. He gave me the information of the test mass coating for green. He also gave me comments on the power budget of the X arm. Kentaro Somiya shared interesting ideas with us, especially on quantum noise. Discussion with him was always interesting and stimulative to me. Ryutaro Takahashi, Ayaka Shoda, Mark A. Barton, Fabián Erasmo Peña Arellano, Lucia Trozzo, Koki Okutomi, Enzo Nicolás Tapia San Martin, Naoko

Ohishi, Naoatsu Hirata, and Naohisa Sato contributed the completion of room temperature suspensions for the optics. I could not perform any experiments in the KAGRA interferometer without their contributions. They also helped me with installing the steering mirror behind SR2. Thanks to the wrapper tools developed by Chihiro Kozakai, I managed to have easy access to past data of KAGRA. Shoichi Oshino supported our work, especially in maintaining and developing the digital control system. Darkhan Tuyenbayev supported the commissioning work from calibration. Other than that, I remember well that it was with him that we identified the issue of birefringence midnight in the mine.

Takahiro Miyamoto showed me the way of studying the KAGRA detector in the graduate course. I was impressed that a small component he had tested at Kashiwa was finally implemented as a part of the cryogenic suspension and it did really work at the KAGRA site. Kouseki Miyo helped me a lot. He kindly implemented the remote control interface for the signal generators. His imperturbable calm is always impressive to me. Yoshinori Fujii also helped me a lot. He always answered questions from me about the suspensions. I recall a lot of scenes with Kouseki and Yoshinori, as we started working (partially) at the site from the first year of the graduate course. Tomohiro Yamada has stimulated me, as he showed good results through his original work. I spent much time with Kohei Yamamoto in the life at the site. His vitality was always impressive to me. Dinner with him, Masayuki, and Gui-Guo Ge was always fun and good rest for me. Terrence Tak Lun Tsang helped me a lot through the suspension works. He was so smart and eager that he learned many new things rapidly, which was stimulative. Kenta Tanaka worked on the transmission monitor of the arm cavities. His preparation of the optics greatly contributed to the initial lock of the X arm.

Masahiro Kamiizumi, Tomonori Tomura, and Katsuhiko Shimode helped me very much from the point of analogue electronics. I probably asked them too much, but they responded with their best. Working on electronics with Shimode-san was one of the most interesting time for me. Mitsuharu Yoshimura supported our work a lot. Particularly, he laid many long coaxial cables and power supply cables used in our experiment. Seiji Furuta led the maintenance work of the mine. He always welcomed us with a smile at the entrance of the mine before and after the mine work. Kyoichi Takayama, Mihoko Okinaka, Yayoi Hara, Yukari Maeda, Miho Iwamatsu, and Eri Sakamoto greatly supported our work through the administration work. We could not do anything without their effort. I never forget the taste of the soup Okinaka-san made for us one day.

Stefan W. Ballmer was always impressive to me. The way he strongly pushed

the experiment forward was amazing. We could not close the DARM control loop without him. Koji Arai always gave me fruitful suggestions in the Interferometer Sensing and Control meetings. The modification plan of the radio-frequency photodetectors for the green PDH loops was entirely based on his suggestion. He also greatly helped me with improving a manuscript of a paper.

Kentaro Komori is very impressive to me. He is so smart that discussions with him are always fun. I was so impressed by his enthusiasm on experiments. Koji Nagano has been the closest colleague to me. His advice was always useful. He helped me to improve the draft of this dissertation. I was so lucky that I could work with him. Tomofumi Shimoda is so smart that what he pointed out often provided me with new insights. He also helped me to improve the draft. Kunihiko Hasegawa helped me through his unique knowledge on his field. He introduced me the chain curry restaurants, which I love now. Naoki Aritomi told us interesting updates from the filter cavity experiment, which has been very stimulative. Hiroki Takeda helped me through his knowledge on astronomical outputs of the gravitational-wave observations. Satoru Takano helped me when he visited the KAGRA site, to align the main interferometer beam to the X end. Takuya Kawasaki's knowledge and insight on quantum physics were impressive to me so that the discussion with him was fun. Ching Pin Ooi corrected my English writing, which was very helpful and easy to understand. Yuki Miyazaki greatly helped me with the initial experiment of the arm length stabilization last year, when he visited the KAGRA site. Naoki Kita also helped me with the initial alignment of the KAGRA beam, especially on the transmission monitor. Mayuko Niwata helped us with the office work. She kindly gave me advice when I could not decide my future direction.

Matteo Leonardi, Eleonora Capocasa, and Yuhang Zhao supported me when I visited their experiment, the filter cavity experiment. The experiences there were precious to me.

My simulation work relied on Matlab modules called Noise Budget. I thank the team led by Cristopher Wipf, who developed the modules.

Akito Kusaka, Masato Takita, Yuji Tachikawa, Takuro Ideguchi, and Hidetoshi Katori reviewed the dissertation. Their comments helped me to improve the dissertation.

I have been financially supported by ALPS (Advanced Leading Graduate Course for Photon Science) program in the University of Tokyo, and JSPS Fellowship DC1. This work was supported by MEXT, JSPS Leading-edge Research Infrastructure Program, JSPS Grant-in-Aid for Specially Promoted Research

26000005, JSPS Grant-in-Aid for Scientific Research on Innovative Areas 2905: JP17H06358, JP17H06361 and JP17H06364, JSPS Grant-in-Aid for JSPS Fellows 17J00973, JSPS Core-to-Core Program A. Advanced Research Networks, JSPS Grant-in-Aid for Scientific Research (S) 17H06133, the joint research program of the Institute for Cosmic Ray Research, University of Tokyo, National Research Foundation (NRF) and Computing Infrastructure Project of KISTI-GSDC in Korea, the LIGO project, and the Virgo project.

Finally, I sincerely thank my family for their understanding and continuous support. Thanks to them, I spent a happy time pursuing what I want to study. I do not know how I can express my gratitude.

CONTENTS

List of Figures xv

List of Tables xviii

Glossary xix

1 Introduction 1
1.1 Outline of the dissertation . . . 2

2 Gravitational Waves 3
2.1 Derivation . . . 3
2.2 Sources of gravitational waves . . . 5
2.2.1 Radiation of GWs . . . 6
2.2.2 Candidates . . . 7
2.3 Detecting gravitational waves . . . 8
2.3.1 Free mass motion under the presence of GWs . . . 8
2.3.2 Concept of GW detectors . . . 10

3 Gravitational-Wave Detector 11
3.1 Overview . . . 11
3.1.1 Laser interferometric detectors . . . 11
3.1.2 Resonant bar detectors . . . 13
3.1.3 Torsion bar detectors . . . 13
3.1.4 Atom interferometer . . . 14
3.1.5 Pulsar timing array . . . 14
3.2 Ground-based interferometric detectors and their noise sources . . . 14
3.2.1 Summary of the detectors . . . 14
3.2.2 Configuration . . . 15
3.2.3 Global detector network . . . 16

3.2.4 Fundamental noise sources . . . 17
3.3 Second generation detectors . . . 21
3.3.1 Science target . . . 21
3.3.2 Detectors . . . 22
3.3.3 KAGRA as the fourth detector in the network . . . 25
3.4 Third generation detectors . . . 25
3.4.1 Science target . . . 26
3.4.2 Detectors . . . 28

4 Interferometer **31**
4.1 Michelson interferometer . . . 31
4.1.1 Response . . . 31
4.1.2 Detection scheme . . . 33
4.1.3 Laser noise rejection . . . 36
4.2 Fabry–Perot cavity . . . 37
4.2.1 Response . . . 37
4.2.2 Detection scheme . . . 38
4.3 Dual-recycled Fabry–Perot Michelson interferometer . . . 41
4.3.1 Power recycling . . . 41
4.3.2 Resonant sideband extraction . . . 42
4.3.3 Detection scheme . . . 43
4.4 Advanced techniques . . . 44
4.4.1 Squeezed light injection . . . 44
4.4.2 Filter cavity . . . 45
4.4.3 Detuned RSE . . . 46
4.5 Challenges in the 3G detectors . . . 46
4.5.1 Long arms . . . 46
4.5.2 Weak actuators . . . 47

5 Lock Acquisition **49**
5.1 Overview . . . 49
5.2 Previous techniques . . . 52
5.2.1 Initial LIGO scheme . . . 52
5.2.2 Third harmonic demodulation technique . . . 52
5.2.3 Variable finesse technique . . . 53
5.3 ALS . . . 54
5.3.1 Necessity of ALS . . . 55
5.3.2 Requirements . . . 55

5.3.3 ALS in Advanced LIGO . . . 56

6 Configuration of KAGRA 59
6.1 Overview . . . 59
6.2 Optical configuration . . . 61
6.3 Control scheme . . . 65
6.4 Lock acquisition scheme . . . 66

7 KAGRA-Type ALS 69
7.1 Requirements . . . 69
7.2 Design . . . 70
7.2.1 Optical and servo topology . . . 71
7.2.2 Noise Design . . . 75
7.3 Implementation . . . 76
7.3.1 Control loops . . . 76
7.3.2 Optics . . . 79
7.3.3 Circuits . . . 84
7.4 Demonstration . . . 87
7.4.1 Interferometer setup . . . 89
7.4.2 The first scheme: direct transition from the ALS system . . . 89
7.4.3 The second scheme: transmission lock . . . 91
7.5 Characterization . . . 94
7.5.1 Sensing noise . . . 95
7.5.2 Actuator saturation . . . 101
7.6 Discussion . . . 101
7.6.1 Expected noise sources . . . 102
7.6.2 Doppler noise . . . 104
7.6.3 Air turbulence . . . 105

8 ALS in the Third Generation 107
8.1 Challenges . . . 107
8.2 Configuration . . . 108
8.2.1 Main interferometer parameters . . . 108
8.2.2 ALS configuration . . . 109
8.3 Noise estimation . . . 113
8.3.1 Methods . . . 113
8.3.2 Results . . . 114
8.4 Discussion: sub-carrier CARM locking as common path ALS . . . 117

9 Conclusion **123**
9.1 Summary of results . . . 123
9.2 Future prospects . . . 124
9.3 Conclusion . . . 125

A Spectral Analysis **127**

B Classical Control Theory **129**
B.1 Linear system . . . 129
B.2 Feedback loop and its stability . . . 130

C Fabry–Perot Cavity **133**

D Sideband Picture and Modulation **137**

E Quantum State of Light **139**
E.1 Vacuum state . . . 139
E.2 Coherent state . . . 140
E.3 Squeezed state . . . 141

F Preliminary Measurements **143**
F.1 Fiber phase noise measurement . . . 143
F.2 Measurements on the VCOs . . . 144
F.2.1 Actuation efficiency . . . 144
F.2.2 Frequency noise of the output signal . . . 146

G List of Devices **147**

Bibliography **151**

LIST OF FIGURES

2.1 Schematic view of how free test masses are moved by GWs 9

3.1 Laser interferometric detectors 12
3.2 Response functions of Michelson interferometers 15
3.3 Antenna pattern functions of an L-shaped detector to GWs in various polarization modes 16
3.4 Schematic sensitivity curves of typical GW telescopes 17
3.5 Transfer functions from seismic motion to the bottom of the pendula 18
3.6 Observation schedule and the approximate sensitivities of the 2G detectors 23
3.7 Sensitivities of the 2G detectors 24
3.8 Sensitivities of the 3G detectors 28

4.1 Schematic view of a Michelson interferometer 32
4.2 Schematic view of an optical layout for the balanced homodyne readout 35
4.3 Schematic diagram of a Fabry–Perot cavity 37
4.4 Response functions from GW strain to phase deviation of the output optical field in various interferometer configurations 39
4.5 PDH signal 40
4.6 Schematic diagram of a dual-recycled Fabry–Perot cavity 41
4.7 Conceptual diagram of how the ASD of strain-equivalent shot noise changes as the interferometer configuration changes 43
4.8 Schematic diagrams of how the squeezed vacuum is incorporated with the interferometer 45
4.9 Response transfer function of a cavity with the FSR of 3.75 kHz to the frequency fluctuations of input laser 47

4.10 Design sensitivities of the 2G and the 3G detectors in low frequency, in terms of displacement 48

5.1 Lock acquisition with and without ALS 51
5.2 Schematic diagrams of the lock acquisition of Initial LIGO 52
5.3 Schematic diagrams of the variable finesse technique 53
5.4 Conceptual diagram of ALS 55
5.5 Schematic view of the ALS system of LIGO 57
5.6 Schematic diagrams of the lock acquisition schemes with ALS . . 58

6.1 Schematic view of KAGRA 60
6.2 Picture and schematic view of a cryogenic payload 61
6.3 Optical configuration of KAGRA 62
6.4 Schematic view of the carrier and sideband fields and the detection ports 66

7.1 Schematic view of the ALS system of KAGRA 71
7.2 ASDs of the simulated noise spectra of the KAGRA ALS system . 74
7.3 Schematic diagram of the subcomponent loops of the system. . . . 77
7.4 Picture of the PSL table 80
7.5 Layout of the optics for the ALS system on the PSL table 80
7.6 Picture of the laid optical fibers 81
7.7 Configuration of the polarization Michelson interferometers for the cancellation of fiber noise 82
7.8 Layout of the optics for the ALS system on the POP table 83
7.9 Layout of the optics for the ALS system on the POS table 83
7.10 Pictures of in-vacuum steering mirrors behind PR2 and SR2 . . . 84
7.11 Conceptual diagram of the VCO circuit 86
7.12 Interferometer configuration for the demonstration of lock acquisition with the KAGRA ALS 87
7.13 Time series of the optical power at various detection ports during the first lock acquisition scheme 91
7.14 Time series of the optical power at various detection ports during the second lock acquisition scheme 93
7.15 ASDs of sensing noise of the ALS system 94
7.16 ASDs of sensing noise of the ALS system for the Y arm with and without the fiber noise cancellation loop engaged 96
7.17 Noise budget plot of sensing noise of the ALS system for ALS CARM 97

7.18 Doppler coupling of the longitudinal motion of PR2 99
7.19 ASD of the control signal of ALS DARM applied to the test mass actuators 100
7.20 Expected ASD of sensing noise of ALS CARM in the DRFPMI . 102

8.1 Possible configurations of the control of the auxiliary laser frequency 111
8.2 Expected ASDs of residual noise of CARM, $\Delta f_{\rm res}(f;\kappa_{\rm CARM})$, in the Cosmic-Explorer-like detector 115
8.3 Expected noise performance of the single arm ALS in the Cosimic-Explorer-like detector 117
8.4 Conceptual diagram of the hand-over of the CARM control as the last step of lock acquisition 118
8.5 Schematic diagram of the interferometer and control configuration for a reliable lock acquisition scheme 120
8.6 CARM resonance of the carrier and sideband fields in terms of the carrier frequency 121
8.7 Layout of the optics for the generation of the sub-carrier field . . 121
8.8 Noise budget plot of the sub-carrier scheme for the CARM control 122

B.1 Schematic diagram of linear systems 129
B.2 Nyquist plots and Bode plots 131

C.1 Schematic view of a Fabry–Perot cavity and associated electric fields 133
C.2 Optical power in a cavity and roundtrip phase 135

D.1 Modulation picture and sideband picture 138

E.1 Schematic diagram of quantum fluctuations of the vacuum state and a squeezed state 142

F.1 Picture of the experimental setup for the preliminary measurement of fiber phase noise 143
F.2 ASD of fiber frequency noise in the preliminary measurement . . . 144
F.3 Measured VCO responses to the input voltage 145
F.4 Setup for the measurement of the VCO frequency noise 145
F.5 Measured ASD of the output of the VCO 146

G.1 Picture of special modifications on the RF PDs for the arm PDH sensing 148

G.2 Top view of the prototype low noise VCO circuit 149

LIST OF TABLES

3.1 Summary of the ground-based interferometeric detectors 14

6.1 Design and measured values of the main interferometer parameters of KAGRA 64
6.3 Five length DoFs of a DRFPMI and their sensing signals 65

7.1 Main differences between the ALS systems of KAGRA and Advanced LIGO 70
7.2 Design of the control bandwidth of each loop of the system 75
7.3 List of major noise sources and assumed magnitude of them . . . 76
7.4 Comparison of the expected and achieved noise levels 103

8.1 Parameter set of the Cosmic-Explorer-like detector 108

G.1 List of devices (optics) 147
G.2 List of devices (opto-electronics) 148
G.3 List of devices (opto-mechanics) 149
G.4 List of devices (electronics) 149

GLOSSARY

Symbols

i	imaginary unit
c	speed of light
G	Newtonian constant of gravitation
h	Planck's constant
$\hbar$	Dirac's constant: $\hbar = h/2\pi$
k_{B}	Boltzmann constant
$M_{\odot}$	Solar mass
E	Electric field
$\mathcal{F}$	Cavity finesse
f	Fourier frequency
$h(t)$, $h(\Omega)$	Strain of gravitational waves
L	Arm length
P	Optical power
λ	Wavelength of light
Ω	Sideband or Fourier (angular) frequency
ω	Carrier (angular) frequency

Abbreviations

1G	First Generation
2G	Second Generation
3G	Third Generation
ASD	Amplitude Spectral Density
ALS	Arm Length Stabilization
AOM	Acousto-Optical Modulator
BBH	Binary Black Hole
BH	Black Hole
BNS	Binary Neutron Star
BS	Beam Splitter
DoF	Degree of Freedom
DRFPMI	Dual-Recycled Fabry–Perot Michelson Interferometer
DRMI	Dual-Recycled Michelson Interferometer
EOM	Electro-Optical Modulator
ETM	End Test Mass
FPMI	Fabry–Perot Michelson Interferometer
FSR	Free Spectral Range
GW	Gravitational Wave
IMC	Input Mode Cleaner
ITM	Input Test Mass
LO	Local Oscillator
NS	Neutron Star
OMC	Output Mode Cleaner
PD	Photodiode/Photodetector
PDH	Pound Drever Hall
PLL	Phase-Locked Loop
PMC	Pre-Mode Cleaner
PR	Power Recycling
PRFPMI	Power-Recycled Fabry–Perot Michelson Interferometer
PRM	Power Recycling Mirror
PSD	Power Spectral Density
PSL	Pre-Stabilized Laser
RF	Radio Frequency
RMS	Root Mean Square
RSE	Resonant Sideband Extraction

SHG	Second Harmonic Generation
SR	Signal Recycling
SRM	Signal Recycling Mirror
VCO	Voltage-Controlled Oscillator

Interferometer DoFs

DARM	Differential ARM length
CARM	Common ARM length
PRCL	Power Recycling Cavity Length
SRCL	Signal Recycling Cavity Length
MICH	MICHelson Length

Interferometer Sensing Ports

AS	Anti-Symmetric port
REFL	interferometer REFLection port
POP	Pick-Off port of Power recycling cavity
POS	Pick-Off port of Signal recycling cavity
TRX	TRansmission port of the X arm
TRY	TRansmission port of the Y arm

Chapter 1
INTRODUCTION

Gravitational waves (GWs) are space-time ripples traveling through the space-time, which were first predicted in General Relativity [1,2]. Since an object that is heavier and moves faster emits GWs more, it is thought that the observable GWs are sourced from astronomical or cosmological origin [3,4]. It is expected that direct observations of GWs reveal undiscovered nature of gravity theory, astronomy and cosmology in a unique way. In fact, the direct observations of GWs by terrestrial interferometric detectors have provided new discoveries [5,6]. Moreover, larger terrestrial detectors that are planned to be built in near future will reveal a lot of new insights on those fields [7,8].

The direct observations of GWs have revealed astronomical information such as the existence of binary black hole systems [5], and the heaviest stellar mass black hole ever [9,10]. Simultaneous observation of GWs and gamma rays indicated that the origin of a short gamma ray burst is a binary neutron star merger [11]. The observations have also set limits to gravity theories, such as speed of GWs [11]. In addition to these results, it is expected that the near-future larger GW detectors provide more; with their better sensitivities, they will be capable of, for example, identifying the equation of state of neutron stars [12,13], probing the mechanism of core-collapse supernovae [14,15], and setting more strict limits on gravity theories [16,17].

Modern GW detectors [18–20], which are sensitive enough to fulfill the scientific targets raised above, inevitably employ kilometer-long coupled optical cavities controlled with very sensitive but narrow-ranged interferometric sensors. Therefore, considering that the controls do not last arbitrarily long as they are occasionally broken by external disturbances, the process to somehow bring the interferometer of the GW detector to the operation point is essential in realizing the observation of GWs. Such a process is called interferometer locking or lock acquisition. Especially, deterministic and systematic lock acquisition is necessary

for stable long term observation. The most challenging part of lock acquisition is to control kilometer-long optical cavities. A scheme called arm length stabilization (ALS) plays an essential role in deterministically controlling the cavities in the lock acquisition sequence [21]. An ALS scheme utilizes auxiliary lasers to sense the cavity lengths. In the ALS scheme that has been used so far, the auxiliary lasers are injected to the interferometer from end stations, which are kilometer-away from the corner station, with a fraction of the main laser sent from the corner station to the end station via optical fibers [22]. Because of this feature, it is not clear if this scheme is scalable to longer-baseline GW detectors.

To address such an issue, a new ALS system that is scalable to such detectors has been designed and implemented for KAGRA, a GW detector soon to join the network observation [23] having key features important in the future detectors [24, 25]. In the dissertation, the detailed design and the implementation of the system are presented, and the experimental results in the performance tests of the ALS system are reported, where the Fabry–Perot Michelson interferometer of KAGRA was successfully locked. In addition, implications of the results on the future GW detectors are also discussed.

1.1 Outline of the dissertation

This dissertation is organized as follows. Chapter 2 summarizes the basic properties of GWs. Chapter 3 overviews GW detectors, instruments to observe GWs, focusing on ground-based interferometric GW detectors. Science outcomes of the current detectors and those of the detecters planned to be built in near future are also summarized. Chapter 4 describes principles and techniques of interferometry involved in the modern and future GW detectors. Chapter 5 reviews lock acquisition schemes in GW detectors. A scheme called ALS is introduced in particular, and its importance is clarified. Chapter 6 overviews the configuration of KAGRA focusing on its interferometer as the experimental setup where the new ALS scheme has been developed and demonstrated. Chapter 7 is the main part of the dissertation, which describes the design of the ALS system, its implementation, and the demonstrations and characterizations of its performance. Chapter 8 discusses the possible configuration and noise performance of the ALS system in the planned GW detectors, which can be inferred from the characterizations of the KAGRA ALS scheme. The necessary techniques in the future ALS scheme are also assessed. Chapter 9 summarizes the results, provides the future prospects, and finally concludes the dissertation.

Chapter 2
GRAVITATIONAL WAVES

Gravitational waves (GWs) are space-time ripples traveling through the space-time. The existence of GWs was first predicted by General Relativity of A. Einstein in 1916 [1,2], and was proven indirectly by the observation of the energy loss in a binary pulsar PSR B1913+16 by R. A. Hulse and J. H. Taylor [26, 27]. In 2015, two Advanced LIGO detectors detected a GW from a binary black hole merger [5], which marked the beginning of an era of GW astronomy. In this chapter, first the physics of GW is overviewed, then sources of GWs are summarized, and the method of the observation of GWs are briefly and conceptually explained.

2.1 Derivation

In this section, let us derive the expression of GWs, and how a test mass moves with GWs in the framework of General Relativity in four-dimensional space-time.

In General Relativity, our space-time is considered as a four-dimensional manifold with distance defined in such a way that the distance between two points x^μ and $x^\mu + dx^\mu$ can be expressed as

$$ds^2 = g_{\mu\nu}(x)dx^\mu dx^\nu. \tag{2.1}$$

Here and hereafter, Greek indices run from 0 to 3, and Einstein's convention is used. $g_{\mu\nu}(x)$ is the metric tensor of space-time. In General Relativity, the metric tensor $g_{\mu\nu}$ completely characterizes the geometry of the space-time, which is gravity.

The metric tensor satisfies the Einstein equation, which can be expressed as follows:

$$R_{\mu\nu} - \frac{1}{2}g_{\mu\nu}g^{\alpha\beta}R_{\alpha\beta} = \frac{8\pi G}{c^4}T_{\mu\nu}. \tag{2.2}$$

Here, c is the speed of light and G is the Newtonian gravitational constant. A tensor field $R_{\mu\nu}$ is referred to as Ricci tensor, which is defined in the following equations:

$$R_{\mu\nu} := R_{\mu\alpha\nu}{}^{\alpha}, \tag{2.3}$$

$$R_{\alpha\beta\gamma}{}^{\delta} := -\frac{\partial}{\partial x^{\alpha}}\Gamma^{\delta}{}_{\beta\gamma} + \frac{\partial}{\partial x^{\beta}}\Gamma^{\delta}{}_{\alpha\gamma} - \Gamma^{\delta}{}_{\alpha\mu}\Gamma^{\mu}{}_{\beta\gamma} + \Gamma^{\delta}{}_{\beta\mu}\Gamma^{\mu}{}_{\alpha\gamma}, \tag{2.4}$$

$$\Gamma^{\gamma}{}_{\alpha\beta} := \frac{1}{2}g^{\gamma\delta}\left(\frac{\partial}{\partial x^{\alpha}}g_{\beta\delta} + \frac{\partial}{\partial x^{\beta}}g_{\alpha\delta} - \frac{\partial}{\partial x^{\delta}}g_{\alpha\beta}\right). \tag{2.5}$$

Here $R_{\alpha\beta\gamma}{}^{\delta}$ is called as Riemann curvature tensor, and $\Gamma^{\gamma}{}_{\alpha\beta}$ is called connection coefficients or Chirstoffel symbols. $T_{\mu\nu}$ in the right-hand side of Equation (2.2) is the energy-momentum tensor, so it can be said that the Einstein equation (2.2) connects the energy and momentum in the space-time to the geometry of the space-time.

In Minkowski space-time, where the gravity does not exist, the space-time is flat in the sense that the metric of $\eta = \mathrm{diag}[-1, 1, 1, 1]$ can be used throughout the space-time. Here let us consider describing the Einstein equation in a perturbative way using the deviation from η, $h_{\mu\nu} := g_{\mu\nu}(x) - \eta_{\mu\nu}$. If we assume the gravity is sufficiently weak and consider only up to the first order of h, then Equation (2.2) can be simplified into the following:

$$-\eta^{\mu\nu}\frac{\partial^2\bar{h}_{\alpha\beta}}{\partial x^{\mu}\partial x^{\nu}} - \eta_{\alpha\beta}\frac{\partial^2\bar{h}^{\mu\nu}}{\partial x^{\mu}\partial x^{\nu}} + \frac{\partial^2\bar{h}^{\mu}_{\beta}}{\partial x^{\alpha}\partial x^{\mu}} + \frac{\partial^2\bar{h}^{\mu}_{\alpha}}{\partial x^{\beta}\partial x^{\mu}} = \frac{16\pi G}{c^4}T_{\alpha\beta}, \tag{2.6}$$

$$\bar{h}_{\alpha\beta} := h_{\alpha\beta} - \frac{1}{2}\eta_{\alpha\beta}\eta^{\mu\nu}h_{\mu\nu}. \tag{2.7}$$

Since it is well-known [3] that we can choose such a coordinate system that the Lorenz gauge condition

$$\frac{\partial}{\partial x^{\mu}}\bar{h}^{\mu\nu} = 0 \tag{2.8}$$

is satisfied, let us always impose the Lorenz gauge condition hereafter. Then Equation (2.6) turns to be

$$-\Box\bar{h}_{\alpha\beta} := -\eta^{\mu\nu}\frac{\partial^2\bar{h}_{\alpha\beta}}{\partial x^{\mu}\partial x^{\nu}} = \frac{16\pi G}{c^4}T_{\alpha\beta}. \tag{2.9}$$

This equation indicates that h, the deviation of the metric tensor from η, is sourced by the energy-momentum T and propagates as waves in the space-time, which shows the presence of the GWs.

To discuss the propagation of the GWs in a flat space-time, let us consider Equation (2.9) in vacuum ($T_{\alpha\beta} = 0$):

$$\Box \bar{h}_{\alpha\beta} = 0. \tag{2.10}$$

It is also known that there is a coordinate system that satisfies the transverse–traceless (TT) gauge conditions [4]:[‡1]

$$h_{0\alpha} = 0, \tag{2.11}$$
$$h^j_k = 0, \tag{2.12}$$
$$\frac{\partial h^{jk}}{\partial x^j} = 0. \tag{2.13}$$

Note $h_{\alpha\beta} = \bar{h}_{\alpha\beta}$, since $\eta^{\alpha\beta} h_{\alpha\beta} = 0$ holds in the TT gauge condition. Let us set $x^\mu = [ct,\, x,\, y,\, z]$, and consider GWs traveling in $+z$ direction. Then the solution of Equation (2.10) will be expressed by using two independent functions $h_+(t)$ and $h_\times(t)$ as follows:

$$h_{\alpha\beta} = \begin{bmatrix} 0 & 0 & 0 & 0 \\ 0 & h_+(t - \frac{z}{c}) & h_\times(t - \frac{z}{c}) & 0 \\ 0 & h_\times(t - \frac{z}{c}) & -h_+(t - \frac{z}{c}) & 0 \\ 0 & 0 & 0 & 0 \end{bmatrix}. \tag{2.14}$$

Here $h_+(t)$ and $h_\times(t)$ are called plus (+) mode and cross (×) mode, respectively. We now know that GWs in General Relativity propagate at the speed of light, and have two independent polarizations.

If General Relativity is not assumed, up to six independent polarizations of GWs can be considered [3], or the propagation speed of GWs can be different from c. Such deviations from General Relativity have been constrained to some extent by observation of GWs [11, 28].

2.2 Sources of gravitational waves

First the description of the radiation of GWs is explained, and then the interesting sources of GWs are introduced.

[‡1] Latin indices run from 1 to 3.

2.2.1 Radiation of GWs

Let us consider the radiation of GWs from a source having energy-momentum localized. Then the formal solution of Equation (2.9) is written as

$$\bar{h}^{\alpha\beta}(t,\boldsymbol{x}) = \frac{4G}{c^4}\int \frac{T^{\alpha\beta}(t-|\boldsymbol{x}-\boldsymbol{x'}|/c,\boldsymbol{x'})}{|\boldsymbol{x}-\boldsymbol{x'}|}d^3\boldsymbol{x'}. \tag{2.15}$$

Assuming the typical speed of the motion of the source is smaller than c and the distance between the observer and the source is larger than the wavelength of the GWs of interest, Equation (2.15) can be approximated as

$$\bar{h}^{\alpha\beta}(t,\boldsymbol{x}) \simeq \frac{4G}{c^4 r}\int T^{\alpha\beta}(t-r/c,\boldsymbol{x'})d^3\boldsymbol{x'}, \tag{2.16}$$

where r is the distance between the observer and the center of the source. Here, using the Lorenz gauge condition $\partial T^{\mu\nu}/\partial x^\mu = 0$,[‡2] the quadrupole formula

$$\bar{h}^{jk}(t,\boldsymbol{x}) \simeq \frac{2G}{c^4 r}\ddot{I}^{jk}(t-r/c) \tag{2.17}$$

is obtained, where

$$I^{jk}(t) := \int x^j x^k T^{00}(t,\boldsymbol{x})d^3\boldsymbol{x}. \tag{2.18}$$

In the TT gauge condition, these expression can be rewritten as

$$h^{\mathrm{TT}}_{jk}(t,\boldsymbol{x}) \simeq \frac{2G}{c^4 r}\ddot{I}^{\mathrm{TT}}_{jk}(t-r/c), \tag{2.19}$$

$$I^{\mathrm{TT}}_{jk} := P_{jl}I_{lm}P_{mk} - \frac{1}{2}P_{jk}P_{lm}I_{lm}, \tag{2.20}$$

$$P_{jk} := \delta_{jk} - \hat{n}_j\hat{n}_k. \tag{2.21}$$

Here $\hat{\boldsymbol{n}}$ is a unit vector pointing from the center of the source to the observer. Here it can be said that the lowest order radiation of GWs is quadrupole. Thus the GWs are radiated from the non-axisymmetric motions of mass. In addition, Equation (2.19) tells us that the higher speed motion of the heavier mass radiates the larger GWs. Therefore, the sources of the observable GWs are considered to be limited to the extreme astronomical or cosmological phenomena.

[‡2] Correct up to $O(h)$. This corresponds to the conservation of energy-momentum.

2.2.2 Candidates

Compact binary coalescence

The most promising sources of GWs are compact binary coalescences. Eleven GW detection events have been published up to now, and all of them were from compact binary coalescences. The first detection event and nine other events were originated in mergers of two orbiting black holes (BHs) [9]. These events have brought us information on binary synthesis [29–32]. The other published event of GW detection was from merging neutron stars (NSs) [6]. This event was also observed by follow-up observations in wide range of electromagnetic waves [33]. This event indicated that the origin of short gamma-ray bursts is the merger of two orbiting NSs [11,34], and also provided an implications on the origin of heavy metals [35]. The GW event from the merger of an NS and a BH is also expected, but have not been observed yet.

The frequency of GWs just before the merger can be approximately written as $f \sim 4.4\,\mathrm{kHz} \times (M_\odot/M)$ [36], where $M_\odot$ is solar mass, and M is the total mass of the binary. Thus the mass range of $M \sim 1 - 100\,M_\odot$ is the target of the ground-based GW detectors. The typical amplitude of the GWs observed on the Earth is considered as $h \sim 10^{-21}$. It is estimated that $\sim 1 - 50$ events of GWs can be detected in one year with the current sensitivity of the ground-based detectors [23].[‡3]

Supernova

Another interesting sources of GWs are core collapse of supernovae. If there is non-axisymmetric component in the core collapse, GWs would be emitted. The estimated amplitude of the GWs is $h \sim 10^{-22} - 10^{-21}$ seen from 10 kpc away from the source, and the typical frequency is considered to be $\sim 1\,\mathrm{kHz}$ [37]. If GWs from supernovae are observed, it would be unique information to access what happens inside the star when a supernova occurs.

Rotating neutron star

If there is non-axisymmetry in a rotating NS, it will emit GWs. Since the frequency of the emitted GWs is typically the double of the rotation frequency of the NS, fast rotating NSs including millisecond pulsars are the target of the ground-based detectors. The GW observations have imposed upper limits on

[‡3]Estimated sensitivity and period of Observation 3 (Figure 3.6).

ellipticity ε of known pulsars; $\varepsilon < 1 \times 10^{-5}$ with 95% credibility for Crab Pulsar, for example [38].

Merger of supermassive black holes

Merger of supermassive BHs may be regarded as an extreme case of compact binary coalescence. Although it has been known that there is a supermassive black hole ($M \sim 10^6 M_\odot$) in most galaxies, scenario of its formation has not yet been determined. It is expected that GWs around 1 mHz from mergers of supermassive BHs will provide indications to the scenario [39].

Cosmic gravitational wave background

If a number of GWs interfere with each other, their combination behaves as stochastic background. Among such GWs, cosmic GW background coming from quantum fluctuations during inflation is one of the most interesting targets [40]. Although the expected spectrum of such GWs is flat, it is key to choose an observational frequency band where the foreground GWs are removable.

2.3 Detecting gravitational waves

After summarizing how free mass moves as GWs come, the detection methods of GWs are conceptually explained.

2.3.1 Free mass motion under the presence of GWs

In General Relativity, the trajectory of a free mass is a geodesic, which means that the trajectory $x(\tau)$ satisfies the geodesic equation,

$$\frac{d^2 x^\mu}{d\tau^2} + \Gamma^\mu{}_{\alpha\beta}(x(\tau)) \frac{dx^\alpha}{d\tau} \frac{dx^\beta}{d\tau} = 0, \tag{2.22}$$

where τ is a parameter for the geodesic.

Hereafter, let us impose the TT gauge condition and chose time t as the parameter τ. In this condition, $x^\mu(t) = [ct, \boldsymbol{X}]$ satisfies Equation (2.22), where $\boldsymbol{X}$ is a set of three arbitrary real numbers. This fact indicates that we can place test masses whose spatial coordinates remain unchanged. Then let us consider how the distance between such two test masses changes in time under the presence of GWs. Here, for simplicity, let us consider a plane wave

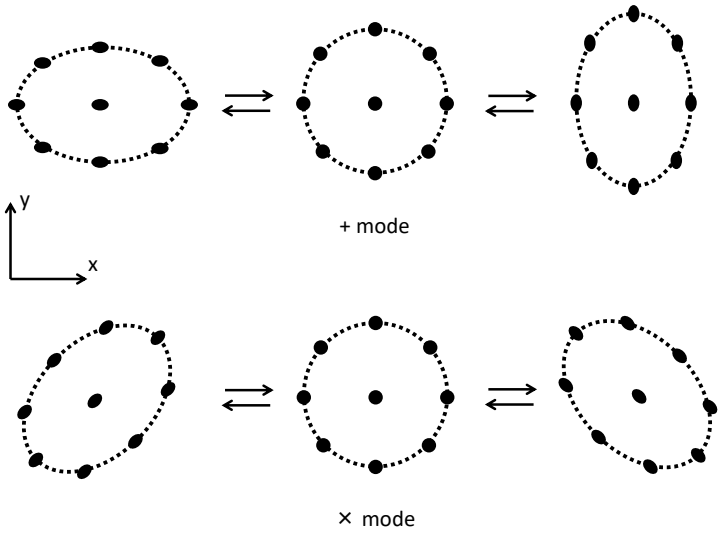

Figure 2.1: Schematic view of how free test masses on xy plane are moved by GWs traveling along z axis. It can be seen that the test masses tidally move.

with + polarization propagating in z direction, and test masses on xy plane $x^\mu(t;\theta) = [ct,\ R\cos\theta,\ R\sin\theta,\ 0]$ and $[ct, 0, 0, 0]$. Such GW can be modeled by setting $h_+(t) = h_p \cos \Omega t$, $h_\times(t) = 0$ in Equation (2.14). The spatial distance between two test masses can be calculated as follows:

$$\sqrt{g_{jk}x_j(t;\theta)x_k(t;\theta)} = R\sqrt{1 + h_p \cos 2\theta \cos \Omega t} \tag{2.23}$$

$$= R\left(1 + \frac{1}{2}h_p \cos 2\theta \cos \Omega t\right), \tag{2.24}$$

ignoring the second and higher order of h. Equation (2.24) shows that the test mass moves as shown in the upper half of Figure 2.1 with the GWs in + mode. Similarly, the motion of the test mass with GWs in × mode, $h_+(t) = 0\,, h_\times(t) = h_c \cos \Omega t$, can also be obtained:

$$\sqrt{g_{jk}x_j(t;\theta)x_k(t;\theta)} = R\left(1 + \frac{1}{2}h_c \sin 2\theta \cos \Omega t\right). \tag{2.25}$$

Equation (2.25) shows that the test mass moves as shown in the lower half of Figure 2.1 with the GWs in × mode.

2.3.2 Concept of GW detectors

As discussed in the previous subsection, the distance between free test masses changes with GWs. Therefore, GWs can be detected by measuring the distance between free test masses. One such realization of this idea is an interferometric GW detector, where the distance between two masses along x axis and that between two test masses along y axis are compared by using laser interferometry.

Chapter 3
GRAVITATIONAL WAVE DETECTOR

In this chapter, GW detectors are introduced focusing on ground-based interferometric GW detectors. First, various types of GW detectors are overviewed. Then ground-based interferometric detectors are introduced in detail. Next, the concrete GW detectors so called the second and third generation detectors are reviewed.

3.1 Overview

In this section, various kinds of GW detectors that are built or proposed so far are overviewed.

3.1.1 Laser interferometric detectors

In laser interferometric GW detectors, differential length change of the two arms is measured by using interference of laser light. The concept of laser interferometric GW detectors is shown in Figure 3.1. At both ends of each arm, mirrors are placed. They behave as test masses and move as GWs come. The laser interferometric GW detectors can be categorized into two: ground-based detectors and space-borne detectors.

Ground-based

Ground-based laser interferometric detectors have been developed most intensively, and they are the only detectors that really detected GWs so far [9]. Since

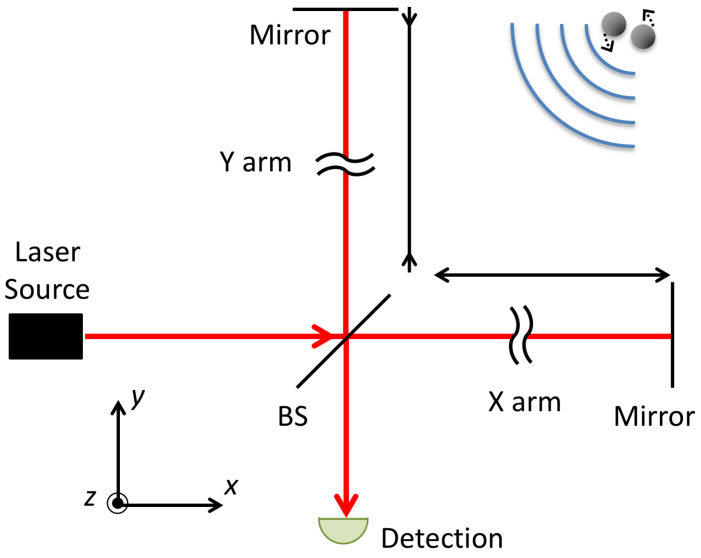

Figure 3.1: Conceptual view of laser interferometric GW detectors. As GWs arrive at the detector, one arm stretches while the other arm shrinks. The differential changes in the arm lengths are detected by using laser interferometric techniques.

it is not easy to have free test masses on the Earth, their test masses are suspended as pendula so that the test masses are regarded as free-falling for GWs in the frequencies above the resonant frequency of the pendula. In this scheme, in spite of the intensive effort to reduce the effect of seismic motion on the test masses, the target frequency of observation has been limited by $f \gtrsim 5-10\,\mathrm{Hz}$ [41]. Currently, detectors categorized in the second generation (2G) detectors such as Advanced LIGO, Advanced Virgo, and KAGRA are operating [23]. The third generation (3G) detectors having longer arms than those of the 2G detectors are also planned worldwide [7,8]. This scheme is described in more detail in the next subsection.

Space-borne

In contrast to the ground-based ones, it is rather easy to prepare free test masses in space. In addition, it is also easier to have long arm length. Utilizing these features, the target frequency band of the space-borne detectors is $\sim 1\,\mathrm{mHz} - 10\,\mathrm{Hz}$, which is lower than that of the ground-based ones. One major mission of

space-borne GW detectors is LISA [42]. The arm length of LISA is planned to be 2.5×10^9 m, and the target frequency band is $0.1 - 100$ mHz. The science target of LISA is mainly binary BHs. Since it is difficult to get laser beam back and forth in such a long arm, LISA adopts the optical transponder scheme, where the space craft receives laser light from the other edge of an arm, and inject laser that is phase-locked to the received laser light. Another major proposed mission of this category is DECIGO [43]. The arm length of DECIGO is planned to be 1×10^6 m, and the target frequency band is $0.1 - 10$ Hz. The science target of DECIGO is cosmic GW background from the inflation, as well as binary BHs and binary NSs. To reach such good sensitivity, it is planned that DECIGO uses optical configuration similar to that of ground-based ones, though it might be challenging to do in space.

3.1.2 Resonant bar detectors

In a local inertial frame, GWs can be treated as external force to act on masses [3]. The distance between two masses that are elastically connected to each other changes larger at the resonant frequency of this two mass system than other frequency. Resonant bar detectors are the realization of this idea; they are designed to be sensitive to GWs around their resonant frequency. The first experimental approach to directly detect GWs was a resonant bar detector by J. Weber [44]. The typical target frequency is typically a few kilohertz [45].

3.1.3 Torsion bar detectors

Due to the effect of seismic motion, it is not straightforward to have detectors on the Earth sensitive to GWs at frequency lower than $\sim 1 - 10$ Hz. One approach to have good sensitivity in such frequency region is to employ a torsion bar as a test mass. In this scheme, rotational motion of a torsion pendulum is used as a probe for GWs. Use of a torsion pendulum has an advantage that the resonant frequency of torsional motion can be much lower than that of translational motion with the same size of the suspension system, which means a torsion pendulum is superior to an ordinary pendulum in the attenuation of the seismic motion. A major experiment toward the realization of torsion bar detectors is TOBA experiment [46].

Table 3.1: Summary of the ground-based interferometeric detectors.

	1G	2G	3G
Detectors	TAMA300, Initial LIGO, Virgo, GEO600	Advanced LIGO, Advanced Virgo, KAGRA	Einstein Telescope, Cosmic Explorer
Year	1990's – 2010's	2010's – 2020's	2030's – 2040's
Sensitivity at 100 Hz $[/\sqrt{\text{Hz}}]$	$\sim 3 \times 10^{-23}$	$\sim 3 \times 10^{-24}$	$\sim 3 \times 10^{-25}$

3.1.4 Atom interferometer

Another approach to built detectors on the Earth sensitive in the low frequency region is to use atom interferometers. In this scheme, matter-wave interferometers of free-falling cold atoms serve as test masses to GWs, between which lasers propagate for measuring the distance [47]. There are projects to realize atom interferometric detectors such as MIGA [48] or ZAIGA [49]. There are also proposes to build atom interferometers in space such as AGIS [47] or AIGSO [50].

3.1.5 Pulsar timing array

In the pulsar timing array scheme, the strain of GWs is inferred from the change of the interval of the arrival of the pulsar signals from many known pulsars. The repetition rate of pulsar signals is so precise that it is expected that the repetition rate changes of pulsar signals caused by GWs can be detected [51]. The target frequency band of this scheme is $\sim 10^{-9} - 10^{-6}$ Hz [52].

3.2 Ground-based interferometric detectors and their noise sources

3.2.1 Summary of the detectors

Table 3.1 summarizes the past, present and future ground-based interferometric detectors. The detectors are commonly categorized into three generations. The first generation (1G) detectors have arm length of from several hundred meters to several kilometers. The 2G detectors have $3 - 4$ km arms. Advanced LIGO

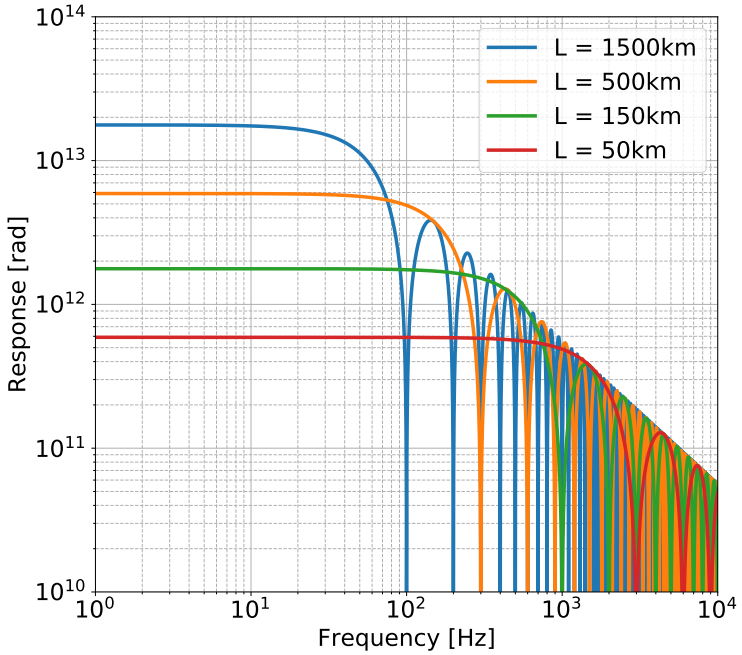

Figure 3.2: Response functions of Michelson interferometers with various arm lengths. The expression of the response function is given by Equation (4.9).

and Advanced Virgo utilize the infrastructure of the corresponding 1G detectors, while KAGRA has been built upon new infrastructure. The 3G detectors are planned to have $10 - 40$ km arms in new sites.

3.2.2 Configuration

The working principle of ground-based interferometric detectors is as simple as that of the Michelson interferometer (Figure 3.1). Each mirror forming the interferometer is suspended as a pendulum so that the mirror moves as a test mass as GWs pass through the detector. The motion of the mirrors caused by the GWs creates differential phase variations of the laser in the arms, and the Michelson interferometer converts them into variations of the laser power, which are then detected by photodetectors.

Figure 3.2 illustrates the detector response function from the strain of GWs to the measurable phase variations by the Michelson interferometer. It shows the responses of the Michelson interferometers that have several different arm lengths. This figure indicates two things. One is that longer arm length provides

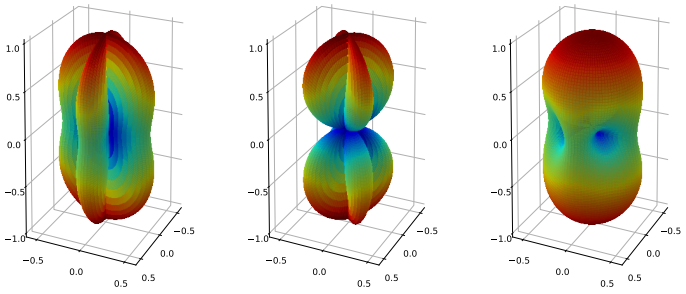

(a) + mode. (b) × mode. (c) Average.

Figure 3.3: Antenna pattern functions of an L-shaped detector to GWs in various polarization modes [4]. For each polarization, the distance from the origin measured in a certain direction depicts the magnitude of the response to GWs coming from the direction. The color of the surface also shows the distance. The response function is normalized so that the maximum response is equal to unity.

better response to the GWs in low frequencies. The other thing is that, for the GWs at a certain frequency f, the increase of the detector response saturates as the arm length reaches $c/4f$. This is because the phase change of the GWs themselves during the propagation of the laser in the arms becomes significant if the arm length is longer than $c/4f$. Therefore, to have a good sensitivity around 100 Hz, which is the current target band of the ground-based interferometric detectors, the arm length of ~ 500 km is required.

Since it is not realistic to achieve such long arm length on the Earth, the current detectors employ optical cavities to enhance the effective arm length [53]. Laser light propagates multiple roundtrips in the optical cavities so that the effective arm length is enhanced by the average number of roundtrips. The interferometer configuration including advanced interferometry is described in the next chapter.

3.2.3 Global detector network

For the ground-based GW detectors, global network observation with multiple detectors is essential. Coincident observation by two detectors is necessary to confidently claim the detected transients as GWs. Three detectors are needed to localize the source of the detected GWs. Figure 3.3 shows the response of a

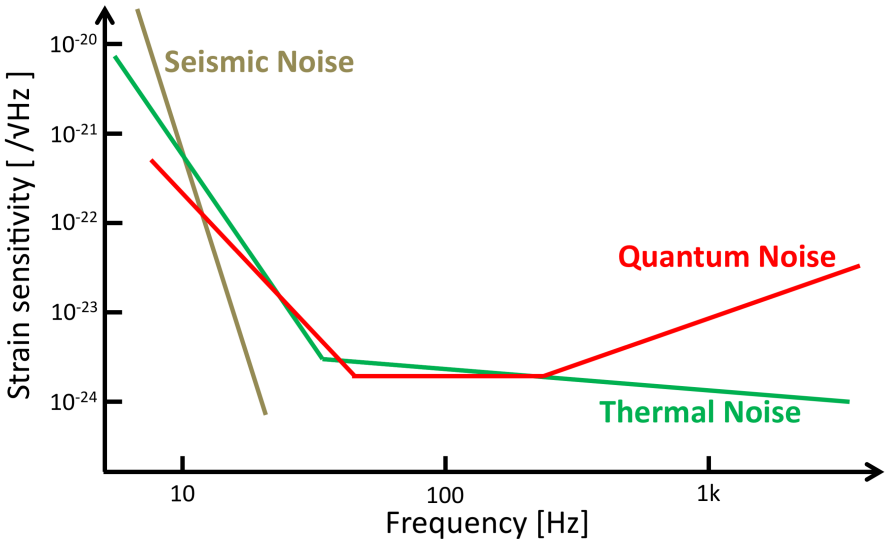

Figure 3.4: Schematic sensitivity curves (ASDs) of typical GW detectors. Contributions from the three fundamental noise sources are shown.

detector to GWs in a certain polarization from a certain direction. This indicates that it is not possible to localize the source of GW transients only by a single detector. The source is localized rather by differences in time of arrivals at multiple detectors. The four detector observation is essential in disentangling polarizations of GWs for the test of non-tensorial GWs [54]. In addition, the four detector network will increase the temporal and spatial coverage of the localizable GW events. In particular, smooth recovery of the operation mode of each detector via a reliable lock acquisition scheme helps improve the temporal coverage, namely the duty cycle.

3.2.4 Fundamental noise sources

Figure 3.4 conceptually shows typical noise spectrum of the ground-based interferometer. The magnitude of the stationary noise is described by the power spectral density (PSD) in the frequency domain (Appendix A). In the field of GW detection, the amplitude spectral density (ASD), which is the square root of the PSD, is also used for the description of the noise level. Each fundamental noise source is described in the following subsection.

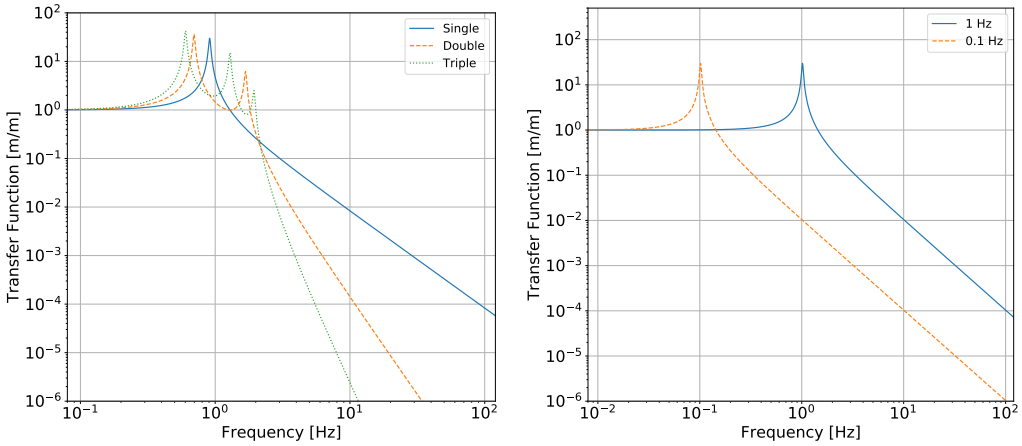

(a) (b)

Figure 3.5: Transfer functions from seismic motion to the bottom of the pendula. (a) How the attenuation function changes as the number of pendulum stages increases. (b) How the attenuation function changes as the resonant frequency of the pendulum decreases.

Seismic noise

Since the detectors are built on the Earth, vibrations of the test mass mirrors introduced from the seismic motion are inevitable. To attenuate the effect of the seismic motion on the test masses, multi-stage pendula are employed. Figure 3.5 shows the transfer functions from the ground motion to the bottom stage of a multi-stage pendulum, with different number of stages or with different resonant frequencies. This figure illustrates that use of multi-stage pendula and having low resonant frequencies effectively increases the attenuation factor. To have pendula with low resonant frequencies with limited space, spring-antispring systems are employed such as an inverted pendulum [55] for horizontal motion or a geometric antispring filter [56] for vertical motion. Another approach is to reduce the seismic motion itself; building the whole detector underground with stable bedrock also helps to improve the seismic noise [24].

Seismic noise is a dominant noise source below $\sim$ 10 Hz, because seismic motion itself is larger at low frequencies and it is rather difficult to have large seismic attenuation there. Apart from the sensitivity point of view, having a good seismic attenuation is essential for the detectors, since it helps the stability of the detectors and the reliability of the lock acquisition process of the interferometer.

Thermal noise

Thermal noise is thermal motion of the center of mass and/or the reflection surface of test mass mirrors having finite temperature.[‡1] According to the fluctuation-dissipation theorem, the PSD of the thermal noise $S_x(f)$ is expressed as

$$S_x(f) = -\frac{4k_{\mathrm{B}}T}{(2\pi f)}\,\mathrm{Im}[H(2\pi f)], \tag{3.1}$$

where k_{B} is the Boltzmann constant, T is the temperature of the thermal bath of interest, H is the transfer function from the force (that is conjugate to the displacement x) to the displacement x, and f is the temporal frequency of the motion. In the Levin's reciprocal approach [58], the PSD is also described in a more generic way as

$$S_x(f) = -\frac{8k_{\mathrm{B}}}{(2\pi f)^2}\sum_i \frac{T_i W_{\mathrm{diss},i}}{F_0^2}, \tag{3.2}$$

where F_0 is the amplitude of an imaginary sinusoidal test force having the same distribution as that of the laser beam for the sensing of the displacement, T_i is the temperature of each thermal bath, and $W_{\mathrm{diss},i}$ is energy loss per unit time to the thermal bath labeled as i under the condition where the imaginary force is applied to the test mass. This formula is also applicable to the case where the test mass is connected to multiple thermal baths having different temperature [59].

Let us discuss thermal noise of a single pendulum system as an example, where the system dynamics is characterized by the transfer function

$$H(2\pi f) = \frac{1}{m(2\pi)^2\left[f_0^2(1+i\phi(f)) - f^2\right]}. \tag{3.3}$$

Substituting it into Equation (3.1) leads to the the following PSD,

$$S_x(f) = \frac{4k_{\mathrm{B}}T}{m(2\pi)^3 f}\,\frac{f_0^2\phi(f)}{\left(f^2 - f_0^2\right)^2 + f_0^4\phi^2(f)}. \tag{3.4}$$

This equation indicates that smaller $\phi(f)$ leads to better thermal noise except for the frequencies around f_0. $\phi(f)$ is called loss angle, which characterizes the energy dissipation of the oscillator. Heavier mass m also leads to better thermal noise.

[‡1] Even if the test mass mirrors and their suspensions are at zero temperature, they move at the level of zero point fluctuations. The zero point fluctuations and the thermal noise can be described in the same frame work [57].

According to Equation (3.4), it is necessary to use mirrors (including optical coatings on them) and their suspensions with low mechanical loss, in order to have good floor level of the thermal noise spectra. In fact, Advanced LIGO employs monolithic fused silica for the test masses and their suspension fibers of the bottom stage, to reduce the mechanical loss. KAGRA adopts sapphire for the test masses and their suspension fibers of the bottom stage, because sapphire is known to have low mechanical loss at cryogenic temperatures. It is also obvious in Equation (3.4) that lowering the temperature of the test mass reduces thermal noise [60]. KAGRA cools its test masses down to $\sim 20\,\mathrm{K}$. The 3G detectors such as Einstein Telescope and Cosmic Explorer also plan to use cryogenic mirrors [7,8]. Thermal noise is a dominant noise source around 100 Hz, where the detectors have the highest sensitivity to the GW strain.

Quantum noise

Since laser interferometric GW detectors utilize interference of laser light, quantum fluctuations of electromagnetic field become a noise source. Such noise is called quantum noise. In simple interferometer configurations,[‡2] quantum noise can be split into two kinds: shot noise and quantum radiation pressure noise.

Shot noise is sensing noise coming from photon number fluctuations at the photon detection. Let us discuss its dependence on the input laser power to the detector. Since laser interferometric GW detectors linearly convert GWs into laser power fluctuations detected by photodiodes, the signal strength is proportional to the input laser power to the interferometer, P_0. The standard deviation of photon number fluctuations is proportional to $\sqrt{N}$ and then $\sqrt{P_0}$,[‡3] where N is the number of photons detected by photodiodes. Therefore, signal-to-noise ratio of the shot noise is proportional to $\sqrt{P_0}$, so that using high power laser is essential. Shot noise limits the sensitivity in the frequency region where $f \gtrsim 100\,\mathrm{Hz}$ [18, 20, 61].

Radiation pressure noise arises from fluctuating displacement of the test mass mirrors caused by quantum fluctuations of radiation pressure of laser photons. As mentioned above, the standard deviation of photon number fluctuations, and thus radiation pressure fluctuations, is proportional to the square root of the laser power so that the displacement of the radiation pressure noise is proportional to $\sqrt{P_0}/mf^2$. Here we used the fact that the test mass response to the external

[‡2] Unless advanced interferometric techniques that produce quantum correlation between sensing noise and backaction noise are used.

[‡3] As long as the laser light is Poissonian.

force is written as $-1/m(2\pi f)^2$ if the mass can be treated as a free-falling mass, where m is mass. Therefore lowering the input laser power P_0 and/or having heavy test masses m can reduce the radiation pressure noise. Radiation pressure noise is one of the dominant noise sources in $\sim 10 - 100\,\mathrm{Hz}$ [18, 20, 61].

From the above discussions, it is clear that shot noise and radiation pressure noise have inverse dependence on the laser power. This trade-off relation is a consequence of the Heisenberg's Uncertainty Principle. It leads to the standard quantum limit of the quantum noise level [62], which cannot be beaten without quantum nondemolition measurement schemes. Recently, experimental realization and practical implementation of measurement schemes to beat the standard quantum limit have been intensively developed [63–68]. From the theory side, more fundamental limit beyond the standard quantum limit is investigated from the perspective of quantum information [69, 70].

3.3 Second generation detectors

Advanced LIGO, Advanced Virgo and KAGRA, which are categorized in the 2G GW detectors, are currently operating. They have the following features: their arm length reaches $3 - 4\,\mathrm{km}$, and their best strain sensitivity approaches $\sim 10^{-24}/\sqrt{\mathrm{Hz}}$ around 100 Hz [18, 20, 61]. This sensitivity level can be described as follows: with this sensitivity, GWs from merging binary black holes (BBHs) and binary neutron stars (BNSs) can be detected with a reasonable rate [23]. In this section, the science target of the 2G detectors are overviewed, and then the features of each 2G detector are introduced.

3.3.1 Science target

Direct observation of GWs

The primary target of the 2G detectors was to directly detect GWs for the first time. It has been important not only because it would be the first direct proof of existence of GWs but because it opens a new window to observe astronomical objects, particularly objects in strong gravity field. In fact, the BHs of GW150914 were larger than any other stellar mass BHs that had ever been reported [10]. Direct observation of BBH mergers has enabled us to obtain the information of BH formation and binary evolution [29, 30], though accumulated statistics is not enough yet. It has also made it possible to test General Relativity using a perturbed BH, which is a remnant of a BBH merger [71, 72], though the sensitivity

is not enough yet.

Multi-messenger observation of compact binary coalescence

Another target is to observe GW transients along with electromagnetic (and neutrino) observatories. GW170817, the first GW event of BNS merger, was associated with many electromagnetic follow-up observations at different wavelengths [6, 33], which provided rich scientific information. Two notable results are the following. (1) Short gamma ray burst (GRB170817A) was observed with a time delay of $\sim 1.7\,\mathrm{s}$ with respect to the merger time, which supports the theory that short gamma ray bursts follow binary neutron star mergers [11]. This simultaneous detection of GWs and gamma ray also set a limit to difference of the propagation speed of GWs and electromagnetic waves [11]. (2) A set of optical and infrared (and also ultraviolet) telescopes observed optical and infrared transients (kilonova) from the volume localized by the GW detection [33]. It indicates that a kilonova comes from the radioactive decay of r-process nuclei synthesized in the ejecta of the merger. This observation is consistent with the theory that heavy metals in our Galaxy were synthesized at the BNS mergers [73–75]. Since optical observations identified the host galaxy (NGC4993), it provided a new independent method to infer the Hubble constant, by combining the luminosity distance inferred from the GWs of the merger and the redshift of the host galaxy [76, 77].

3.3.2 Detectors

Figure 3.6 shows past and near future schedule of the observations and the approximate sensitivity of each detectors at each observation period. Here the features of them are explained.

Common features

Common features among the 2G detectors can be listed as follow:

- the design sensitivity reaches as high as $\gtrsim 100\,\mathrm{Mpc}$ in terms of BNS merger detection range,
- the arm length is $\sim 3 - 4\,\mathrm{km}$,
- input laser power is on the order of $100\,\mathrm{W}$ at maximum,

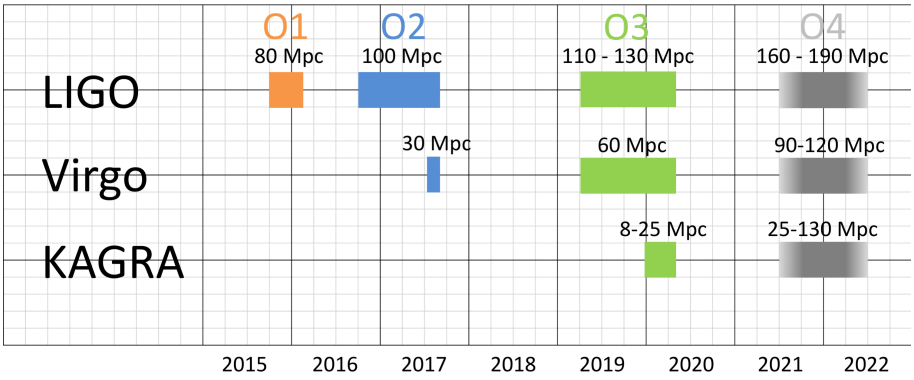

Figure 3.6: Observation schedule and the approximate sensitivities of the 2G detectors.

- interferometer configuration is so-called *Dual-Recycled Fabry–Perot Michelson Interferometer* (DRFPMI; see Chapter 4).

Advanced LIGO

Advanced LIGO has two identical detectors at Hanford in Washington and Livingston in Louisiana in the U.S. [18]. They were built on the infrastructure of Initial LIGO [81,82]. The third LIGO detector, LIGO India, is also planned [83] and approved [84]. The design sensitivity of Advanced LIGO is shown in Figure 3.7. Two Advanced LIGO detectors detected the first GW event, GW150914, to mark the beginning of an era of GW astronomy in the period of Observation 1 (O1). The arm length is approximately 4 km. Each test mass and its suspension wire are made of fused silica and the weight of the mass is 40 kg. The world's best sensitivity so far in terms of the BNS merger detection range was recorded by the Livingston Observatory, which is ~ 140 Mpc [85].

Advanced Virgo

Advanced Virgo detector is built at Pisa in Italy [61], utilizing the infrastructure of the initial version of Virgo detector [86]. The design sensitivity of Advanced Virgo is shown in Figure 3.7. Advanced Virgo joined the network observation at the late stage of Observation 2 (O2), and detected several compact binary coalescence events including the first BNS merger, GW170817 [9]. It is notable that localization of the BNS with the three detector network made it possible for

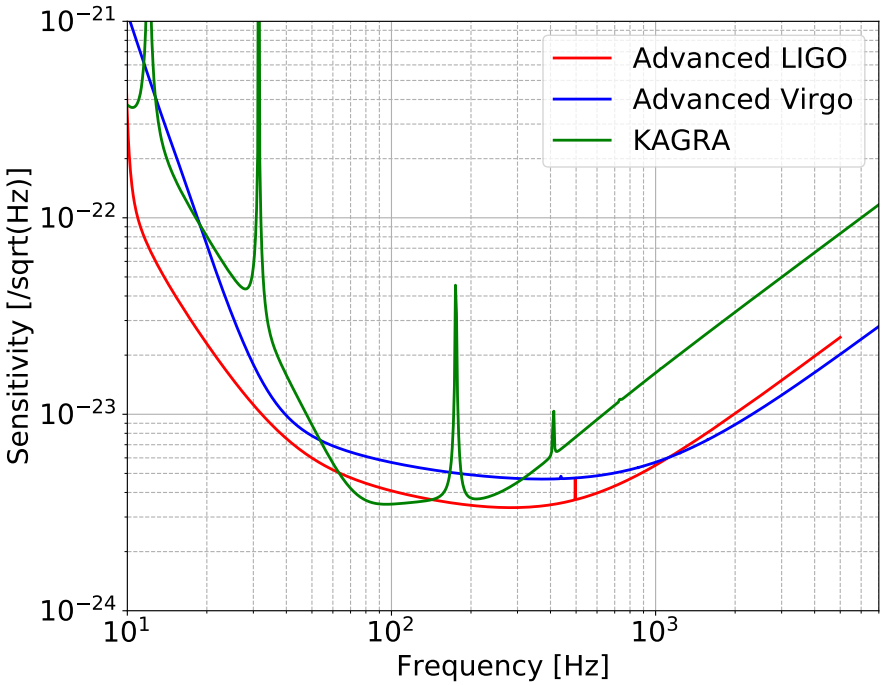

Figure 3.7: Sensitivities of the 2G detectors [23, 78–80].

optical telescopes to survey almost all the potential transients in the localized sky region [87]. The arm length is 3 km. Each test mass and its suspension wire are made of fused silica and the weight of the mass is 42 kg.

KAGRA

KAGRA is built in the underground tunnel at Kamioka in Japan, in a newly built infrastructure [24]. The design sensitivity of KAGRA is shown in Figure 3.7. KAGRA plans to join the network as the fourth detector at the last stage of Observation 3 (O3). It is expected that KAGRA joining the network enables us to increase the network duty cycle, to improve the sky coverage of the localizable sources of GWs [23, 88], and to disentangle polarizations of GWs [54]. KAGRA has two unique features in its detector itself. One is that the detector is built underground [20, 24]. The other is that the key components, test masses are cooled down to cryogenic temperature [20, 25]. These features will be of great importance for the 3G detectors [8, 89]. KAGRA has its own importance not only as one detector of the four-detector network but also as a test bed to accumulate

knowledges and experiences for the future detectors. The arm length is 3 km. Each test mass and its suspension wire are made of crystalline sapphire and the weight of the mass is 23 kg. The test mass is cooled down to 20 K.

3.3.3 KAGRA as the fourth detector in the network

Let us here focus on the scientific importance of KAGRA joining the network observation as the fourth detector. The fourth detector is considered to improve temporal and spatial coverage of localizable events as explained below.

Network duty cycle can be used to quantify the contribution of the fourth detector to the temporal coverage. Let us compare the ratio of time when three or more detectors are operating in the following simplified cases: (i) there are three detectors and each detector has the duty cycle of 75 %, and (ii) there are four detectors and each detector has the duty cycle of 75 %. The ratio of time with three or more detectors online can be given by straightforward calculations: (i) 42 % and (ii) 74 %. It is worth noting here that the duty cycle of the single detector was $\sim 70 - 80$ % and the three-detector duty cycle was 44 % in the early stage of O3 [90]. These numbers are close to the outcome of the simple consideration. Therefore, it is expected that the temporal coverage will be improved by ~ 1.7, by comparing the results of (i) and (ii).

Adding the fourth detector will also improve the spatial coverage. Simulation works revealed that KAGRA joining the network as the fourth detector improve the sky localization by more than $\sim$ 15 % for half of all the compact binary coalescence events even if the sensitivity of KAGRA is limited [91].

3.4 Third generation detectors

The 3G detectors are the planned GW detectors which will be online from 2030's [92, 93]. The planned arm length is on the order of 10 km. They will have approximately 10 times better sensitivity than those of the 2G detectors. Better sensitivity will provide benefits in two ways. One is the number of detectable events. A naive discussion tells us that N times better strain sensitivity leads to N^3 times more statistics. The other is the maximum signal-to-noise ratio of the GW increases by a factor of N with an N times more sensitive detector. With such detectors, fruitful science outcomes are expected as summarized below. In this section, the science target of the 3G detectors are overviewed, and then the planned detectors are also introduced.

3.4.1 Science target

Neutron star physics

How matter in a neutron star behaves still remains unknown; the equation of state, the relation between mass and radius, or the maximum mass are not yet understood well. It is of great importance to investigate them because they convey the information of how matter behaves under the extreme condition of high pressure, high density, strong gravity, and strong magnetic field. It is predicted that they are encoded in the GWs both from late inspiral of BNS mergers and from a remnant of BNS mergers. As each NS comes close to each other in the late inspiral phase, the tidal deformation affects the orbit evolution and thus modulates the emitted GWs [13, 94]. From the waveform of GW170817, some constraints were set to tidal deformability (a dimensionless parameter characterizing the deformation) of the NSs [95]. With the 3G detectors, it is expected that the tidal deformability will be clearly measurable and so strong constraints will be set that a significant fraction of the proposed equations of state will be ruled out [12, 13]. After the merger of a BNS, a massive NS can be formed in an excited state, which will then emit quasiperiodic GWs. It has been reported that the characteristic frequency of such GWs depends on the equation of state [96]. From the numerical simulations, its dependency can be approximately expressed as

$$f \sim 4.0\,\mathrm{kHz} \times \left(\frac{R_{1.8} - 2\,\mathrm{km}}{8\,\mathrm{km}} \right) \tag{3.5}$$

for a massive neutron star formed from a BNS with its total mass equal to $2.7 M_{\odot}$, where $R_{1.8}$ denotes radius of an NS for given equations of state. With 3G detectors operating for a year, radius of an NS may be determined within $\lesssim 100\,\mathrm{m}$, which is smaller than systematic errors in theoretical modeling [97].

Supernovae mechanism

The mechanism of supernovae remains unknown mainly because of two reasons; it is difficult to fully simulate the explosion and the core cannot be accessed with electromagnetic waves. It is expected that core-collapse supernovae may produce detectable GWs [14]. It is also expected that the 2G detectors could detect GWs from core-collapse supernovae, but the expected rate is very low. Thus the 3G detectors may be needed to detect such GWs for the first time [15]. With 3G detectors, we can expect one event in a few years, and we can also expect that, from the detected signals, g-mode excitation of proto-neutron star formed at the

core may be probed and signs of the convection or the standing accretion shock instability may be caught resulting in constraining the supernova models [15].

Test of General Relativity

General Relativity has been one of the fundamental laws of the Universe for more than one hundred years as no deviations from it has been found. One of the direct ways to observe such deviations in strong gravity regime is to probe BH perturbations with GWs. A remnant of a merged BBH is damped by emitting GWs, which can be modeled by quasi-normal modes of a Kerr BH. According to General Relativity, a BH is characterized only by the mass and spin,[‡4] and so are the frequency and damping rate of quasi-normal modes. GWs from the quasi-normal modes were detected from the post-merger phase of GW150914 [72]. With the 3G detectors, the deviations in the frequency and the damping rate will be detectable within a few percent, to set constraints on gravity theories [16].

Another way to test General Relativity is to search for extra polarizations in propagating GWs, since General Relativity predicts only two tensor polarizations while general metric theories allow six polarizations [98, 99]. It is also expected that the existence of nontensorial polarization modes of GW may be tested with the 3G detectors [17].

Standard siren measurement

Since there has been discrepancy in the reported values of the Hubble constant, one is from spatial spectrum of the CMB temperature fluctuations [100] and the other is from the observation of type Ia supernovae [101], it is important to have another independent method to obtain the Hubble constant. A GW standard siren measurement is one such candidate [102]; the luminosity distance of compact binary coalescence can be inferred from its inspiral signals and thus the Hubble constant can be obtained by combining the redshift of the source. In fact, the Hubble constant was measured to be $70.0^{+12.0}_{-8.0}$ km/c/Mpc by using GW170817 and the redshift of the identified host galaxy [76], though the precision was not high enough to resolve the discrepancy. With the 3G detectors, it is expected not only that the Hubble constant can be determined with enough precision but also that the evolution history of the Universe can be precisely measured [103–105] since the 3G detectors can detect binary coalescence at high redshift as mentioned below.

[‡4]Electric charge is ignored here since astronomical BHs are considered to be neutral.

Population of compact binary systems

Since the targeted sensitivity of the 3G detectors is good even at low frequencies ($\sim 10\,\mathrm{Hz}$), it is expected that they are capable of detecting GWs from compact binary coalescence with high signal-to-noise ratio all across the history of the Universe (redshift $z \gtrsim 10$) [8, 89, 93]. With this ability of the detectors, the complete population of stellar-mass BHs from the era of first stars to the present time will be revealed. They will also be able to probe how the BBH merger rate and the underlying star formation rate have evolved from the early Universe, through the observations of BBH mergers providing the inference of their masses and spins.

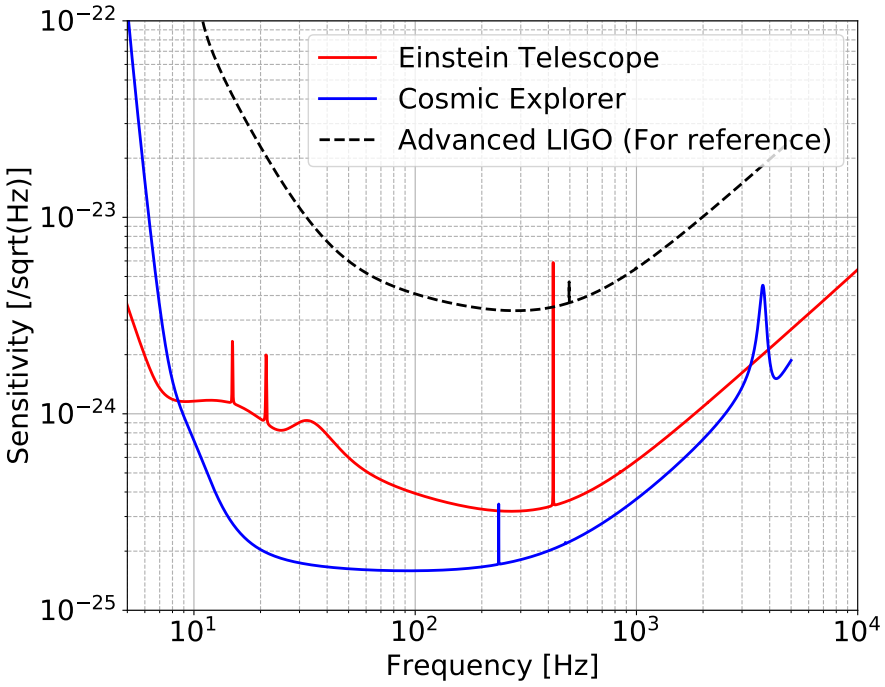

Figure 3.8: Sensitivities of the 3G detectors [7, 8, 106].

3.4.2 Detectors

There are two major projects of the 3G detectors, Einstein Telescope [7] and Cosmic Explorer [8, 93]. The sensitivity of each detector reaches below $10^{-24}\,/\sqrt{\mathrm{Hz}}$. The sensitivity curves are shown in Figure 3.8.

The characteristic of each detector can be overviewed as follows. The arm length of Einstein Telescope is 10 km. A unique feature of Einstein Telescope is its xylophone design, which employs one detector specialized for low frequency GWs and the other for high frequency GWs. The test masses of the low frequency detectors will be cooled down to cryogenic temperature. The detectors will be built in a triangular-shape underground tunnel that houses three pairs of the xylophones [89].

Cosmic Explorer will be an L-shaped detector with the arm length of 40 km. The project will be split into two stages. The first stage adopts room temperature fused silica test masses. In the second one, cryogenic silicon will be used as test masses for better thermal noise performance and better capability of storing high power laser in arm cavities [93].

Chapter 4
INTERFEROMETER

In this chapter, basic interferometric methods and techniques that are or will be implemented in the 2G and/or 3G detectors are summarized. They are indispensable to reach the targeted sensitivity of each detector. Since they make the interferometer of the GW detector complicated, it becomes important to study lock acquisition processes of the interferometer. In the last section, expected technical challenges in the 3G interferometers are overviewed.

4.1 Michelson interferometer

4.1.1 Response

Let us consider the response of a Michelson interferometer as shown in Figure 4.1 to GWs, $h(t)$, propagating along z axis. Let us assume each mirror moves as a free mass, and the beam splitter (BS) has split ratio of 50:50. Let us denote the distance between the BS and each end mirror in the x or y direction by L_x or L_y, respectively. Let us define L by $L = (L_x + L_y)/2$. According to Equation (2.1), the relation

$$\frac{dx}{dt} \simeq \pm c \left(1 - \frac{1}{2}h(t)\right) \tag{4.1}$$

holds. Therefore, the duration $T_x(t)$ it takes for the laser light to propagate in the x arm in a roundtrip way can be described by[‡1]

[‡1] Assuming $|L_x - L_y|/L \ll 1$, L is used for the interval instead of L_x.

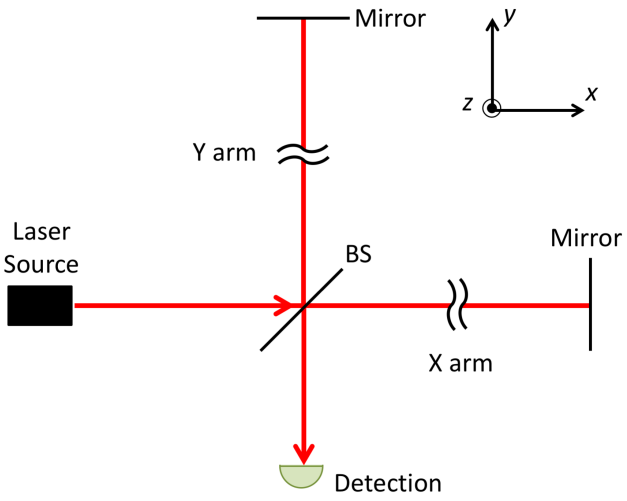

Figure 4.1: Schematic view of a Michelson interferometer.

$$T_x(t) = \int_{\text{roundtrip}} \left(\frac{dx}{dt}\right)^{-1} dx \tag{4.2}$$

$$= \frac{2L_x}{c} + \frac{1}{2}\int_{t-2L/c}^{t} h(t')dt'. \tag{4.3}$$

Similarly, the duration $T_y(t)$ it takes for the laser light to propagate in the y arm can be written by

$$T_y(t) = \frac{2L_y}{c} - \frac{1}{2}\int_{t-2L/c}^{t} h(t')dt'. \tag{4.4}$$

Therefore, defining a laser electric field incident to the BS by $E_{\text{in}}(t) = E_0 \mathrm{e}^{i\omega_0 t}$, the electric field at the output port $E_{\text{out}}(t)$ is expressed as

$$E_{\text{out}}(t) = \frac{1}{2}\left[E_{\text{in}}(t - T_x(t)) - E_{\text{in}}(t - T_y(t))\right] \tag{4.5}$$

$$= \frac{1}{2}E_0 \mathrm{e}^{i\omega_0(t-T_x(t))}\left[1 - \mathrm{e}^{i(\phi+\phi_{\text{GW}}(t))}\right], \tag{4.6}$$

$$\phi = \frac{2\omega_0(L_x - L_y)}{c}, \tag{4.7}$$

$$\phi_{\text{GW}}(t) = \omega_0 \int_{t-2L/c}^{t} h(t')dt'. \tag{4.8}$$

By detecting phase variations $\phi_{\rm GW}(t)$ at the output port, the GWs are detected. The Fourier transform of Equation (4.8) leads to $\phi_{\rm GW}(\Omega) = C_{\rm MI}(\Omega)h(\Omega)$, defining the response function of a Michelson interferometer $C_{\rm MI}(\Omega)$:

$$C_{\rm MI}(\Omega) = \frac{2\omega_0 L}{c}\frac{\sin(\Omega L/c)}{\Omega L/c}\mathrm{e}^{-i\Omega L/c}. \tag{4.9}$$

4.1.2 Detection scheme

Because we detect power of the laser field by photodetectors, we have to use interferometric techniques to readout the phase of the output laser field, which convert it into optical power varations. Here, such techniques are summarized.

Mid-fringe detection

The most primitive way to detect the phase variations of the electromagnetic field of the output laser is so-called Mid-fringe detection. Substituting $\pi/2$ into ϕ in Equation (4.6), the laser power at the output port $P_{\rm out}(t)$ turns to be[‡2]

$$P_{\rm out}(t) \simeq \frac{P_0}{2} + \frac{P_0}{2}\phi_{\rm GW}(t), \tag{4.10}$$

where $P_0 = |E_0|^2$. In this way, $P_{\rm out}(t)$ has a linear term of $\phi_{\rm GW}(t)$ and so the GWs can be detected. This scheme is called *mid-fringe* detection because the half of the input power goes to the output port.

Homodyne readout

One commonly used scheme is homodyne readout. If ϕ is kept to be zero, the output field becomes

$$E_{\rm out}(t) = \frac{-i}{2}E_1\mathrm{e}^{i\omega_0 t}\phi_{\rm GW}(t), \tag{4.11}$$

where $E_1 = E_0\mathrm{e}^{-i\omega_0 T_x(t)}$. This condition is called *dark fringe* condition, since the output port is kept dark in the sense that no constant field is coming out there. A merit of adopting the dark fringe condition is that all of the constant fields are reflected back to the input side, which enables us to use a technique called *power recycling* (see Section 4.3).

[‡2]Here the higher order terms of $\phi_{\rm GW}$ are ignored. In the field of precision interferometry, such time-varying phase terms are actively controlled so that this approximation is valid. The same approximation is also used hereafter.

Let us assume that there is a reference field denoted by $E_{\rm ref} = -iAE_1$, where A is a real number. The interference of these two fields are written as

$$E_{\rm homo}(t) := E_{\rm ref}(t) + E_{\rm out}(t) = -iE_1 \mathrm{e}^{i\omega_0 t}\left(A + \frac{\phi_{\rm GW}(t)}{2}\right). \tag{4.12}$$

The optical power $P_{\rm homo}(t)$ of the interference field $E_{\rm homo}(t)$ is

$$P_{\rm homo}(t) \simeq P_0\left[A^2 + A\phi_{\rm GW}(t)\right], \tag{4.13}$$

where linear signals of the GWs are obtained.

One implementation of the homodyne readout scheme is DC readout [107]. If ϕ is kept to be a certain small number instead of zero,

$$E_{\rm out}(t) = -iE_1 \mathrm{e}^{i\omega_0 t}\left(\frac{\phi}{2} + \frac{\phi_{\rm GW}(t)}{2}\right), \tag{4.14}$$

where the first term can be regarded as a reference field. One of the merits of DC readout is there is no need to prepare an additional reference light field. DC readout is employed in the sensing of the length degree of freedom (DoF) corresponding to GWs[‡3] in the 2G detectors.

Another implementation is balanced homodyne readout (Figure 4.2). The difference of the outputs of these two photodetector, namely $P_{\rm BHD}$, is expressed as

$$P_{\rm BHD}(t) \simeq P_0\left[A^2 + A\phi_{\rm GW}(t)\right], \tag{4.15}$$

where some symbols are defined as some ways. These two are the major benefits of balanced homodyne readout. One is noise associated with the reference field can be cancelled out by the subtraction. The other is the relative phase between the output field $E_{\rm out}(t)$ and the reference field $E_{\rm ref}(t)$ can be controlled at an arbitrary point, which is crucial in realizing quantum backaction evasion [108]. It is planned that the scheme of balanced homodyne readout will be used in the upgrade of Advanced LIGO, so called A+ [109, 110].

Heterodyne readout (RF readout)

In order to read out the output field in the dark fringe condition, we can prepare another kind of reference fields. Let us consider a reference filed denoted by $E_{\rm ref} = -iAE_1 \sin\Omega_m t$. Usually, $\Omega_m/2\pi$ is chosen from the range of $\sim 10 -$

[‡3]This DoF is called DARM (Figure 4.6).

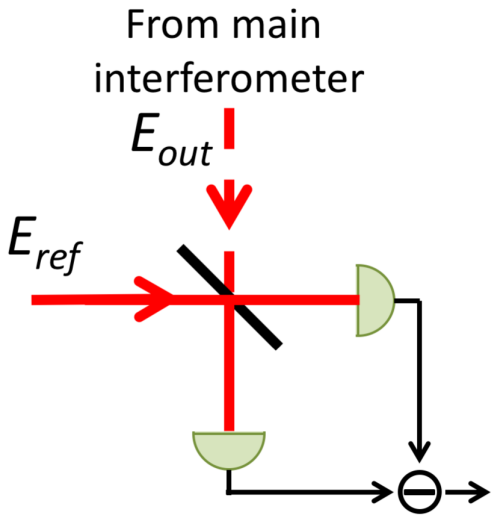

Figure 4.2: Schematic view of an optical layout for the balanced homodyne readout. The output field from the main interferometer interferes with a reference field at a 50:50 beam splitter. The signals from two photodetectors are subtracted with each other so that noise associated with the reference field will be cancelled out.

200 MHz.[‡4] This is because this scheme is called radio frequency (RF) readout. The interference of the reference and output fields are written as

$$E_{\rm hetero}(t) := E_{\rm ref}(t) + E_{\rm out}(t) = -iE_1 {\rm e}^{i\omega_0 t}\left(A\sin\Omega_m t + \frac{\phi_{\rm GW}(t)}{2}\right). \tag{4.16}$$

The optical power $P_{\rm hetero}(t)$ of the interference field $E_{\rm hetero}(t)$ is

$$P_{\rm hetero}(t) \simeq P_0\left[A^2\sin^2\Omega_m t + A\sin\Omega_m t\cdot\phi_{\rm GW}(t)\right], \tag{4.17}$$

[‡4]In the field of the GW detectors, these frequencies are commonly used for the following reasons. One is that the frequency band of the phase variations we want to detect (including auxiliary DoFs) is, at most, up to 1 MHz so that filtering of Ω_m components is feasible without affecting the phase variation signals very much. Another reason is that, up to a few hundreds of MHz, it is rather easy to handle circuits associated with the photodetectors as a lumped-element model. Effective capacitance of a photodiode with reasonable diameter ($\sim$ 1 mm) is also tolerable.

which is detected by an RF photodetector. The output of the RF photodetector is then demodulated by $\sin \Omega_m t$, which yields

$$V_{\rm demod} := P_{\rm hetero}(t) \sin \Omega_m t = P_0 \left[\frac{A}{2} \phi_{\rm GW}(t) + (\text{RF terms}) \right]. \tag{4.18}$$

The RF terms consist of terms proportional to $\sin n\Omega_m t$ or $\cos n\Omega_m t$, where n is any non-zero integer. Since the RF terms can be easily low-passed out by passive electrical components, a linear signal of $\phi_{\rm GW}(t)$ is obtained in this way.

A commonly used realization of heterodyne readout of a Michelson interferometer is the use of Schnupp asymmetry [111]. Let us set $L_x - L_y = l_{\rm as}$, where $l_{\rm as}$ is macroscopic length difference (on the order of centimeters to meters). If we inject a phase-modulated laser field $E_{\rm in}(t) = E_0 \exp[i\omega_0 t + i\beta \cos \Omega_m t]$ to the interferometer, the output field turns to be

$$E_{\rm out}(t) = -iJ_0(\beta) E_1 e^{i\omega_0 t} \left[(2J_1(\beta)/J_0(\beta)) \sin\alpha \sin \Omega_m t + \frac{\phi_{\rm GW}(t)}{2} \right] \tag{4.19}$$

in a neighborhood of the dark fringe condition, where $\alpha = \Omega_m l_{\rm as}/c$ and J_n is the Bessel function. Here, terms proportional to $\sin n\Omega_m t$ or $\cos n\Omega_m t$ with $n > 1$ are ignored. In this way, the reference field is provided at the output port and so heterodyne readout can be realized. This scheme is used for central Michelson interferometer of the GW detectors (Section 4.3).

4.1.3 Laser noise rejection

As pointed out in the first proposal [53], a Michelson interferometer can reject laser noise so that it does not couple to the output signal of differential phase shift. Let us consider frequency noise coupling by expressing the input field by $E_{\rm in} = E_0 e^{i(\omega_0 t + \delta\psi(t))}$. Then the output of the interferometer can be written as

$$E_{\rm out}(t) = \frac{-i}{2} E_1 e^{i\omega_0 t} \left(\frac{2l_{\rm as}}{c} \delta f(t) + \phi_{\rm GW}(t) \right), \tag{4.20}$$

where $\delta f = {\rm d}(\delta\psi)/{\rm d}t$ is frequency fluctuations of the input laser. This equation shows that the frequency noise coupling can be arbitrarily small by making two arms symmetrical.

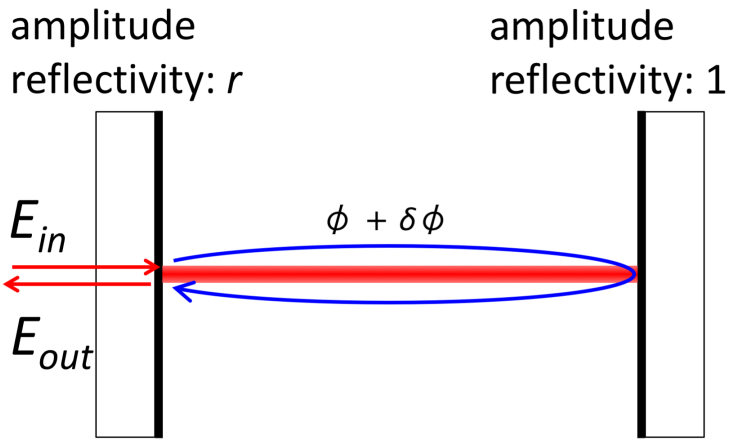

Figure 4.3: Schematic diagram of a Fabry–Perot cavity. The amplitude reflectivity of the input mirror is denoted by r.

4.2 Fabry–Perot cavity

4.2.1 Response

As briefly mentioned in Section 3.2.2, a Fabry–Perot cavity[‡5] is employed in each arm of the Michelson interferometer of the GW detectors (Figure 4.6), in order to make the effective arm length longer. Such an interferometer is called Fabry–Perot Michelson interferometer (FPMI). Let us consider an optical cavity shown in Figure 4.3. Let $E_{\rm in}(t) = E_0 e^{i\omega_0 t}$ be the incident field to the cavity. Let us then express a roundtrip phase of the laser field in the cavity by $\phi + \delta\phi(t)$, where ϕ is constant part and $\delta\phi(t)$ is time-varying small deviations of the phase. Hereafter, let us use Fourier domain to discuss the phase deviations. If ϕ is set to be an integer multiple of 2π, meaning that the laser is kept at the resonance of the cavity, the reflection $E_{\rm out}(t)$ can be described as

[‡5]See Appendix C for more detail.

$$E_{\rm out}(t) = E_0 \mathrm{e}^{i\omega_0 t} \cdot \mathrm{e}^{-iC_{\rm FP}\delta\phi(f)}, \tag{4.21}$$

$$C_{\rm FP} = \frac{r^{1/2}(1+r)}{2\sinh\left[\frac{|\ln r|}{2}\left(1+i\Omega/\Omega_{\rm cav}\right)\right]} \tag{4.22}$$

$$\simeq \frac{2\mathcal{F}}{\pi}\frac{1}{1+i\Omega/\Omega_{\rm cav}} \quad \left(1-r \ll 1,\ \frac{\Omega}{2\pi} \ll f_{\rm FSR}\right), \tag{4.23}$$

where

$$\Omega_{\rm cav} = |\ln r| \cdot f_{\rm FSR} \simeq 2\pi\frac{f_{\rm FSR}}{2\mathcal{F}}, \tag{4.24}$$

$$\mathcal{F} \simeq \frac{2\pi}{1-r^2}, \tag{4.25}$$

$$f_{\rm FSR} = \frac{c}{2L}. \tag{4.26}$$

Here, $\Omega_{\rm cav}/2\pi$ is called cavity pole frequency or half linewidth of the cavity, the inverse of which represents average storage time of the cavity. $f_{\rm FSR}$ is free spectral range (FSR), which corresponds to the separation of two nearby resonances in terms of frequency. $\mathcal{F}$ is called finesse, which is a (dimensionless) ratio of the FSR to the full linewidth ($2\Omega_{\rm cav}/2\pi$). Finesse is proportional to average roundtrip numbers in the cavity. Equation (4.23) shows how a Fabry–Perot cavity amplifies the phase deviations inside the cavity. The GW signal is amplified by a factor of $2\mathcal{F}/\pi$ and the amplification gets reduced with a low-pass response with the corner frequency equal to the cavity pole frequency. Figure 4.4 compares the responses of a FPMI and a MI with long arms. Each cavity mirror closer to the BS is called input test mass (ITM), and the farther one is called end test mass (ETM) (Figure 4.6).

4.2.2 Detection scheme

The most commonly used scheme to detect the phase deviations of the reflected laser field is the Pound–Drever–Hall (PDH) technique [112]. This method applies heterodyne readout to the sensing of a cavity. Let us consider the case where a phase-modulated laser field is injected to an optical cavity; $E_{\rm in}(t) = E_0\exp[i\omega_0 t + i\beta\cos\Omega_m t]$. If the modulation frequency is chosen in such a way that the modulation sidebands[‡6] are far from resonance, the reflection of the

[‡6]Please refer to Appendix D for sideband picture of modulations.

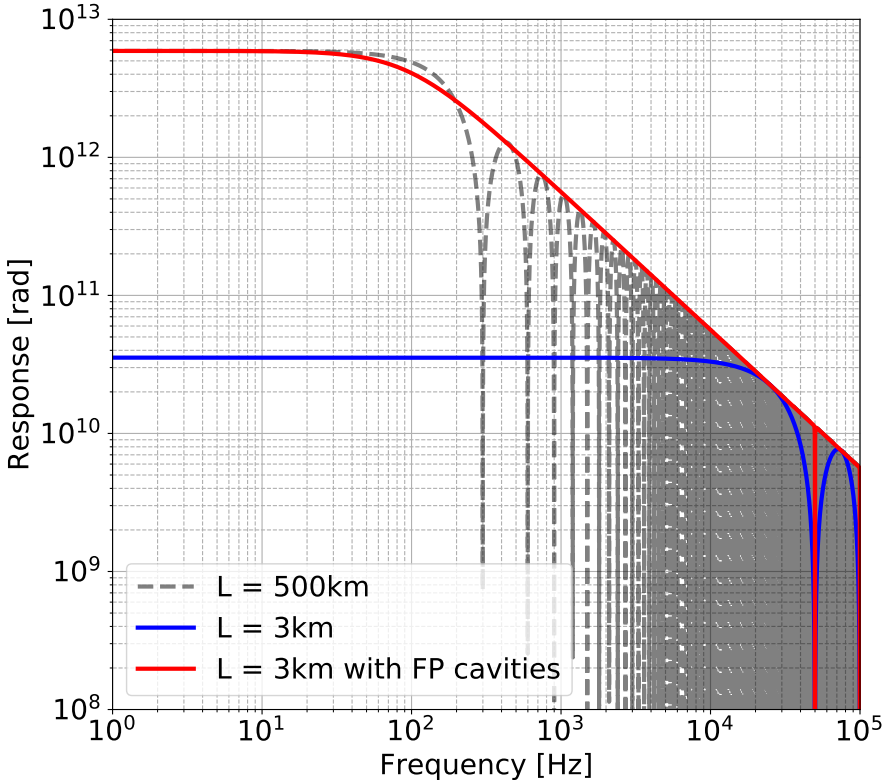

Figure 4.4: Response functions from GW strain to phase deviation of the output optical field in various interferometer configurations. The gray dashed line shows the response of a MI with long arms. The blue line shows the response of a MI with short arms. The red line shows the response of a FPMI having short arms but long effective arm length ($\mathcal{F} = 262$).

cavity $E_{\mathrm{out}}(t)$ can be written as

$$E_{\mathrm{out}}(t) = J_0(\beta)E_0 \mathrm{e}^{i\omega_0 t} \cdot \left[1 - i\frac{2J_1(\beta)}{J_0(\beta)} \cos \Omega_m t - iC_{\mathrm{FP}}\delta\phi(f)\right]. \tag{4.27}$$

Therefore, the optical power of the reflection $P_{\mathrm{out}}(t)$ is

$$\begin{aligned} P_{\mathrm{out}}(t) = {} & 4J_0(\beta)J_1(\beta) \cos \Omega_m t \cdot C_{\mathrm{FP}}\delta\phi(f) \\ & + (\text{constant term}) + (2\Omega_m \text{ or higher order terms}). \end{aligned} \tag{4.28}$$

This shows that the phase variations can be detected by demodulating the photodetector output with $\cos \Omega_{\mathrm{m}} t$.

It is worth noting that the PDH signal is obtained by a demodulation with $\cos \Omega_{\mathrm{m}} t$ while the Michelson signal with Schnupp asymmetry is obtained by a demodulation with $\sin \Omega_{\mathrm{m}} t$, comparing Equations (4.19) and (4.28). The phase of the demodulation sinusoid that gives the PDH signal is called in-phase (I-phase) while the phase that gives the Michelson signal is called quadrature phase (Q-phase).

Figure 4.5 shows how the PDH signals behave as ϕ changes across FSRs. This illustrates that the linear range of the PDH signal is very narrow. In order to have the amplification effect of the cavity, it is necessary to keep controlling the phase, ϕ, within the narrow range very close to the resonance.

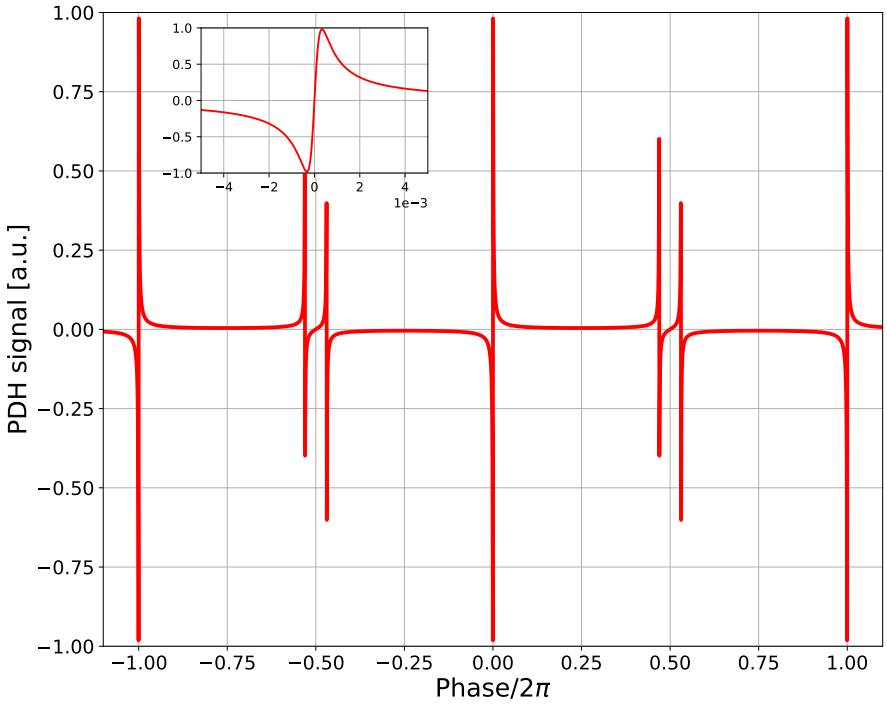

Figure 4.5: How typical PDH signal behaves ($\mathcal{F} = 1500$). The inset shows the enlarged view around the resonance.

4.3 Dual-recycled Fabry–Perot Michelson interferometer

A Michelson interferometer having Fabry–Perot cavities in both arms is called a Fabry–Perot Michelson interferometer (FPMI). The current GW detectors combine with a FPMI two techniques, which are *power recycling* and *resonant sideband extraction*.[‡7] A FPMI with these techniques incorporated is called a dual-recycled Fabry–Perot Michelson interferometer (DRFPMI). Figure 4.6 shows a schematic view of a DRFPMI.

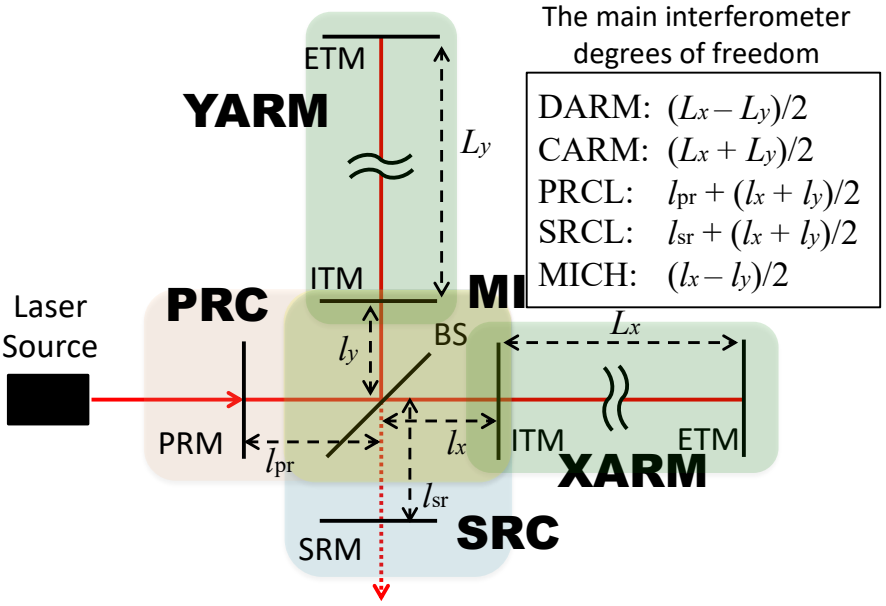

Figure 4.6: Schematic diagram of a dual-recycled Fabry–Perot cavity. The definition of each length DoF is also described.

4.3.1 Power recycling

As the FPMI is operated in dark fringe condition, most of the laser power comes back to the input side. The power recycling mirror (PRM), which is placed at the input side of the FPMI, resonantly reflects back such a return beam to the FPMI

[‡7]Resonant sideband extraction is also known as *signal recycling*.

part so as to enhance the laser power at the FPMI part. Higher power leads to better signal-to-noise ratio of shot noise as mentioned in Section 3.2.4. This technique is called power recycling (PR) [113]. The PRM has to be controlled so that the carrier field satisfies the anti-resonant[‡8] conditions of the cavity formed by the PRM and ITMs, which is called the PR cavity.

4.3.2 Resonant sideband extraction

A mirror placed at the output side of the FPMI is called the signal recycling mirror (SRM). Although the laser field coming from the input side does not go to the output side, differential modulations of the laser field introduced in the arms, which include GW signals, leak to the output side. If such modulation sidebands[‡9] resonate between the SRM and the ITMs, average storage time of the sidebands in the arm cavities becomes smaller, or more specifically, effective finesse of the arm cavities for the sidebands becomes smaller, so that the cut-off frequency in the response to GW signals is pushed up. This technique is called resonant sideband extraction (RSE) [113, 114]. The effective finesse can be written by

$$\mathcal{F}_{\mathrm{eff}} = \frac{1-\sqrt{R_{\mathrm{s}}}}{1+\sqrt{R_{\mathrm{s}}}}\mathcal{F}, \tag{4.29}$$

where R_{s} is the reflectivity of the SRM. The SRM has to be controlled so that the carrier field satisfies the resonant conditions of the cavity formed by the SRM and ITMs, which is called the SR cavity.

Figure 4.7 schematically shows how the ASD of (strain-equivalent) shot noise is reshaped by PR and RSE. This figure shows that RSE improves shot noise in high frequencies at the cost of worse shot noise in low frequencies. It also shows that increasing the power at the BS by a factor of N with a help of PR is equivalent to increasing the arm finesse by N and broadening the bandwidth by N with RSE at the same time. Since the latter does not increase the laser power at the BS, combining PR and RSE can provide the optimized shot noise curve while the power at the BS and the power inside the arm cavities are balanced with a desired ratio.

[‡8] When the roundtrip phase in a cavity is a half-integer multiple of 2π, such a condition is called anti-resonant.

[‡9] Please refer to Appendix D for sideband picture of modulations.

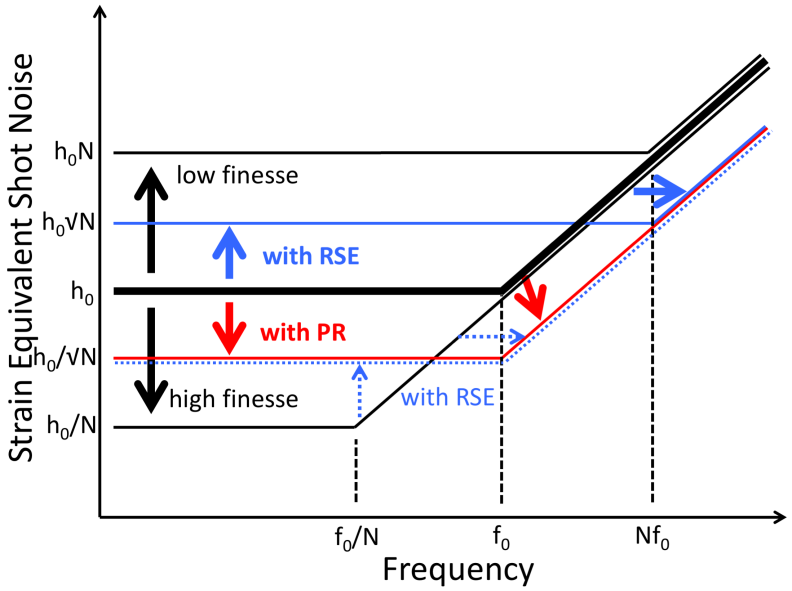

Figure 4.7: Conceptual diagram of how the ASD of strain-equivalent shot noise changes as the interferometer configuration changes.

4.3.3 Detection scheme

A DRFPMI is a coupled interferometer consisting of five length DoFs. The name of each DoF is defined in Figure 4.6. Since all of them are coupled with each other, it is not straightforward to separately detect each DoF. Here the common sensing scheme employed in the 2G detectors are explained. The injection laser field is phase-modulated at two different frequencies. The Schnupp asymmetry and the modulation frequencies are chosen so that one pair of sidebands (f_1)[‡10] leaks to the output side while the other (f_2) does not. The length of recycling cavities are set so that the carrier field satisfies the anti-resonant or resonant conditions of the PR or SR cavities, respectively, when f_2 sidebands resonate in the PR cavity and f_1 sidebands resonate in the PR-SR coupled cavity. In this way, three DoFs of central interferometer (PRCL, SRCL, and MICH) are sensed with heterodyne readout by using the modulation sideband fields as signal fields and the carrier field as a reference field. DARM is sensed with DC readout at the output port of the DRFPMI. As the output mode-cleaner (OMC)[‡11] is

[‡10] See also Figure 6.4.
[‡11] Advanced Virgo uses two OMCs in series.

employed to reject undesired RF sidebands and higher order transverse modes, the transmission of the OMC, namely OMC TRANS, is used for DARM sensing. Before the DARM error signal is switched to OMC TRANS, the PDH signal at the transmission of the SRM (AS port; Figure 6.3) is used. CARM is sensed by the PDH signal at the reflection of the main interferometer (REFL port; Figure 6.3) as the f_1 or f_2 sidebands are used as the reference field. Although either of the PDH signals at REFL port and the pick-off port of the PR cavity (POP ports; Figure 6.3) is linear combination of CARM and PRCL, they are linearly independent so that CARM and PRCL can be sensed independently. A similar thing holds for SRCL. In a later section, Table 6.3 summarizes the error signal for each DoF in the case of KAGRA.

4.4 Advanced techniques

To improve the sensitivity further, other advanced techniques are implemented or to be implemented in the 2G and the 3G detectors, exploiting quantum nature of light.

4.4.1 Squeezed light injection

Unless light fields are prepared in a certain quantum mechanical state, shot noise of the interferometer output follows the Poisson distribution, which means that the standard deviation of the number of received photons in a certain period is $\sqrt{N}$ if the expectation of the photon number is N. If the light field is in a squeezed state, the fluctuations of the number of received photons can be made below the level of the Poisson distribution. Please refer to Appendices D and E for more detail. If a light field is in a squeezed state, fluctuations of electric field along a certain direction in the complex plane are reduced while the fluctuations along the perpendicular direction are increased [115].

In the context of the GW detectors, use of squeezed light can reduce shot noise at the cost of the increase of radiation pressure noise. Figure 4.8 shows how squeezed light can be incorporated in an interferometer of the GW detectors. Since the interferometer reflects the laser field back to where it is injected from, the laser field at the detection port is determined by *vacuum* fields entering to the interferometer. By injecting squeezed vacuum there and properly controlling the squeezing angle, the reduction of shot noise can be realized.

Advanced LIGO and Advanced Virgo are currently operating with a help of squeezed light injection, without introducing additional excess noise [116, 117].

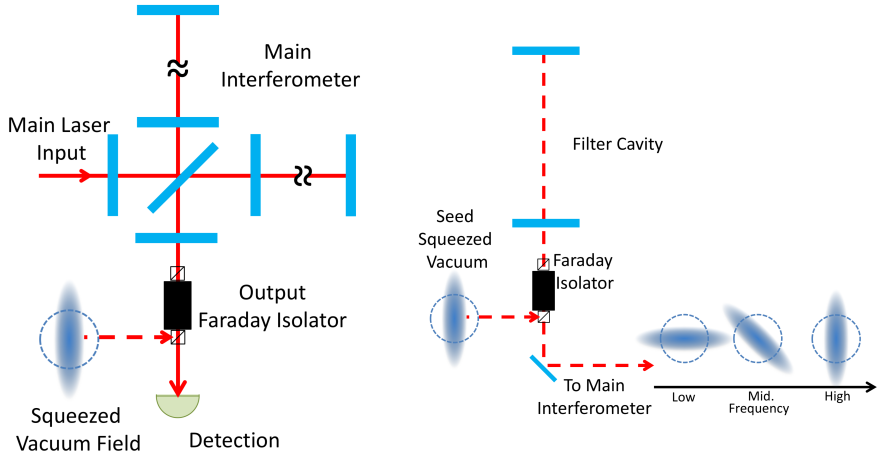

(a) Squeezed light injection. (b) How a filter cavity rotates the squeezing ellipse.

Figure 4.8: Schematic diagrams of how the squeezed vacuum is incorporated with the interferometer.

KAGRA also has a plan to implement squeezing.

4.4.2 Filter cavity

Since radiation pressure noise limits the sensitivity only in low frequency region, the overall quantum noise curve can be improved by controlling the squeezing angle in a frequency-dependent way; the angle is controlled so that radiation pressure noise is reduced in low frequency region while shot noise is reduced in high frequency region. Such a rotation of squeezing angle can be realized by reflecting a squeezed field with a fixed squeezing angle off a detuned optical cavity, namely a filter cavity (Figure 4.8) [108].

The principle of this technique has been demonstrated [63]. Worldwide efforts are being made toward its implementation to the GW detectors [63,64,118]. It is planned that a filter cavity will be employed in the upgrade of each 2G detector and the 3G detectors [8, 89, 109].

4.4.3 Detuned RSE

As described in Section 4.3, a SR cavity can reshape the response function of the detector to GWs. If the SR cavity is detuned by certain amount, radiation pressure noise can be cancelled in a narrow frequency range thanks to quantum correlation between shot noise and radiation pressure noise, as well as GW signals are amplified at the frequencies according to the amount of detuning [119, 120]. This technique is called detuned RSE. It is adopted in the design configurations of KAGRA and the low frequency detectors of Einstein Telescope [20, 89].

4.5 Challenges in the 3G detectors

4.5.1 Long arms

The 3G detectors will have $3-10$ times longer arms than those of the 2G. The arm length of Einstein Telescope will be 10 km, and that of Cosmic Explorer will be 40 km. A possible challenge arising from long arm length is difficulty in the frequency stabilization control using CARM.

Assuming that the finesse of a virtual cavity corresponding to CARM is a constant regardless of the arm length,[‡12] the linewidth of the CARM cavity becomes narrower in terms of frequency if the arm cavities get longer. This indicates that requirements on frequency stabilization control becomes stringent in the 3G detectors. In particular, lock acquisition of CARM becomes even more challenging. In addition, the error signal of CARM will be more easily distorted by the ringing effect due to the dynamical evolution of the electromagnetic field in the cavity [121, 122]; laser frequency change in a timescale shorter than the inverse of the linewidth of the cavity causes the effect. The other is that the requirements on the CARM control by the ALS system become stringent. Please refer to Chapter 8 for more detail.

Another effect of long arms is that the frequency of the FSR is no longer above the interested frequency range. In the case of Cosmic Explorer, the FSR is 3.75 kHz, which is not only within the observation frequency band but also

[‡12]The fluctuations of the injected laser and common displacement in two cavity lengths couple with each other. This DoF can be treated as a cavity. The PRM makes its effective finesse larger than that of a single arm cavity. The assumption that the finesse is independent of the arm length is reasonable because the finesse is determined purely by optical loss in the arm cavities if the power recycling is in the optimal condition, which has little dependence on the cavity length.

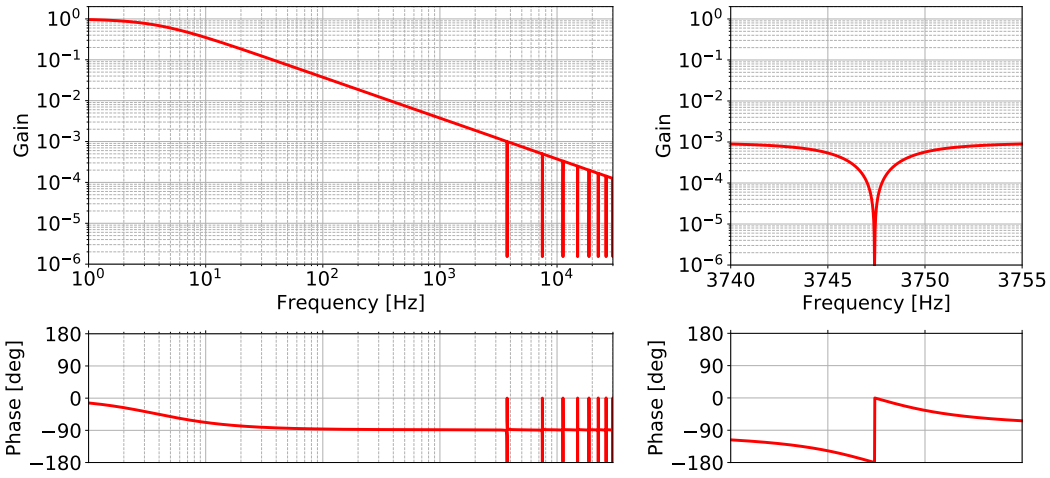

(a) Overview

(b) Enlarged view around the first FSR

Figure 4.9: Response transfer function of a cavity with the FSR of 3.75 kHz and the finesse of 500 to the frequency fluctuations of input laser.

likely to be within the control frequency band of CARM. Figure 4.9 shows the response transfer function of a cavity to the frequency fluctuations of input laser. It behaves in a complicated way like a notch filter around the frequencies of the integer multiple of the FSR [123]. In order to have a stable control loop [‡13] of CARM with the bandwidth up to ~ 10 kHz, it is necessary to flatten such structures by the servo filter. This will possibly be a new challenge in the 3G detectors.

4.5.2 Weak actuators

As an example, Figure 4.10 compares low frequency noise spectra of Advanced LIGO and Cosmic Explorer in terms of displacement, showing that the requirement on displacement noise of a test mass will be ~ 10 times more stringent in Cosmic Explorer. This implies that ~ 10 times weaker actuators with inevitably smaller range have to be used for each test mass. This will make the DARM control even more difficult, which relies on test mass actuators. In particular, lock acquisition of DARM will be challenging due to saturation of the actuators.

[‡13] See Appendix B for stability conditions of a control loop.

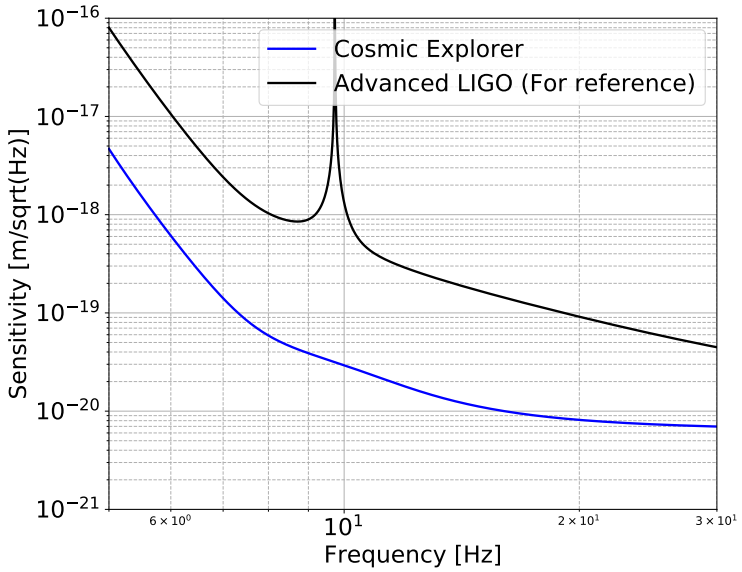

Figure 4.10: Design sensitivities of the 2G and the 3G detectors in low frequency, in terms of displacement.

Chapter 5
LOCK ACQUISITION

Lock acquisition or interferometer locking is a process to bring the interferometer from a state where each DoF is moving in a stochastic way to the observation state, where each DoF is controlled with a low noise sensor that generally has a narrow linear range. Such sensors show highly nonlinear behaviors outside their linear range and each DoF is cross-coupled with each other meaning that it is usually not possible to lock each DoF one by one. Therefore, lock acquisition process is not straightforward and thus it requires intensive development. In this chapter, the overview of lock acquisition and the summary of the lock acquisition schemes of the present and past GW detectors are given.

5.1 Overview

Each mirror of the interferometer swings in longitudinal direction by $\sim 1\,\mu$m in $0.1 - 1\,$Hz due to seismic motion, in spite of passive and active seismic attenuation. In these conditions, each length DoF of the interferometer (Figure 4.6) stochastically fluctuates and stays only for a short period in the linear range of its sensor around the operating point. In order to bring the interferometer to the operation mode, every DoF has to be somehow confined within their linear ranges.

A process of interferometer locking has three major difficulties. The first one is that each mirror freely swings at the beginning. The second one is that each DoF of the interferometer is cross-coupled with each other. The third one is that the error signal of an single DoF shows nonlinear behaviors. Locking the interferometer against these difficulties has been considered to be one of the most challenging processes in realizing the observation of GW detectors. In fact, it typically took about one year to achieve the first lock of the interferometer in the case of the current detectors. Since the process is challenging, many efforts

has been made on this topic as follows.

One obvious way to lock the interferometer is to engage the control loops for the length DoFs during the short period when the sensor signals are in their linear ranges. Such schemes were used in TAMA300 [124, 125] and Initial LIGO [126]. If it is possible to lock the interferometer in this way, this approach has a great advantage that the lock acquisition process can be finished in short time. However, it also has the following drawbacks. The first one is that the error signals for DoFs of the central interferometer can be largely disturbed or even vanished, depending on a dynamical state of the arm cavities. The second one is that it is not straightforward to diagnose the lock acquisition process in case it is not successful. It is not possible to measure the responses of the interferometer in an intermediate state of lock acquisition for diagnostic purposes. The third one is that it is necessary to stop a swinging mirror during a short period when the corresponding DoF is in the linear range of its sensor. This condition imposes requirements of the maximum force actuators can exert. Typical force F necessary to catch the resonance of an cavity can be written as

$$F = \frac{m v_{\mathrm{RMS}}}{\Delta t} \simeq \frac{m v_{\mathrm{RMS}}^2 \mathcal{F}}{\lambda}, \tag{5.1}$$

where v_{RMS} is the root mean square (RMS) velocity of a test mass, Δt is the average time it takes for a test mass to move across the linear range of the PDH signal around the resonance, $\mathcal{F}$ is the finesse of the cavity, and λ is the wavelength of the main laser. This limitation to the maximum force of the actuators and/or the RMS velocity is called kinetic limit (Figure 5.1). It is of great relevance in the 2G or 3G detectors, since their low frequency sensitivity imposes stringent requirements on actuator noise.

Another approach for interferometer locking is to sequentially bring the DoFs into the linear ranges by using auxiliary sensors. *Variable finesse technique* in Virgo [127] can be regarded as a pioneering work of this approach. This technique utilizes the PDH signals obtained from the transmission of arm cavities to control them in intermediate steps of lock acquisition, which are not disturbed by dynamical states of the central interferometer. In addition, it starts from keeping the Michelson interferometer at mid-fringe to reduce the finesse of the PR cavity so that the central part and the arm part are even more decoupled.

A more dedicated approach is employed by a technique called *arm length stabilization* (ALS) [128]. This technique utilizes auxiliary lasers having different wavelength than that of the main laser as auxiliary sensors for arm cavities. It is adopted in Advanced LIGO [22] and KAGRA [129], and planned to be used

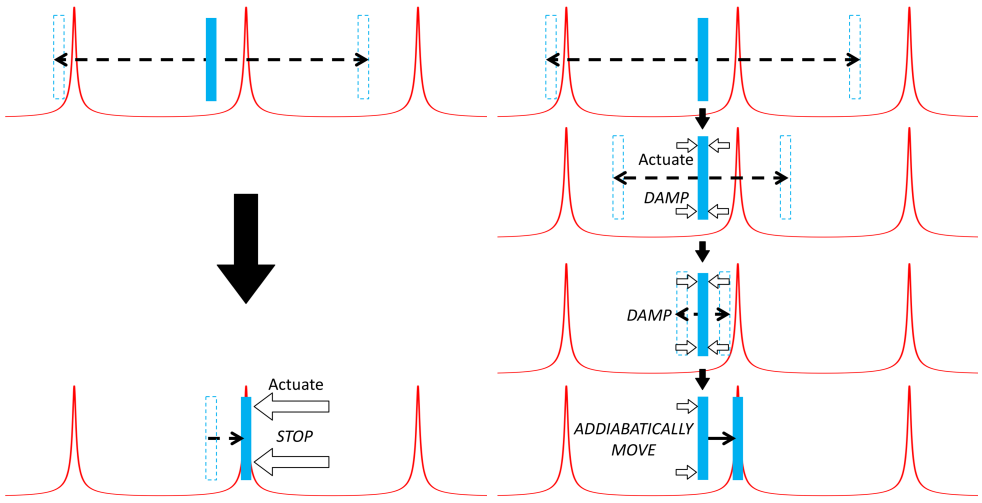

(a) Lock acquisition without ALS (b) Lock acquisition with ALS

Figure 5.1: Schematic picture of lock acquisition of a cavity with and without ALS. The red line shows the optical power inside a cavity against the mirror position, which exhibits resonant feature. The blue rectangles depict a mirror. (a) Without the help of ALS, the motion of a free swinging mirror has to be stopped within a short period when the cavity stays around the resonance. This leads to the kinetic limit. (b) Using the control by an ALS system, the motion can be gradually damped, and the cavity length can be eventually set wherever one wants, including at the resonance.

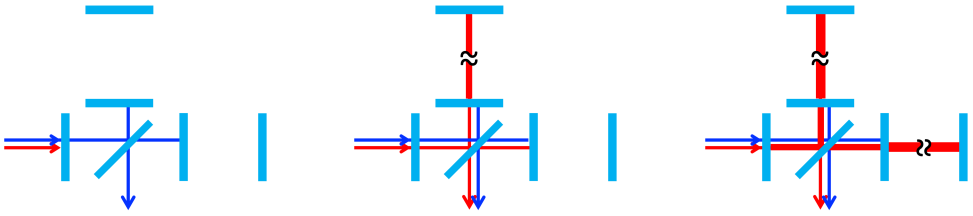

(a) (b) (c)

Figure 5.2: Schematic diagrams of the lock acquisition of Initial LIGO. Red arrows represent the carrier fields of the laser beam while blue ones represent the sideband fields. In the step (a), the central PRMI is controlled using the sideband fields. In (b), the resonance of one arm cavity is caught. In (c), the the resonance of the other arm is finally caught.

in Advanced Virgo in its upgrade. The technique ALS is the main topic of this dissertation.

5.2 Previous techniques

5.2.1 Initial LIGO scheme

The power-recycled Fabry–Perot Michelson interferometer (PRFPMI) of Initial LIGO was locked in the following sequence [126]. First, the central interferometer is controlled so that the modulation sidebands field resonate there (Figure 5.2). In this step, the demodulated signals of the reflection PD output are used for the control of PRCL and MICH. Next, the resonance of one of the arm cavities is caught when the arm goes across it resonance. Finally, the resonance of the other arm is also caught to end the lock acquisition process.

5.2.2 Third harmonic demodulation technique

The above scheme has an issue that the error signals for PRCL and MICH can be largely disturbed or even vanished due to the resonance of the arm cavities. In order to mitigate this issue, a robust signal extraction scheme called *third harmonic demodulation* was developed in TAMA300 [125]. This scheme does not

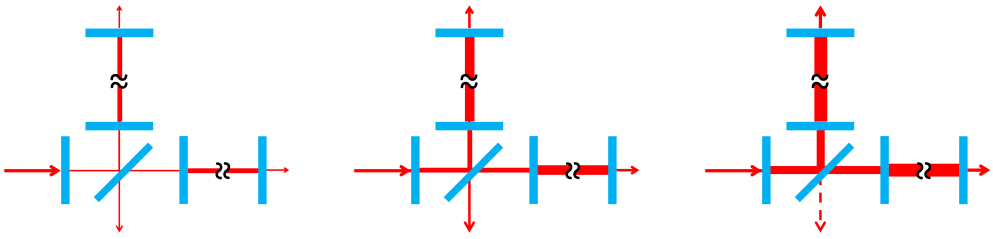

(a) (b) (c)

Figure 5.3: Schematic diagrams of the variable finesse technique. In the step (a), both arm cavities are controlled at their resonances using the transmission PDH signals while the central interferometer is controlled with the Michelson interferometer being at mid-fringe. In (b), the condition of MICH is gradually changed to dark fringe. In (c), the Michelson interferometer reaches dark fringe and then the error signal for each DoF is switched to that in the final state.

rely on the carrier field of the laser for the extraction of the PRCL and MICH[‡1] so that the arm cavities affect much less when the carrier field is close to the resonance of an arm. Instead of the carrier filed, the second order modulation fields are used as reference fields of PRCL and MICH sensing. This scheme is still used in Advanced LIGO and KAGRA.

5.2.3 Variable finesse technique

In Virgo detector, the PRFPMI was locked using the variable finesse technique [127,130] (Figure 5.3). First, each arm cavity is kept at resonance using the PDH signals from the transmission of the arm, and MICH is controlled at mid-fringe. PRCL is also controlled. At this stage, the coupling between the arms and the central interferometer is small since MICH is at mid-fringe so that the finesse of the PR cavity is very small. Next, the condition of MICH is gradually changed to dark fringe. Finally, the error signal for each DoF is switched to that in the final state. This technique has been used in Advanced Virgo because the optical configuration is a PRFPMI until now, at the time of O3.

[‡1] And also SRCL in a DRFPMI.

5.3 ALS

A technique called ALS uses one auxiliary laser for each arm cavity so as to independently sense the arm cavity length, or equivalently the resonant frequency of the cavity with respect to the main laser frequency [128]. In the first stage of lock acquisition, the arm cavities and central interferometer are controlled separately. Once CARM and DARM are confined within the linear range of their final sensing signals coming from the main laser, the CARM and DARM controls are handed over to these signals and, eventually, all DoFs are controlled using the main laser signals.

The features and advantages of use of ALS can be summarized as follows:

(i) Use of different wavelength (from that of the main laser) enables us to independently sense the length fluctuations of one arm.[‡2] With the help of dichroic coating of mirrors, the optical configurations are designed so that each auxiliary laser field is affected only from the corresponding arm cavity. In addition, the finesse of the arms for the auxiliary laser can be set relatively low for the ease of locking the cavity (In the case of KAGRA, the finesse was set to about 50, as noted in Table 6.1).

(ii) By utilizing frequency conversion of lasers, e.g. second harmonic generation (SHG), optical interference between the main laser and the auxiliary lasers are realized so that the difference among the frequencies of these lasers are always monitored. Thanks to this, the resonant frequencies of the arms are controlled with respect to the main laser frequency and vise versa.

(iii) The frequency of each auxiliary laser can be actuated so that the laser are kept resonating in the arm. Adding such actuators enables us to sense the difference between the resonant frequency of the arm and the main laser frequency even if the PDH signal of the arm associated with the main laser is far away from its linear range. The signals from the auxiliary lasers are always kept within their linear range.

The above items are conceptually illustrated in Figure 5.4. It is worth noting that the advantage (i) inevitably comes at a cost of a potential disadvantage;

[‡2]There is a scheme to independently measure displacement of mirrors by utilizing digital interferometry [131, 132], without introducing different-colored lasers. Such a scheme may be utilized for ALS instead of using auxiliary lasers.

the optical paths are different for the main and auxiliary lasers[‡3] so that phase noise in the differential paths biases the ALS sensing.

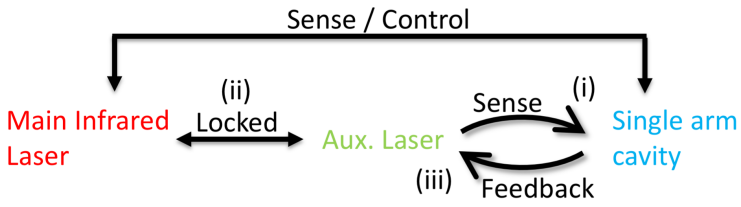

Figure 5.4: Conceptual diagram of ALS.

5.3.1 Necessity of ALS

It is considered that the ALS scheme is necessary in the lock acquisition process in the 2G and 3G detectors with the DRFPMI configuration. This is because it is not clear how to extend lock acquisition schemes without ALS developed so far for the PRFPMI configuration to the DRFPMI configuration.[‡4] In addition, with ALS, the kinetic limit is not imposed on the arm cavities thanks to the third feature described above (also by Figure 5.1). Therefore, adopting a lock acquisition scheme with ALS reduces the requirements on the test mass suspensions and actuators. For these reasons, schemes with ALS are so far the only solutions for lock acquisition of a kilometer-scale DRFPMI.

5.3.2 Requirements

Here the requirements on the ALS system are described. The noise requirement can be given primarily by the following condition (*primary noise requirement*). The frequency fluctuations of the main laser with respect to the resonance of the single arm cavity are suppressed within the linewidth of the arm cavity in terms of the RMS. If this condition is satisfied, it is possible to hand over the controls from the ALS system to the main laser PDH signals, by utilizing the signal derived from the optical power in transmission in intermediate steps of lock acquisition, as is done in Advanced LIGO [22].

[‡3]Dispersion of the main and auxiliary lasers is not negligible. More practically, it is technically difficult to make the input mode cleaner and the input Faraday isolator dichroic.

[‡4]There is an ongoing simulation work to extend variable finesse technique to a DRFPMI [133].

A more *ambitious noise target* can be set by the CARM linewidth.[‡5] It has to be noted here that the linewidth of the CARM cavity is narrower than that of a single arm cavity or the DARM cavity, since PR effectively enhances the finesse of the arm while RSE effectively reduces the finesse. If the RMS of the residual frequency fluctuations is suppressed below the level of the CARM linewidth, the CARM control can be directly handed over from the ALS CARM to the main laser PDH signal. This would greatly simplify the lock acquisition process and contribute in reducing the down time of the detector. The CARM linewidth can be expressed as

$$\kappa_{\mathrm{CARM}} \simeq \left(\frac{1-\sqrt{R_{\mathrm{PRM}}}}{1+\sqrt{R_{\mathrm{PRM}}}} + \frac{T_{\mathrm{loss}}}{T_{\mathrm{ITM}}} \right) \kappa_{\mathrm{ARM}}, \tag{5.2}$$

where κ_{ARM} and κ_{CARM} are the linewidths of the single arm and CARM, respectively, R_{PRM} is the reflectivity of the PRM, T_{ITM} is the transmissivity of the ITMs, and T_{loss} is the roundtrip loss in the arm cavity. As T_{PRM} is usually from a few to ten percent, the CARM linewidth is $\sim 10-50$ times narrower than the single arm linewidth.

Another requirement on the ALS system is the range of frequency actuation of the auxiliary lasers injected to the arms (feature (iii)). The range has to be large enough to follow the fluctuations of the resonant frequency of the arm.

5.3.3 ALS in Advanced LIGO

Figure 5.5 is the schematic view of the ALS system of Advanced LIGO [22]. Small fraction of the pre-stabilized laser (PSL) are picked off and sent from the corner station (area that houses ITMs, BS, and so on) to both end stations (area that houses an ETM) via optical fibers. The picked-off PSL is used to stabilize the frequency of an auxiliary laser placed behind each ETM, by taking beat note of the PSL and the infrared output of the auxiliary laser in the end station. The laser head of the auxiliary laser has built-in SHG setup. Its green laser output[‡6] is injected to the corresponding arm cavity. The resonant frequency of the arm is sensed with the PDH signal of the green laser. The PDH signal is fed back to the reference frequency of the beat note. Lock of one arm cavity in green can be achieved easily because the finesse of the arm is set relatively low. The green laser transmitting through each arm is extracted on an optical table in the corner station. On the table, beat note of the two transmitted beams and beat note of

[‡5] CARM serves as a single optical cavity with the full interferometer locked.

[‡6] In Advanced LIGO the main laser has wavelength of 1064 nm and thus the frequency-doubled laser has wavelength of 532 nm, which is green.

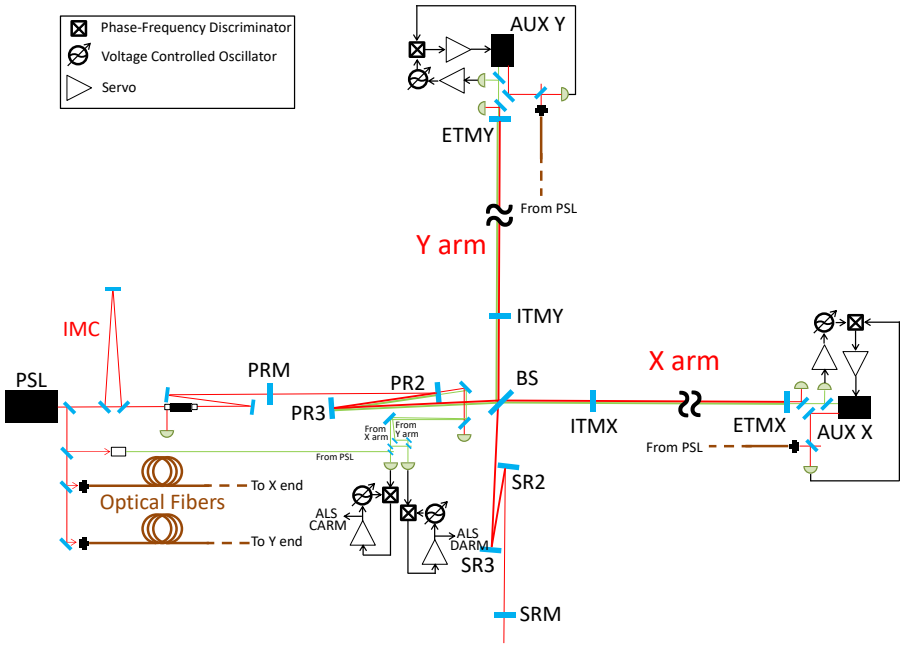

Figure 5.5: Schematic view of the ALS system of Advanced LIGO.

the transmission of the X arm and the second harmonic field of the picked-off PSL are obtained. Each beat note is phase-locked and, by doing so, the DARM signal and the CARM[‡7] signal are extracted from the former and the latter beat notes, respectively.

The lock acquisition scheme of Advanced LIGO with the ALS system is the following (Figure 5.6). First, the resonance of the green lasers in the arms are acquired. Second, CARM and DARM are controlled so that the main laser is kept off-resonant of each arm by certain amount. Third, lock of the dual-recycled Michelson interferometer (DRMI) in the central interferometer is acquired as three DoFs of the DRMI are controlled using the third harmonic demodulation technique. Fourth, the control of CARM and DARM is handed over from the ALS system to the transmission power of the main laser of the arms and the PDH signal of the anti-symmetric port (transmission of the SRM), respectively. Finally, the offset of the main laser frequency with respect to the arm cavity resonances is gradually reduced to switch all the controls to the main laser PDH signals. They achieved the full operation of the DRFPMI with this scheme.

[‡7]In fact, this is not a pure CARM.

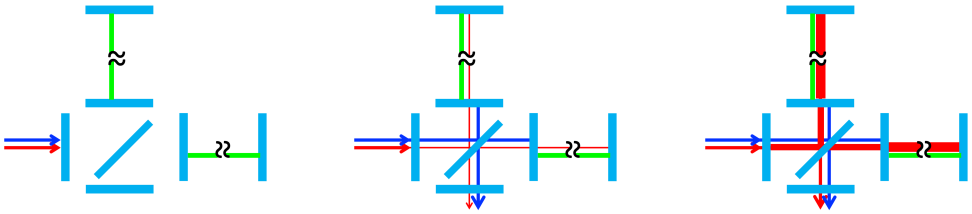

(a) (b) (c)

Figure 5.6: Schematic diagrams of the lock acquisition schemes with ALS. In the step (a), each green laser keeps resonating in the corresponding arm cavity so that the displacement of the arm cavity length can be sensed with respect to the main laser. In (b), the central DRMI is controlled by using the sideband fields while the main laser is kept off-resonant by ALS. In (c), both cavities are brought around their resonances and then the error signal for each DoF is switched to that in the final state.

Putting a focus on the performance of their ALS system, it has been reported that the RMS of the residual frequency fluctuations reached 6 Hz [134] or 8 Hz [135] in the single arm operation, which were significantly smaller than the full linewidth of the single arm, 84 Hz.

Issues

The following issues of the lock acquisition and ALS scheme of Advanced LIGO can be raised.

- The scheme requires the optical fibers have to be laid along the arms. Thus the longer arms in the 3G detectors would force us to use the longer fibers. If a similar ALS scheme is used in the 3G detectors, it is expected that fiber phase noise and optical loss increase, which might harm the overall performance.
- The lock acquisition sequence of CARM consists of multiple steps that use the arm transmission as an error signal. This complicates the lock acquisition process.

In the following chapters, a new ALS scheme that addresses these issues is described after introducing the interferometer of KAGRA, where the new ALS scheme has been implemented and demonstrated.

Chapter 6
CONFIGURATION OF KAGRA

KAGRA is one of the 2G ground-based interferometric GW detectors. While its design sensitivity and size of the arms or test masses are on the same order of those of other 2G detectors, it has unique features that will be keys in the next generation GW detectors, such as underground facility and cryogenic test masses. In this chapter, the configuration of KAGRA is overviewed with a focus on its interferometer, where the new ALS system has been implemented and tested.

6.1 Overview

KAGRA is constructed in the Kamioka mine, Gifu Prefecture, Japan [24]. The detector of KAGRA is built in the L-shaped underground tunnel in the mine. Each point of the tunnel is at least 200 m below the surface of the ground. The purpose of building the detector in underground facility is the following. One is that the level of seismic motion is lower, which is beneficial for both sensitivity and stability. Another is that it is expected that physical conditions such as temperature, humidity, and air pressure are more stable.

Figure 6.1 shows the top view of the whole system of the KAGRA detector. Two arms, namely the X and Y arms, are 3-km long for each. The long vacuum tube is installed in each arm of the L-shaped tunnel. At the both edge of each arm, large cryostats are placed to house the cryogenic payloads for the test masses. The cryostat is, with proper thermal insulation, connected to a vertical vacuum tube reaching the second floor, which is the base of the test mass suspension. At the bottom of five horizontal and vertical seismic isolation stages at room temperature [136], the cryogenic payload is suspended, which is cooled down to approximately 20 K. These test mass suspensions are called *Type-A*. Since the longitudinal motion of the test masses directly becomes dis-

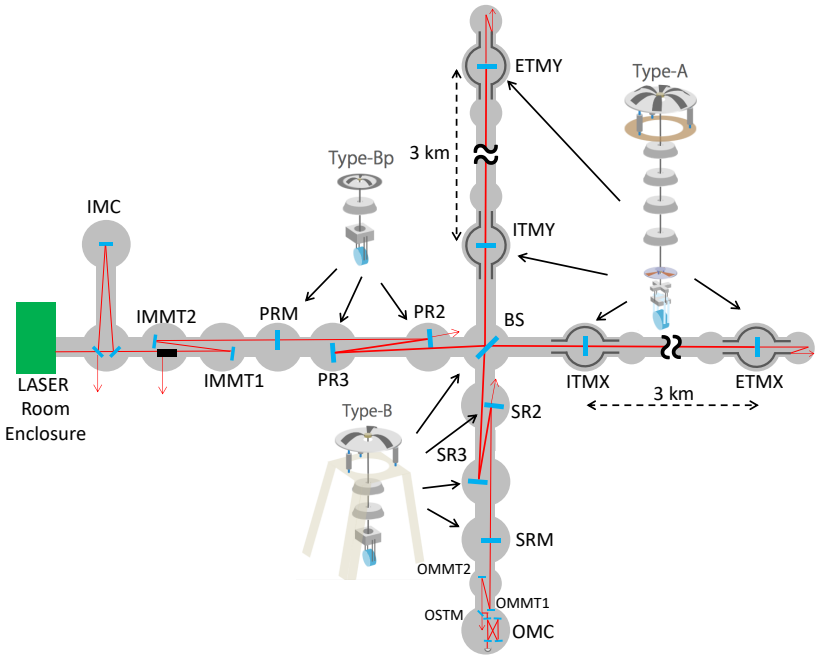

Figure 6.1: Schematic view of the whole system of KAGRA. The suspension system of the core optics are also shown. The gray-colored area represents vacuum tanks and tubes. Each test mass and its payload is surrounded by a cryostat.

placement noise of the detector, the highest seismic isolation is applied to them. The BS and SR mirrors are suspended with *Type-B* suspensions [137]. Compared with Type-A, a Type-B suspension has fewer number of isolation stages and the room temperature payload. The PR mirrors are suspended with *Type-Bp* suspensions [138], which are the simplified version of Type-B. For Type-A and -B, the suspension chain starts from an inverted pendulum while, for Type-A, -B, and -Bp, geometric antispring filters are employed for vertical isolation. Other mirrors labeled as IMC, IMMT1, IMMT2, OMMT1, or OMMT2 are suspended with *Type-C* suspensions, which are simple double pendula that were also used in TAMA300. Most stages including the mirror stage of each suspension have coil-magnet actuators.[‡1]

Figure 6.2 shows the cryogenic suspension of the test mass of KAGRA. Test

[‡1] A magnet is attached to the object one wants to actuate (e.g. a mirror), and a coil is placed correspondingly on the reaction mass. By introducing electrical current in the coil, the force between the magnet and coil can be varied linearly to the applied current.

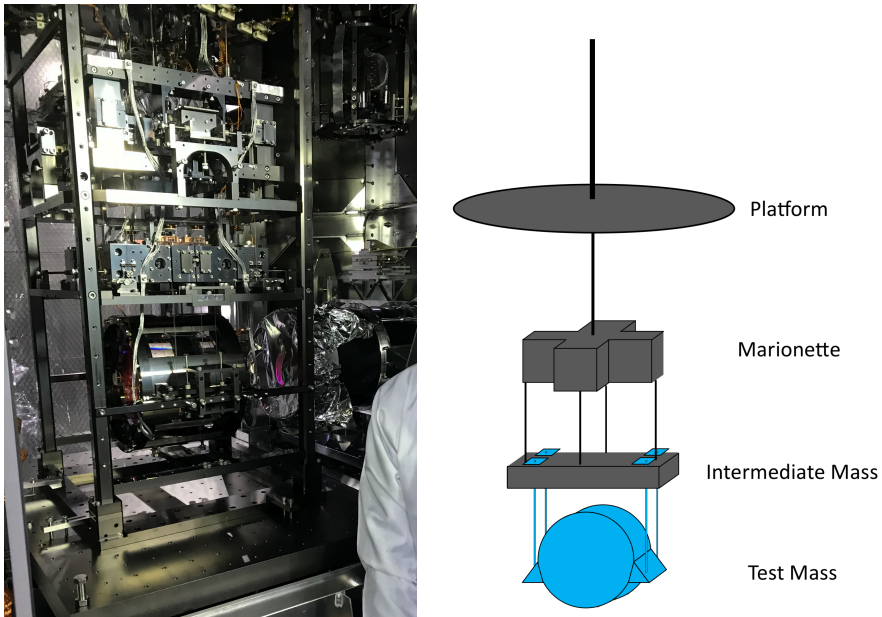

(a) Picture of a cryogenic payload. (b) Schematic view of a cryogenic payload.

Figure 6.2: Picture and schematic view of a cryogenic payload. (a) Picture of a cryogenic payload viewed from side. The test mass chain is surrounded by its reaction mass chain, which is further surrounded by a security frame. (b) Schematic view of a cryogenic payload only showing the test mass chain. Each stage of the marionette, intermediate mass, and test mass is surrounded by its reaction mass. The reaction mass chain is suspended from the platform.

mass is made of sapphire crystal with a weight of 23 kg. The test mass is suspended by four sapphire fibers. The upper edge of each fiber is connected to a sapphire blade, which is attached to the intermediate mass. The intermediate mass is suspended from the marionette stage, which is mainly used for the large-range actuation of longitudinal and angular motion of the test mass.

6.2 Optical configuration

Figure 6.3 shows the optical configuration of KAGRA. KAGRA adopts a DRFPMI as the main interferometer. Tables 6.1 and 6.2 summarizes the parameters

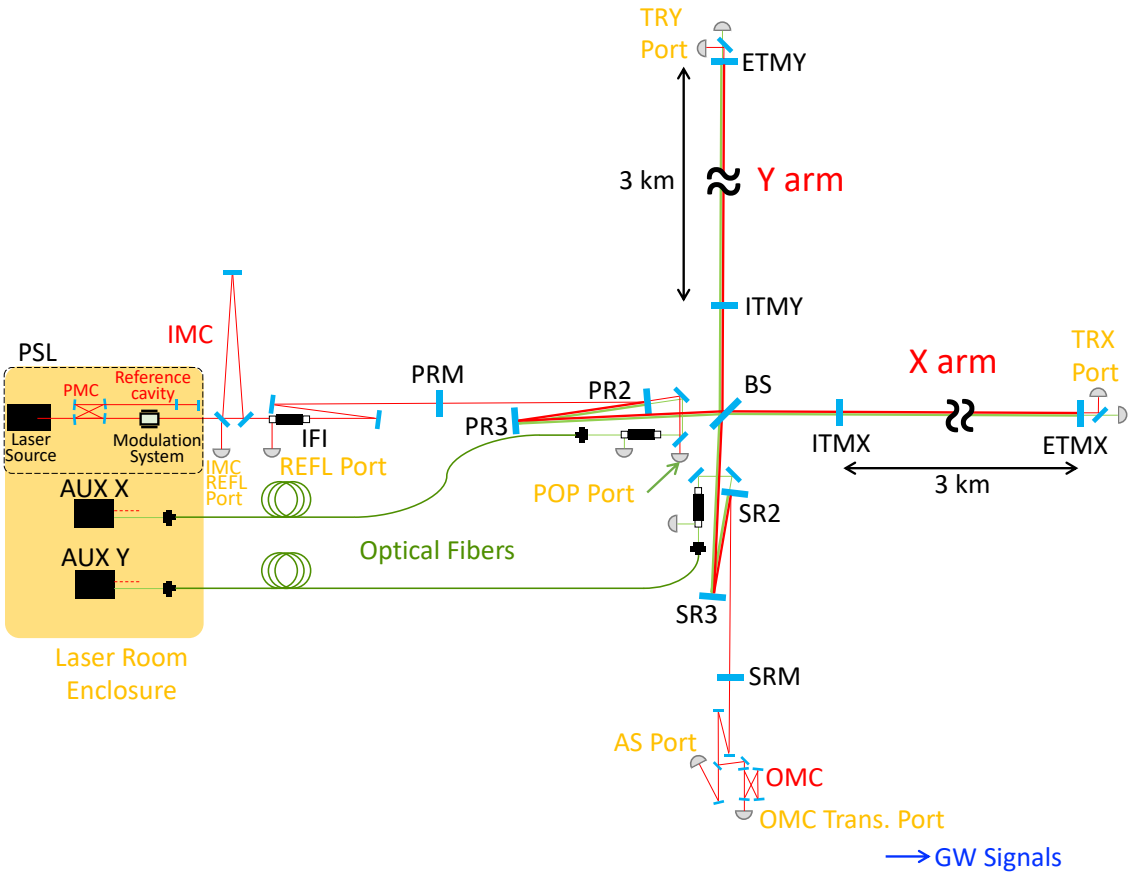

Figure 6.3: Optical configuration of KAGRA.

associated with the main interferometer. The wavelength of the main laser is 1064 nm. The output of the main laser amplifier passes through the pre-mode cleaner (PMC), which is a bow-tie cavity that rejects the junk higher order optical modes and RF amplitude fluctuations of the laser [139]. A fraction of the leakage of the PMC is guided to the reference cavity, which is a stable 10-cm long Fabry–Perot cavity for the frequency reference. The main output of the PMC is sent to the modulation system [140], where phase and amplitude modulation is applied to the main laser. These are the breakdown of the PSL system of KAGRA. After coming out of the laser room enclosure and entering the vacuum tube, the PSL is injected to a triangular optical cavity composed of three suspended mirrors, called the input mode cleaner (IMC) [139]. The IMC has mainly three purposes.

The first is to be a frequency reference of the second stage of the frequency stabilization. The second is to reduce beam jitter of the main laser incident to the main interferometer. The third is to reject higher order optical modes that might have been generated in the modulation system. The transmission of the IMC subsequently passes through a Faraday isolator called the input Faraday isolator (IFI), where the reflection of the main interferometer is extracted. The transmitted beam is then steered toward the main interferometer by a pair of curved mirrors, called input mode matching telescope 1 and 2 (IMMT1 and 2). The power or signal recycling mirrors are composed of three mirrors. The PRM and SRM perpendicularly reflect the beam from the main interferometer, while pairs of PR2 and PR3, and SR2 and SR3 serve as telescopes. They help to make the recycling cavities stable in terms of transverse modes. The transmission of the SRM, which is the output of the main interferometer, is steered by a pair of curved mirrors, called output mode matching telescope 1 and 2 (OMMT1 and 2), and a flat mirror called output steering mirror (OSTM). The beam subsequently propagates through a bow-tie cavity on a suspended breadboard, called the output mode cleaner (OMC). Variations of the transmitted optical power from the OMC corresponds to GW signals detected by KAGRA. The name of each detection port of the optical signals is also described in the figure.

For the purpose of lock acquisition, two auxiliary lasers are placed in the laser room beside the main laser. Each auxiliary laser provides two laser outputs: infrared and green. The infrared beam is the primary output with a wavelength of 1064 nm, which is same as that of the main laser. The secondary output is the green laser, which is produced in the laser head by SHG of the primary beam. Thus it has a wavelength of 532 nm. The two green lasers are delivered via optical fibers to the optical tables placed nearby PR2 or SR2. The fibers have the length of approximately 60 m. The green lasers are injected to the main interferometer from the back side of PR2 or SR2. The BS, PR2 and SR2 have dichroic coating on their front side so that they are transmissive in green at 532 nm. Thanks to these dichroic properties, the lasers from PR2 and SR2 are incident to the X and Y arms, respectively. The transmitted beam of each arm cavity is separated into infrared and green beams by a dichroic mirror, and their optical power is separately detected at TRX or TRY ports.

It is worth mentioning that the finesse of the arm cavities of KAGRA is higher than those of Advanced LIGO and Advanced Virgo approximately by a factor of three. This is mainly because only KAGRA cools its test masses down to cryogenic temperature; less optical power in the central interferometer is preferred given the optical absorption of the substrate of the test mass mirror and

thus the combination of higher finesse of the arm cavities and higher reflectivity of the SRM is preferred.[‡2] This fact makes lock acquisition of KAGRA even more challenging and the arm cavities of KAGRA a suitable test bed of lock acquisition schemes.

Table 6.1: Design and measured values of the main interferometer parameters of KAGRA.

Parameter	Designed	Measured
Arm cavity length [m]	3000 [141]	X: 2999.990(2) [129, 142] Y: 3000.015(1) [143]
Arm FSR [kHz]	(49.96541)	X: 49.96557(4) [129, 142] Y: 49.96517(2) [143]
Roundtrip Gouy phase [deg]	250.75 [141]	X: 250.7(3) [129, 142] Y: 250.9(3) [143]
Arm finesse for 1064 nm	1530 [141]	X: 1410(30) [129] Y: 1320(30) [144]
Arm finesse for 532 nm	51 [145]	X: 41(2) [146] Y: 53(3) [146]
Arm roundtrip loss for 1064 nm [ppm]	100 [141]	X: 86(3) [129] Y: –
PR cavity length [m]	66.591 [141]	–
SR cavity length [m]	66.591 [141]	–
Roundtrip Gouy phase of PR cavity [deg]	33.0 [141]	31(1) [147]
Roundtrip Gouy phase of SR cavity [deg]	35.0 [141]	48(2) [148]
Schnupp assymmetry [m]	3.3299 [141, 145]	–
PRM transmissivity [%]	10 [145]	10.35 [145]
SRM transmissivity [%]	15 [145]	–
IMC length [m]	26.639 [141]	26.65095(2) [149]
IMC finesse	520 [150]	540(70) [151]
Modulation 1 (f_1) [MHz]	16.880962 [141, 145]	16.8732705 [149]
Modulation 2 (f_2) [MHz]	45.015898 [141, 145]	44.995388 [149]
Modulation 3 (f_3) [MHz]	56.269873 [145]	–

[‡2]Please refer to Section 4.3.2 for how RSE balances the optical power in the central interferometer.

Table 6.2: Linewidths of the arm cavities of KAGRA that are derived from the values in Table 6.1.

Parameter	Designed	Measured
Single arm full linewidth for 1064 nm [Hz]	32.7	X: 35.4(7) Y: 37.9(8)
CARM full linewidth [Hz]	1.6	–
DARM full linewidth [Hz]	783	–

Table 6.3: Five length DoFs of a DRFPMI and their sensing signals. The names of the demodulation signals are defined in the following way: X-phase demodulation at k (integer) MHz of the photodetector outputs at *NAME* port is called NAMEkX.

DoF name	Error signal
DARM	OMC TRANS (or AS17Q)
CARM	REFL45I
PRCL	POP45I
SRCL	POP17I
MICH	POP17Q

6.3 Control scheme

In this section, the designed control scheme of the main interferometer in the observation mode is briefly described. For the sensing of length DoFs of the DRFPMI, the main laser is phase-modulated at two different frequencies, namely f_1 and f_2 (Figure 6.4). Defining the FSR of the IMC as f_{IMC}, f_1 and f_2 can be written by $f_1 = 3f_{\mathrm{IMC}}$ and $f_2 = 8f_{\mathrm{IMC}}$. f_1 and f_2 are integer multiple of f_{IMC} so that the modulation sidebands transmit through the IMC together with the carrier field. These frequencies are listed in Table 6.1. As shown also in Table 6.1, the Schnupp asymmetry of the central Michelson interferometer is about 3.33 m. With this asymmetry, f_1 sidebands leak to the SR cavity while f_2 sidebands are perfectly reflected by the Michelson interferometer when the carrier field is at the dark fringe. DARM is controlled with an offset of about $1 - 10$ pm so that a small fraction of carrier field leaks out of the SR cavity, which enables us to sense DARM with the DC readout scheme.

The error signal for each length DoF is listed in Table 6.3. At REFL and POP

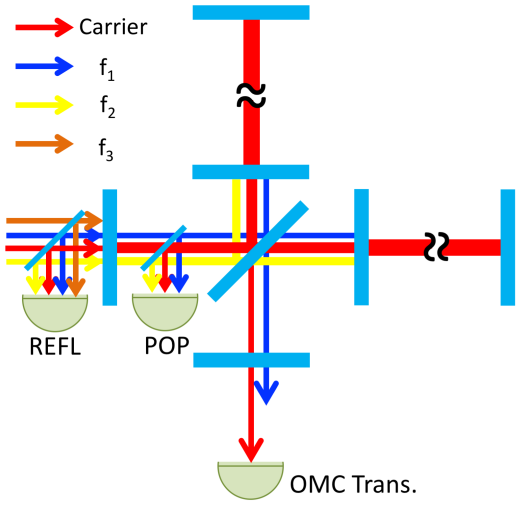

Figure 6.4: Schematic view of the carrier and sideband fields and the detection ports in the main interferometer. The carrier field resonates in the arm cavities and the PR cavity. Due to the DARM offset, a small fraction of the carrier leaks out of the Michelson interferometer and the SR cavity. The f_1 sidebands resonate in the PR-SR coupled cavity while the f_2 sidebands resonate in the PR cavity. At REFL and POP port, the beat notes between the carrier field and the sideband fields are detected.

port, the beat notes between the carrier field and the sideband fields are detected with photodetectors that have a resonant circuit at f_1 and f_2 frequencies so as to have high signal-to-noise ratio. The DARM signal is fed back to the position of one of ETMs with the bandwidth of about 50 Hz. The CARM signal is fed back to the frequency of the main laser by the combination of changing the IMC length and directly actuating the laser frequency with the bandwidth of about 10 kHz. The PRCL, SRCL, and MICH signal are fed back to the position of the PRM, the SRM, and the BS, respectively, with the bandwidth of about 30 Hz.

6.4 Lock acquisition scheme

In this section, the lock acquisition scheme of the KAGRA interferometer, or how to reach the control configuration described in the previous section, is described. The scheme is similar to that of Advanced LIGO. The main differences are the following two. One is that the scheme of the ALS is different. The ALS

scheme of KAGRA is described in the next chapter in detail. The other is that, in the default plan, the amplitude modulation sidebands at the frequency of f_3 are employed in the intermediate steps of lock acquisition [141]. f_3 is equal to $10 f_{\mathrm{IMC}}$. This value is chosen so that the sidebands do not resonate in any cavities of the main interferometer. The use of these non-resonant sidebands of amplitude modulation enables us to realize an improved version of the third harmonic demodulation technique. Let us recall that, in the third harmonic demodulation technique, the variations in the DoFs of the central interferometer are carried by the phase modulation sidebands of f_1 or f_2, and they are sensed with heterodyne readout by using the second order sidebands, which have sideband frequency of $2f_1$ and $2f_2$, as reference fields; the signals in the photodetector outputs are consequently around $3f_1$ or $3f_2$ (Specifically, REFL51I/Q and REFL135I). Since the $2f_1$ and $2f_2$ sidebands are amplitude modulation,[‡3] it is possible to sense the same signals by alternatively preparing new amplitude modulation sidebands. This is the working principle of this scheme. The signals of the length DoFs appear around $f_3 \pm f_1$ or $f_3 \pm f_2$ instead. The advantage of this scheme is that the signals are further separated from the dynamics of arm cavities compared with the third harmonic demodulation technique; the beat note between the carrier field, which carries the signals from the arm cavities, and the third order sidebands pollutes the signals in the third harmonic demodulation technique. KAGRA employs a pair of Mach–Zehnder interferometers to generate amplitude modulation only from electro-optic modulators (EOMs), each of which is a phase modulator [140].

[‡3] Phase modulation at f is inevitably accompanied with amplitude modulation at $2f$.

Chapter 7
KAGRA TYPE ALS

In this chapter, a newly developed ALS scheme that is used in KAGRA is described in detail. First, the design of the scheme is explained. Second, the implemented optics and circuits associated with the ALS system are overviewed. Third, the demonstration of the lock acquisition scheme of KAGRA using the ALS system is described. Finally, the characterized performance of the ALS system is explained. The works covered by the present chapter were primarily done by the author of the dissertation.

7.1 Requirements

As mentioned in Section 5.3.2, for smooth handing over from the ALS system to the main laser signals, the ALS system has to be capable of suppressing the fluctuations of the main laser frequency below the full linewidth of a single arm cavity. This requirement can be quantified by the condition that the RMS of $\Delta f_{\rm res}(f;\kappa_{\rm ARM})$ is below the full linewidth of the arm, where

$$\Delta f_{\rm res}(f;\kappa_{\rm ARM}) = [\Delta f_{\rm main}(f) - \Delta f_{\rm ARM}(f)]L(f;\kappa_{\rm ARM}), \tag{7.1}$$

$$L(f;\kappa_{\rm c}) = \frac{1}{1+if/\kappa_{\rm c}}. \tag{7.2}$$

Here $\kappa_{\rm ARM}$ is the (half) linewidth of the arm, $\Delta f_{\rm main}(f)$ and $\Delta f_{\rm ARM}(f)$ are the frequency fluctuations of the main laser entering the main interferometer and the resonance of the arm, respectively, and $L(f;\kappa_{\rm c})$ is the transfer function of a low-pass filter with a corner frequency of $\kappa_{\rm c}$. We here consider the low-passed fluctuations because the error signal of the arm cavity senses these low-passed fluctuations[‡1] and thus its RMS has to be compared with the linewidth of the

[‡1] Please refer to Equation (4.23).

Table 7.1: Main differences between the ALS systems of KAGRA and Advanced LIGO.

	KAGRA	Advanced LIGO
Green laser injection site	Central area	End stations
Optical fibers	Within the central area	Along the arms
Signals of the arm DoFs	Summations in electronics	Optical beat notes
Number of optical sensors	4 (or 6 [a])	6
Number of SHG setups	2	3

[a] If the fiber noise cancellation loops are involved.

arm. In the case of KAGRA, the full linewidth of the single arm cavity is 33 Hz,[‡2] and thus the requirement on $\Delta f_{\rm res}(f;\kappa_{\rm ARM})$ is 33 Hz (Table 6.2). This value is smaller than that of Advanced LIGO, which is 84 Hz [22].

While the above requirement is the primary target of the frequency stability by the ALS system, the more ambitious target can be given by the CARM linewidth. This target can be quantified by the condition that the RMS of $\Delta f_{\rm res}(f;\kappa_{\rm CARM})$ is below the full linewidth of CARM, where

$$\Delta f_{\rm res}(f;\kappa_{\rm CARM}) = [\Delta f_{\rm main}(f) - \Delta f_{\rm CARM}(f)]L(f;\kappa_{\rm CARM}). \tag{7.3}$$

Here $\kappa_{\rm CARM}$ is the (half) linewidth of CARM, and $\Delta f_{\rm CARM}(f)$ is the fluctuations of the resonant frequency of CARM. In the case of KAGRA, the full linewidth of CARM is 1.6 Hz (Table 6.2). If the condition is satisfied, it is possible to directly hand over the CARM control from the ALS system to the main laser PDH signal obtained at REFL port, which will greatly simplify the whole lock acquisition process.

As is also mentioned, an requirement is imposed on the range of the frequency actuation of the auxiliary lasers. Since the RMS of the arm length fluctuation due to seismic motion is about 2 μm on a noisy day at the KAGRA site [152], the range has to be larger than 0.2 MHz.

7.2 Design

The ALS scheme of KAGRA is different from that of Advanced LIGO in their concepts, designs, and control strategy. As explained in the previous chapter,

[‡2] This corresponds to 0.35 nm in terms of the cavity length displacement.

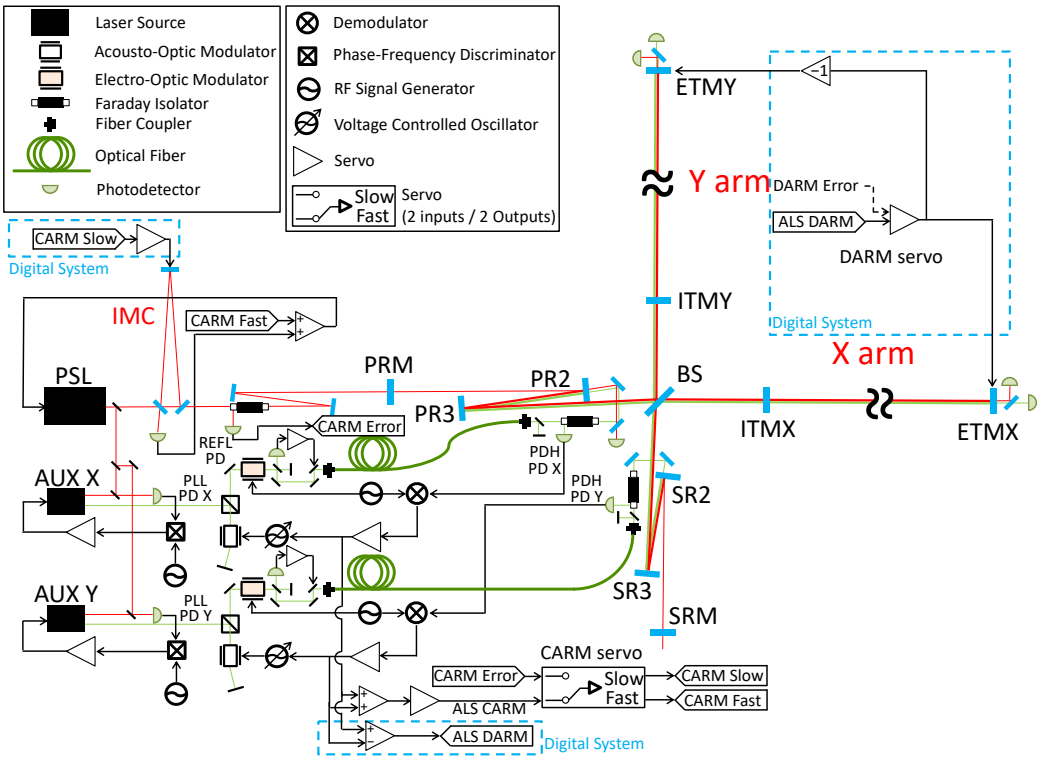

Figure 7.1: Schematic view of the ALS system of KAGRA.

KAGRA employs the green laser beams injected from the central area of the interferometer, instead of the other ends of the arm cavities. This made the control configuration simple by eliminating the long optical fibers along the kilometer-long arms. The main differences of them are summarized in Table 7.1. This section covers the design of the optical and control configuration of the ALS system and the noise budget design of the system.

7.2.1 Optical and servo topology

Figure 7.1 shows the optical and control topology of the ALS system. Let us first summarize the working principle before going into the detail. First, phase-locked loops (PLLs) make the frequencies of the infrared outputs of the auxiliary lasers follow the PSL frequency with certain offsets. The frequency of the green laser from each auxiliary laser follows the resonant frequency of the corresponding arm by using the combination of a voltage controlled oscillator (VCO) and a

double-path acousto-optic modulator (AOM) as a frequency actuator. At this point, on the assumption that the auxiliary laser is tightly locked to the PSL via the PLL, each control signal applied to the frequency actuator is equivalent to the difference between the PSL frequency and the arm resonant frequency. Therefore, CARM can be sensed by the sum of the two control signals while DARM by the difference between the two. Such error signals are called ALS CARM and ALS DARM. ALS CARM is fed back to the PSL frequency while ALS DARM is to (differential) arm cavity lengths, so as to achieve the control of the two length DoFs of the arm cavities. By this control, the main laser frequency is fixed to certain points with respect to the resonances of the arm cavities. The positions of the resonances are adjusted by the frequency offsets in the PLLs of the auxiliary lasers.

The detail of the system can be described as follows. For the PLLs of the auxiliary lasers, beat notes between the PSL and the infrared output of the auxiliary laser are detected by photodetectors (denoted by PLL PD X and Y in the figure). At phase-frequency discriminators, the signals from the beat note photodetectors are demodulated by mixing them with local oscillator (LO) signals from RF signal generators. One can adjust the auxiliary laser frequency with respect to the PSL frequency by changing the LO frequency. To close the PLL, each demodulated beat note signal is filtered by an analogue servo circuit and then fed back to the frequency of the auxiliary laser. The frequency actuation is achieved by the piezoelectric transducer attached to the laser cavity, accompanied with the temperature control for drift compensation. The green laser output from the laser head of each auxiliary laser is frequency-shifted by a double path AOM. Successively, phase modulation is applied by an EOM in the laser room enclosure for signal extraction via the PDH technique. After delivered via the optical fibers, they are injected to the X and Y arms from the rear side of PR2 and SR2, respectively. The reflection from each arm cavity is extracted by a Faraday isolator and detected by a photodetector (PDH PD X or Y) on the optical table (POP or POS table, respectively) to provide the PDH error signal. Each PDH error signal is filtered by another analogue servo circuit and then fed back to a low-noise VCO that drives the AOM. The two control signals of the PDH loops are combined to obtain the ALS CARM and ALS DARM error signals. The CARM loop partially involves analogue control filters, while the DARM loop is entirely realized by a digital control, because the CARM loop requires wide control bandwidth up to about $1-10\,\mathrm{kHz}$. Then an extra analogue circuit is used for adding the two control signals and successively applying a low-pass filter to the summation, in order to to synthesize the ALS CARM error

signal in such a way that its frequency response is matched with the main laser CARM signal (REFL CARM). The REFL CARM and ALS CARM are sent to the same analogue servo board named the CARM servo so that the two input signals can be gradually switched to accomplish smooth hand-over from the ALS system to the main laser PDH signal. The CARM servo has two output ports named slow and fast outputs. The slow output is fed back to the IMC length while the fast output is to the error point of the IMC control loop. Combining two feedback paths enables us to form a dual loop CARM control [153]. Meanwhile, for the DARM control, the two control signals of the arm PDH loops are sampled and digitally processed by real-time digital controllers. The output of the digital controller is fed back differentially to the ETM motion. Once the ALS CARM and ALS DARM loops are fully engaged, the resonant frequency of each arm cavity can be tuned to a desired position with respect to the PSL frequency by changing the LO frequency for the corresponding PLL.

In addition to the main control loops of the ALS system, optics and servo for the cancellation of fiber phase noise are prepared; what is called fiber phase noise here is phase fluctuations the lasers pick up as they propagate through the optical fibers. For the purpose of this cancellation technique, a small fraction of each green laser is picked off and immediately reflected back between the EOM and the fiber coupler in the laser room enclosure. Another small fraction is also picked off and reflected back from POP or POS table to the laser room. The interference of the two reflection is detected in the laser room, and the fringe of it can be controlled to mid-fringe by feeding back the detected fringe signal to the optical path length; a piezoelectric transducer is attached to the mirror immediately before the fiber coupler so that its position can be actuated. This control is secondary in the sense that it can improve the noise performance of the ALS system if fiber noise limits the noise level but it is not indispensable for the control topology of the ALS system.

The features of the KAGRA ALS can be summarized as follows. The first feature is that auxiliary green lasers are injected from the corner station, as opposed to the end stations. Thanks to this feature, the optical fiber length is not on the same order to the arm length but can be significantly shortened to the level of approximately 60 m, which makes the system scalable to the 3G detectors [8,89]; fiber phase noise and optical loss do not increase even if the arm cavity length gets long. Moreover, it is also realistic to even eliminate optical fibers in the configuration of the KAGRA-type ALS. The second is that the configuration is simple in the sense that the number of SHG setups is less. If the fiber noise cancellation is not used, the number of the involved sensors is

also less. The third feature is that the ALS CARM and ALS DARM signals are produced by summing the two signals from two arms in electronics or real-time controllers, respectively. This increases the flexibility of the ALS control loops, compared to the case where these signals are obtained with optical beat notes.[‡3]

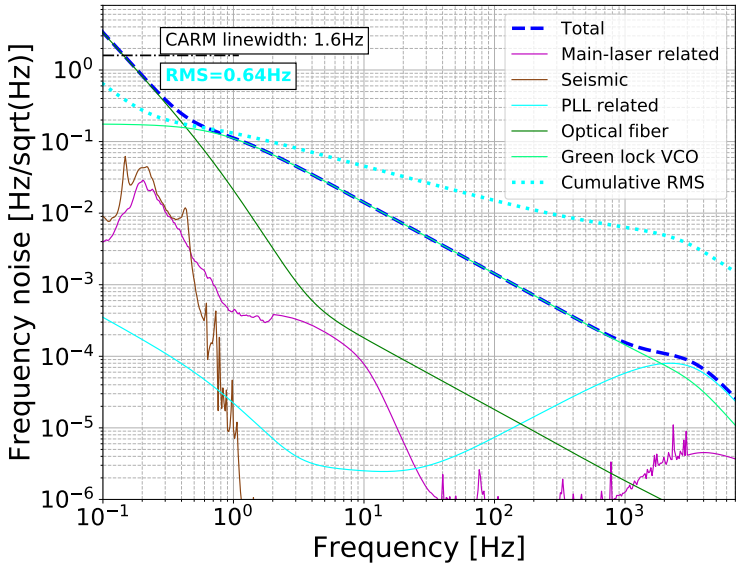

Figure 7.2: ASDs of the simulated noise spectra of the ALS system in design. The blue dashed line shows total noise: quadrature sum of the contributions of all the noise sources considered in the design study. The magenta line shows the total contributions of noise related to the PSL and its frequency stabilization. The brown line shows the estimated residual contribution of arm length fluctuations caused by seismic motion. The solid cyan line shows the contribution from the PLLs of the auxiliary lasers including free-run frequency fluctuations of the auxiliary lasers. The green line shows the contribution of phase noise caused by the optical fibers for the green lasers. The light green line shows the contribution of phase noises of the VCOs. The light blue dotted line shows the cumulative RMS of the blue dashed line integrated from the high frequency side. The RMS integration is bounded by 0.1 Hz because we assumed that the control hand-over lasts for 10 s at most.

[‡3]In the case of Advanced LIGO, the true CARM cannot be sensed by their ALS system.

Table 7.2: Design of the control bandwidth of each loop of the system. The unity gain frequencies (UGF) are shown.

Loop name	UGF
PLL	20 kHz
Arm PDH loop	20 kHz
ALS CARM loop	10 kHz
ALS DARM loop	25 Hz

7.2.2 Noise Design

In order to verify the design of the whole ALS system, we numerically simulated the noise performance of the ALS. The noise design of the KAGRA ALS system is described here.

We numerically simulated the noise contributions in the KAGRA ALS system in the frequency domain. The servo loops were also simulated and designed. The conditions and assumptions of the simulation are summarized in Tables 7.2 and 7.3. The simulation results of the noise contributions to residual frequency fluctuations of the main laser with respect to the CARM resonance are shown in Figure 7.2. The spectra of $\Delta f_{\mathrm{res}}(f;\kappa_{\mathrm{CARM}})$ are computed by using a commercial software, Simulink. The constructed Simulink model is available here [154]. The calculation results show that, in the designed system, the RMS of the residual frequency fluctuations with the ALS control can be as low as 0.64 Hz, which is smaller than the CARM linewidth. The dominant noise contribution above about 1 Hz was expected to come from frequency noise of the VCOs. Below 1 Hz, it was expected that phase noise of the green lasers introduced by the optical fibers was dominant. We also confirmed that the primary noise requirement can be achieved; the RMS of $\Delta f_{\mathrm{res}}(f;\kappa_{\mathrm{ARM}})$ is 2.0 Hz and so smaller than the linewidth of the single arm cavity, 33 Hz.

Fiber phase noise had been estimated based on a measurement of phase noise of an optical fiber of length of 5 m placed on an optical table (Appendix F for the detail). We scaled the measured level of phase noise in such a way that the PSD of fiber phase noise is proportional to the fiber length. Since it was expected that the contribution of fiber phase noise was not critical in achieving the requirement based on the preliminary measurement, the fiber noise cancellation loop was not included in the simulation work.

Table 7.3: List of major noise sources and design magnitude of them.

Noise source	ASD at 1 Hz	Note
Optical fiber	$0.01\,\mathrm{Hz}/\sqrt{\mathrm{Hz}}$	Appendix F
VCO	$0.5\,\mathrm{Hz}/\sqrt{\mathrm{Hz}}$	Extrapolation from LIGO VCO [155] with a safety factor of 10
Arm length fluctuations	$3\times10^{-9}\,\mathrm{m}/\sqrt{\mathrm{Hz}}$	[152]
Free-run frequency noise of the auxiliary laser	$1\times10^{5}\,\mathrm{Hz}/\sqrt{\mathrm{Hz}}$	$1/f$ dependency [156]
PSL frequency noise	$1\times10^{4}\,\mathrm{Hz}/\sqrt{\mathrm{Hz}}$	Calculated from [152]

7.3 Implementation

In this section, first, the configuration of each control loop in the ALS system that has been installed in KAGRA is overviewed. Successively, optical and electrical components in the actual system are described in detail. Comprehensive information of the components such as the product numbers can be found in Appendix G.

7.3.1 Control loops

Here, the control loops that are the building blocks of the whole system are explained; they are the PLLs between the main and auxiliary lasers, the arm cavity loops of the auxiliary lasers, fiber noise cancellation loops, and ALS CARM and DARM loops. Sensors, servo filters, and actuators of them are described below (Figure 7.3).

Phase-locked loop

The sensor of the PLL is a photodetector. It receives the interference fields between the main laser and one of the auxiliary lasers. Its photodiode converts the received optical power into electrical current, and the circuit part of the photodetector then converts the current into voltage signal. The output of the photodetector is typically at several tens of megahertz.

The raw output of the photodetector is then demodulated at the phase-frequency discriminator by mixing it with local oscillator signal. The demodulated signal, which is typically down-converted below about 1 MHz, is regarded

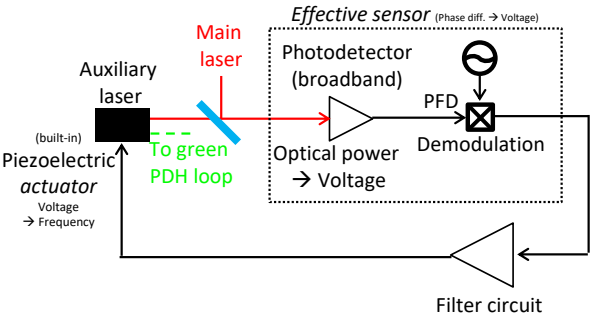

(a) Phase-locked loop.

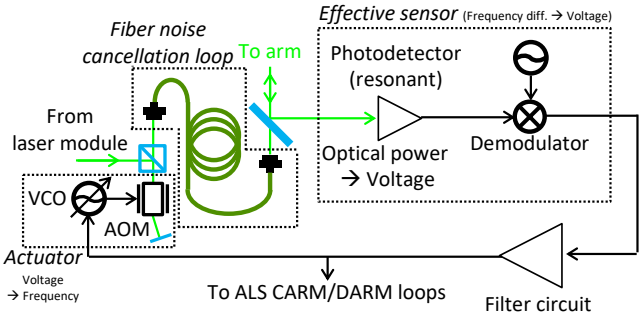

(b) Green PDH loop.

Figure 7.3: Schematic diagram of the subcomponent loops of the system. The configuration of the fiber noise cancellation loops is shown in Figure 7.7.

as the error signal of the PLL; it is proportional to the relative phase deviations between the main and auxiliary lasers.

The demodulated voltage signal is then sent to a filter circuit ("universal analogue circuit" described below). The circuit is a series of variable gain amplifier stages and filter stages with zeros and poles, which are realized with operational amplifiers.

The output voltage signal of the filer circuit is sent to the laser module of the auxiliary laser, which eventually drives piezoelectric actuator of the laser cavity to actuate the laser frequency. The effective frequency bandwidth of the frequency actuation is about 100 kHz, since there is a bunch of mechanical resonances above $\sim$ 200 kHz.

Green PDH loop

The sensor of the arm cavity loop of the green laser is also a photodetector. It receives the reflection fields of the arm cavity, which are the interference between the carrier and the phase-modulation sideband fields. The photocurrent generated at the photodiode is converted into voltage signal via a resonant circuit. Its resonant frequency is tuned at the frequency of the phase modulation.

The raw output of the photodetector is demodulated at a mixer circuit to produce the PDH signal. The frequency band of the signal is below about 1 MHz. The PDH signal is proportional to the difference between the auxiliary laser frequency and the resonant frequency of the arm. The PDH signal is then sent to a similar filter circuit.

The output voltage signal of the filter circuit then drives a VCO. The VCO drives an AOM, which shifts the frequency of the green output of the auxiliary laser. As a whole, the amount of the frequency shift is proportional to the output voltage of the filter circuit.

Fiber noise cancellation loop

The sensor of the fiber noise cancellation loop is a subtraction[‡4] of the outputs of two photodetectors, which sense DC optical power of two ports of a Michelson interferometer. The Michelson interferometer is designed to be sensitive to the optical length variations in the optical fiber for the green laser. The sensor output is then filtered in a similar filter circuit.

The output voltage signal of the filter circuit is amplified by a high-voltage amplifier with the output range of $0 - 150\,\mathrm{V}$. The amplified signal drives a piezoelectric actuator attached to a mirror so that the motion of the mirror compensates the optical length variations.

ALS CARM and DARM loops

The effective sensors of the ALS CARM and ALS DARM loops are the control signals of the green PDH loops, which are the voltage signals applied to the VCOs. As for the ALS CARM loop, the error signal is filtered by a similar analogue filter circuit. As for the ALS DARM loop, the filtering is performed in digital real-time controllers.

There are two actuators in the ALS CARM loop. One changes the length of the IMC. The length of the IMC is actuated by pushing one mirror of the IMC

[‡4]The subtraction is actually done in the filter circuit downstream.

(MCe; a suspended mirror placed at the far end of the IMC) with coil-magnet actuators. Since the control system of the IMC forces the PSL frequency to follow the IMC resonance, changing the IMC length actuates the PSL frequency via the IMC control. The other injects the voltage signal into the error point of the IMC control. This injection biases the IMC control and thus actuates the PSL frequency through the control.

The actuator of the ALS DARM loop changes the lengths of the arm cavities. The length of the arms are actuated by pushing one or more ETMs with coil-magnet actuators. The test mass stage is used for the higher frequencies while the marionette stage is used for the lower frequencies.

7.3.2 Optics

Laser room

In the laser room enclosure, a large optical table with the dimension of 1500 mm by 4800 mm is placed, which is called the PSL table (Figure 7.4). One corner of the table (in the +x and +y side in the interferometer frame) is assigned for the optics associated with the ALS system. Figure 7.5 shows the layout of such optics. Important optical components among them are introduced in the following.

Two free-space laser modules are fixed on the table. They are commercial products named Prometheus from Coherent Inc., which are based on non-planar ring oscillator configurations and have a SHG setup inside so that each module has infrared and green laser outputs. The power of the infrared output is about 1 W while that of the green output is about 100 mW. For detection of beat notes between the PSL and the auxiliary lasers, we employed commercial broadband photodetector units with silicon photodiode. The reason why we chose silicon photodiode, which has fast response but relatively low responsivity for 1064 nm (compared to InGaAs, for example) is that there is a lot of optical power on the photodiodes thanks to the new configuration of ALS.[‡5] About the use of the AOMs, it is worth noting that the "minus" first order diffraction is chosen for the X arm beam while the "plus" first order diffraction is used for the Y arm beam; here we defined the terminologies of the "plus" and "minus" first order diffractions in such a way that the "plus" one has higher frequency than that

[‡5]In the ALS of Advanced LIGO, the optical power of the green beat notes are limited for two reasons. One is that the power of the green lasers produced by the SHG setup is not high. The other is that the auxiliary green lasers for the beat notes are the transmission of one of the arm cavities

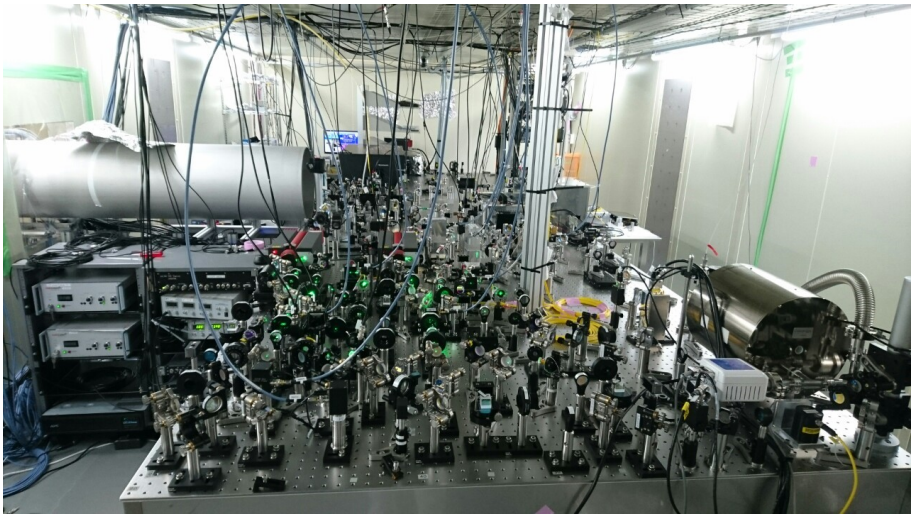

Figure 7.4: Picture of the PSL table focusing on the ALS part. Yellow-colored jacketed fibers can be found in the middle.

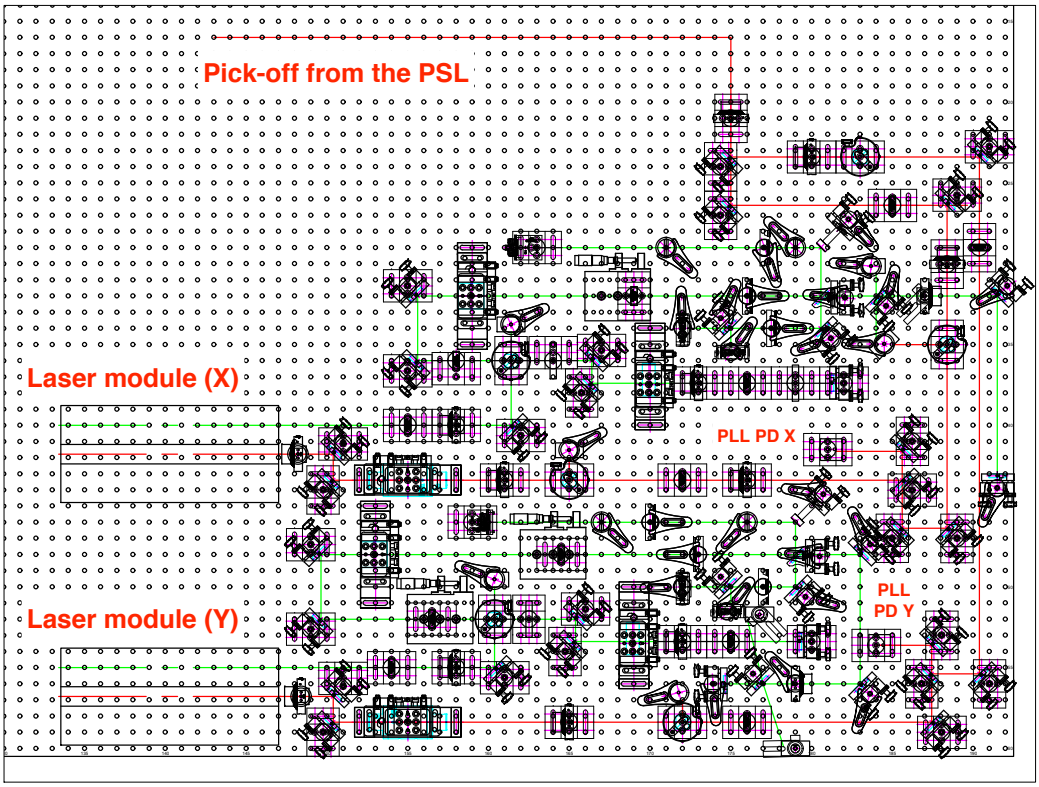

Figure 7.5: Layout of the optics for the ALS system on the PSL table.

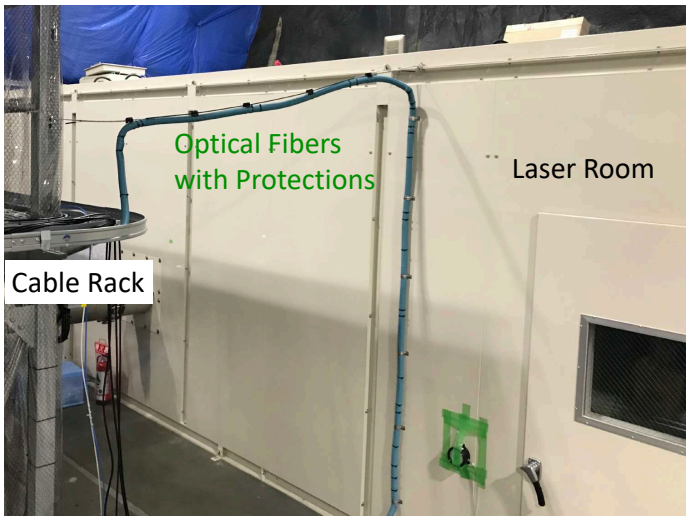

Figure 7.6: Picture of how the optical fibers are laid outside the laser room enclosure. The tubes that have the fibers in them are laid on cable racks and the walls of the laser room.

of the input beam while "minus" one has lower frequency. This selection leads to opposite efficiencies of the frequency actuations. Thanks to this feature, the positive bias voltages applied to the VCOs are compensated with each other at the very first stage of the analogue ALS CARM servo. We laid a pair of optical fibers for green laser for each arm.[‡6] Each fiber has length of about 60 m. Both ends of the fiber are end-capped to avoid damage of the surfaces. The bare fiber is protected by protective outer jacket, which is further wrapped in corrugated tubes together with shock absorbers outside the laser room or the areas around POP or POS table (Figures 7.4 and 7.6). The jacketed optical fibers are laid vertically along rigid pillars standing on the optical tables from the tables to ceiling cable racks. The interferometer configuration of the fiber noise cancellation system is described in Figure 7.7. It employs a polarization Michelson interferometer controlled at mid-fringe. This interferometer locks the fluctuations of the propagation phase of the laser in the longer arm, which includes the fiber, with respect to that in the shorter arm.

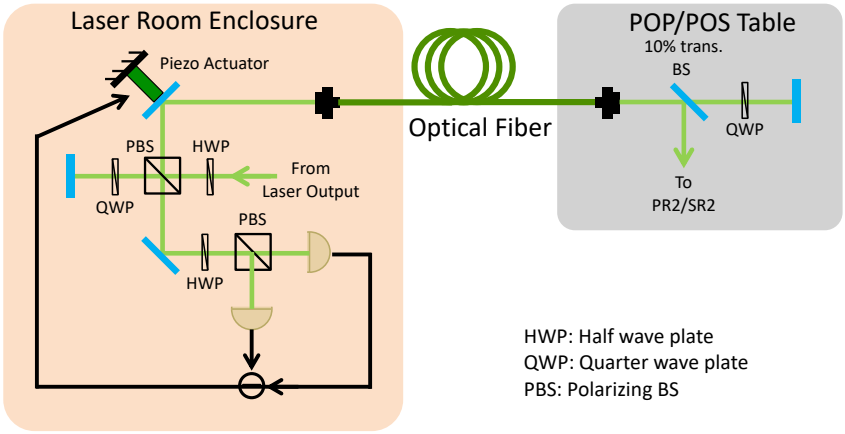

Figure 7.7: Configuration of the polarization Michelson interferometers for the cancellation of fiber noise.

POP/POS table

Figures 7.8 and 7.9 show the layout of optics on POP and POS tables, respectively. Photodetectors on the tables for the PDH signals of green are resonant-type circuits. For this purpose, we modified standard RF photodetectors of KAGRA [157] so that the resonant frequencies are 33 MHz and 32 MHz for the X and Y arm, respectively. We also swapped the photodiodes from InGaAs ones to silicon ones. The last (horizontal) steering mirrors on the tables have dichroic coatings so that they reflect green beams (532 nm) but transmit infrared (1064 nm). Their mirror mounts have two piezo-motor actuators for each for their remote alignment adjustment. On POP table, the transmission of this mirror is used for POP port of the main interferometer. There is a pair of dichroic mirrors to form a periscope at the edge of each table. After the periscopes, the green beams are injected to vacuum chambers through glass viewports with anti-reflective coatings. As shown in Figure 7.1, we have one steering mirror in vacuum immediately behind PR2 or SR2 (Figure 7.10). These mirrors also have two piezo-motor actuators.

[‡6]Four fibers for green are laid in total.

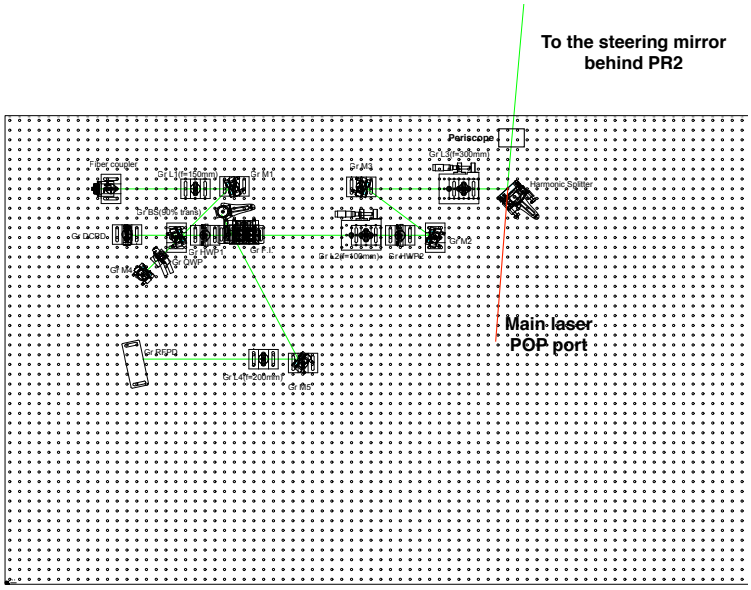

Figure 7.8: Layout of the optics for the ALS system on the POP table.

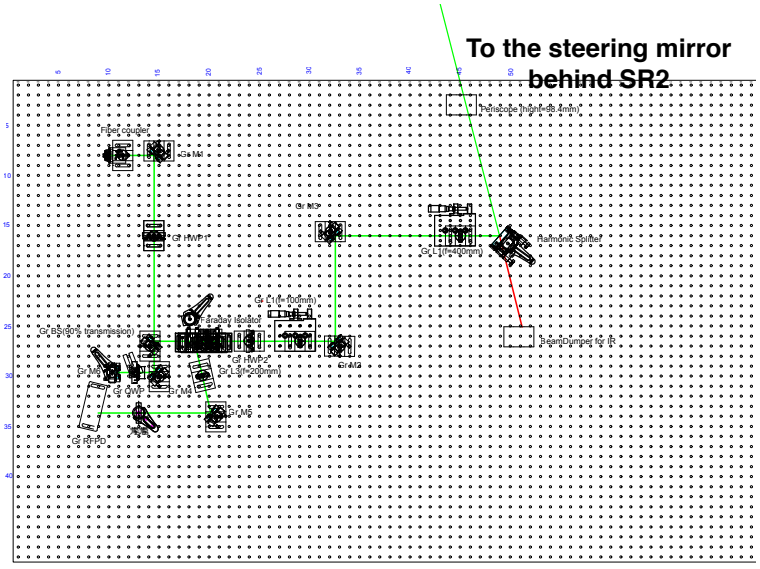

Figure 7.9: Layout of the optics for the ALS system on the POS table.

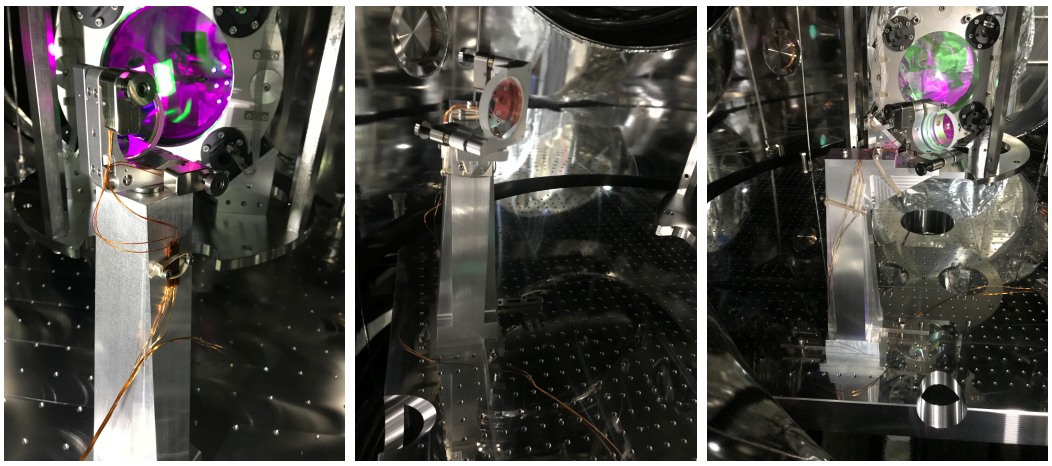

(a) Behind PR2. (b) Behind SR2. (c) Another view behind SR2.

Figure 7.10: Pictures of in-vacuum steering mirrors behind PR2 and SR2.

7.3.3 Circuits

Phase-frequency discriminator

For demodulations of the beat notes of the PLLs, we made and used the circuit modules of phase-frequency discriminator. This circuit outputs the voltage signal proportional to the phase difference between the beat note and the LO if their frequencies are identical. The output is positive or negative constant voltage at a certain value depending on whether the frequency of the beat note is lower or higher than the LO frequency, respectively, if their frequencies are different. This functionality enables us to easily bring the frequency of the auxiliary laser close to that of the PSL when it gets far away.

RF signal generator

In the ALS system, different commercial RF signal generators are employed for three different purposes. The first purpose is the LO of the PLLs. Stable signal generators, E8663D from Keysight Technologies, are used for this purpose. Since phase noise of the LO directly becomes sensing noise of the ALS system, so it is desirable that the noise level of the LO is low. They provide a stable RF signal with the phase noise level as low as $1.6 \times 10^{-4}\,\mathrm{rad}/\sqrt{\mathrm{Hz}}$ in the condition that the carrier frequency is between 250 kHz and 250 MHz and the sideband frequency is 1 Hz [158]. They can also sweep the output frequency in a phase-continuous

way upon remote control commands so that the operation point of the ALS (the PSL frequency with respect to the arm cavity resonance) can be smoothly changed without disturbing the whole control loops. The LO frequencies are set around 40 MHz and 46 MHz for the X and Y arms, respectively. The second purpose is the phase modulation and demodulation for the arm PDH signals. The frequencies for the X and Y arm are chosen to be 33 MHz and 32 MHz, respectively. The third purpose is the frequency reference for the VCOs, which is described in the section of VCO.

Demodulator

The demodulator circuit modules employed for the green PDH signals are standard ones in KAGRA. These ones have the smaller phase delay in the high frequency region among the two types of demodulator modules that KAGRA has [159]. Amplification circuits of LO signals, frequency mixers, and low-pass filters for the demodulated signals are built in a single chassis. This module outputs I- and Q-phase demodulations and the relative phase between the signal applied to the EOM and the LO signal was adjusted so that the PDH error signal did not leak in the Q-phase signal. The relative phase can be remotely adjusted by a voltage-controlled phase shifter.

VCO

Phase noise of the output of the VCO circuit also directly leads to sensing noise of the ALS system. Thus we made our own VCO circuits by simplifying the design of those in Advanced LIGO. Figure 7.11 shows the conceptual diagram of the VCO. The frequency division by ten reduces phase noise of the seed VCO by a factor of ten at the cost of the reduction of the actuation range by the same factor. For the constant frequency reference, another stable RF generator is used for both arms in common. The output of the reference is set to 70.35 MHz so that the output of the VCO unit is around 80 MHz, which is the nominal operating frequency of the AOMs. Their actuation efficiency and range of frequency were characterized. The efficiency is 0.42 MHz/V – 0.43 MHz/V and the range is about 1 MHz, which satisfies the requirement on the actuation range of the whole ALS system. Phase noise of the output was also characterized. The details of these preliminary measurements of the VCOs are described in Appendix F.

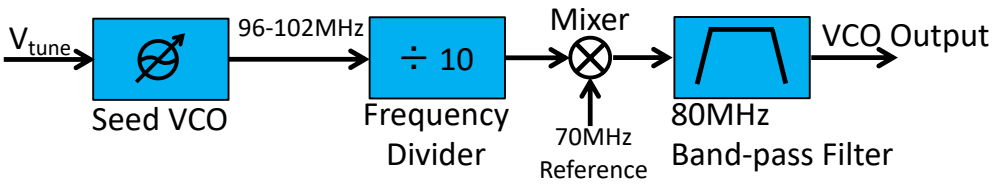

Figure 7.11: Conceptual diagram of the VCO circuit. The output frequency of the seed VCO is adjusted linearly by the input voltage labeled as $V_{\rm tune}$. After the frequency division, the frequency of the signal is then raised to the desired value by the combination of frequency mixing and band-passing.

Universal analogue circuits

Universal analogue circuits are employed in the servos of the PLLs, PDH loops, fiber noise cancellation loops, and CARM loop. Use of analogue circuits enables us to have wide control bandwidths in these loops up to tens of kilohertz. The features of them can be summarized as follows. The input and output ranges of the circuit are $\sim \pm 13\,\mathrm{V}$. The input equivalent noise level is $\sim 1 \times 10^{-7}\,\mathrm{V}/\sqrt{\mathrm{Hz}}$. The targeted frequency band is below $\sim 1\,\mathrm{MHz}$. The circuit has two input ports and two output ports. Each input port has a variable gain amplifier stage and a switchable inverter. One output port is DC-coupled, namely the slow path, while the other is AC-coupled, namely the fast path, which we utilize only for the CARM loop. There are several switchable integrator stages in the common path for the purpose of gain boost in the low frequency region. The common path is then split into the slow and fast path, where we also have a few switchable filters. The variable gain stages and the switchable filters can be controlled remotely via binary outputs of the real-time controllers.

Digital real-time controller

KAGRA uses digital real-time controllers that were originally developed in LIGO. The sampling frequency of this system is 16384 Hz.[‡7] The voltage signals acquired by analogue-digital convertors are processed in real-time controllers and output by digital-analogue converters. How the signals are processed in the controllers is programmed by users before the programs are run. The important feature

[‡7] The sampling frequency can be set as high as 65536 Hz though it is usually set to 16384 Hz or less.

here is that parameters of the programmed process such as the parameters of finite impulse response filters and matrix elements can be changed while they are running. This feature enables us to dynamically and flexibly change the configuration of the control loops as the lock acquisition process proceeds. The states of analogue circuits such as the switches and gains are also governed by the digital controllers.

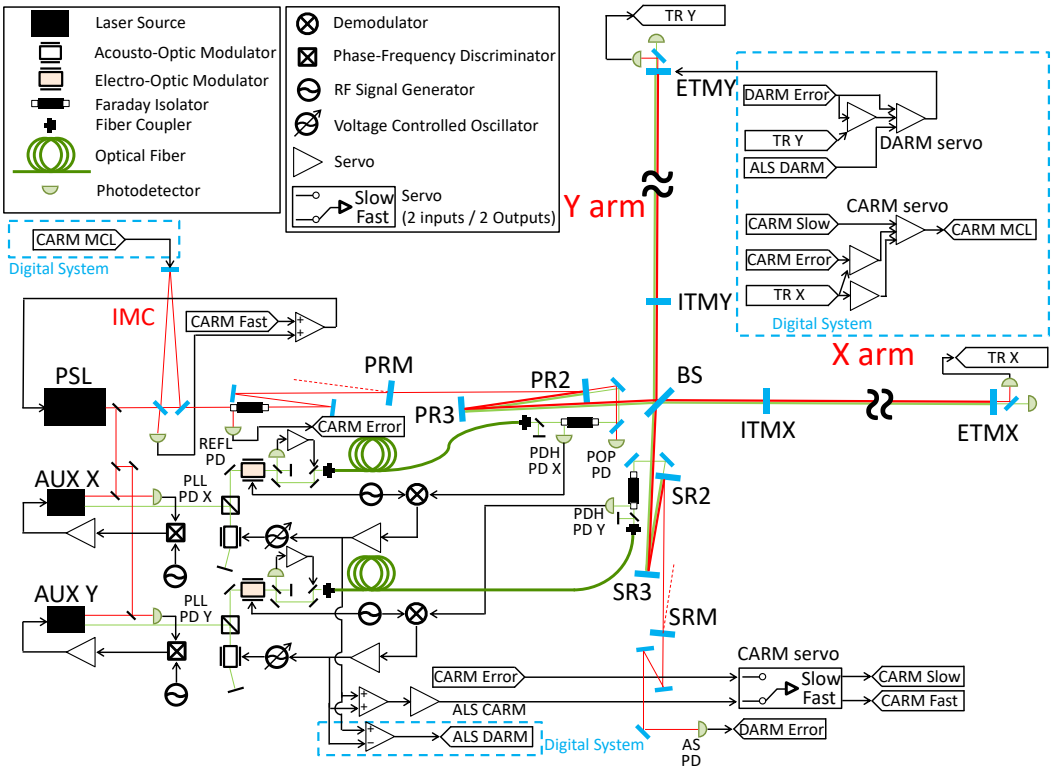

Figure 7.12: Interferometer configuration for the demonstration of lock acquisition with the KAGRA ALS. The control diagram is focused on the CARM and DARM control. The PRM and SRM were misaligned.

7.4 Demonstration

Using the ALS system that has been implemented in the main interferometer, we have achieved lock acquisition of the FPMI of KAGRA. Figure 7.12 shows the interferometer configuration when the demonstration of the lock acquisition

scheme with the KAGRA ALS was performed. We chose the FPMI configuration instead of the DRFPMI because the control of the DRMI (the central interferometer of the DRFPMI) was unstable due to the failure of polarization property of the ITMs [160, 161]; the birefringence of the ITMs due to inhomogeneity of the sapphire crystals was too large for the control of the DRMI to be stably held. Thus we simplified the central interferometer to the short Michelson interferometer for the demonstration purpose. The DARM control was closed by actuating only ETMY in order to simplify the control topology; actuating both ETMs might introduce instabilities in the control loop due to undesirable competition of the motion of two ETMs. The fiber noise cancellation loops were engaged to improve the noise performance of the ALS system.

In order to demonstrate, with the FPMI configuration, that full interferometer[‡8] lock is achievable by utilizing the present ALS system, we performed lock acquisition of the FPMI using the following two schemes. In the first scheme, the CARM and DARM controls were directly handed over from the ALS signals to the main laser PDH signals. In the second schemes, the CARM (or the PSL frequency) is controlled using the optical power of the transmitted beam of the arm cavities as the error signal in the intermediate steps as Advanced LIGO does. The purposes of the demonstration of each scheme are the following.

The demonstration of first scheme shows that the the ALS CARM and ALS DARM controls satisfied the requirement that the fluctuations of the main laser frequency with respect to the resonant frequency of the arm cavities are suppressed within the linewidth of the arms. It is worth mentioning that the linewidths of the CARM and DARM of our demonstration setup are, to our best knowledge, the narrowest ever in the arm cavities whose lock acquisition is achieved purely with ALS.

The achievement of lock with the second scheme demonstrates the process of the CARM hand-over from the ALS signal to the transmission signal. As the final step of the CARM lock process of the DRFPMI, which is the hand-over from the transmission signal to the PDH signal at REFL port, has been established in Advanced LIGO [22], the demonstration of the second scheme shows that the ALS system is ready for locking the DRFPMI. Once the hand-over from the ALS signal to the transmission signal is demonstrated, the successive locking procedure of the DRFPMI in Advanced LIGO, which is irrelevant to ALS, should be applicable also to KAGRA. For DARM locking, since the SR cavity widens the linewidth of DARM in contrast, lock acquisition of DARM should be achievable also in the DRFPMI.

[‡8] DRFPMI.

7.4.1 Interferometer setup

The interferometer setup when the demonstrations were performed can be summarized as follows. The main laser power after the IMC was approximately 4 W. The power after the laser transmitted through the PRM was approximately 0.4 W since the transmission of the PRM was approximately 10 %. The power of each green laser injected to the arm was about 10 mW. The temperature of ETMX, ITMX, ETMY, and ITMY was 179 K, 174 K, 259 K, and 293 K, since each cryostats housing the test mass was in preparation status for the cool-down of the mirror. The Mach–Zehnder interferometers for the modulation system of the PSL was not employed at that time since they could not satisfy the noise requirement. Thus non-resonant amplitude modulation sidebands of f_3 could not be used, and the third harmonic demodulation technique was used instead. Since the OMC was not ready, the lock acquisition sequences were demonstrated up to a stage where DARM was sensed by RF readout with the PDH signal at AS port instead of DC readout with the OMC transmission signal. However, the transition from RF readout to DC readout is an independent process that has been established, thus it is of no relevance with demonstrating the performance of the ALS system in the lock acquisition processes.

7.4.2 The first scheme: direct transition from the ALS system

Figure 7.13 shows how the optical power of the main infrared or auxiliary green lasers at various detection ports evolved in time along with the steps taken throughout the lock acquisition process. Here, each step of the first lock acquisition scheme is explained.

(I) The resonances of both arm cavities only for the green auxiliary lasers were achieved by feeding back the PDH error signals to the VCOs.

(II) The ALS CARM control was engaged with the full frequency bandwidth using both slow and fast outputs of the CARM servo. The crossover frequency of the slow and fast loops was set to around 80 Hz. The overall control bandwidth was about 2 kHz at this point.

(III) In this period, the ALS DARM control was gradually engaged by feeding back the ALS DARM signal to the longitudinal motion of ETMY. The feedback force was applied to the test mass stage in the high frequency region and the marionette stage in the low frequency region. The cross

over frequency of the two actuation loops was set to around 1 Hz. The overall control bandwidth was about 30 Hz at this stage. From this step, the ALS system controlled the difference between the main laser frequency and the resonant frequency of each arm so that the main laser no longer stochastically resonated in the arms.

(IV) In this period, the resonance points of both arms were searched by sweeping the LO frequencies of the PLLs. At the end of this period, the two arms were held at the resonance points of the main laser.

(V) The control loop of the DoF of the central interferometer, MICH in this case, was engaged by using the third harmonic demodulation signal of f_1 at REFL port in Q-phase (REFL51Q) as the error signal. The MICH control signal was fed back to the BS.

(VI) In this period, the DARM control was handed over from the ALS system to the main laser PDH signal. The error signal used here was the PDH signal of f_1 at AS port in Q-phase normalized by the transmitted power of the arm (AS17Q/TRY), which have broader linear range than the ordinary PDH signal by a factor of a few. The use of the normalized one helped to significantly reduce the rate of hand-over failures due to the associated transients. After the hand-over, the control bandwidth was successively increased by a factor of 1.5 and two stages of a low frequency boost filter were enabled.

(VII) The CARM control was handed over from the ALS system to the main laser PDH signal of f_2 at REFPl port in I-phase (REFL45I), by enabling the first input and disabling the second input of the CARM servo circuit. The overall control bandwidth was about 5 kHz from this point.

(VIII) The error signal of the DARM control was switched from AS17Q/TRY to the ordinary PDH signal (AS17Q).

(IX) The error signal of the MICH control was switched from REFL51Q to the 1f signal at REFL port (REFL17Q), to finish the lock acquisition sequence.

The whole process listed above was automated. We performed four times the demonstration in the procedure described above, and succeeded every time.

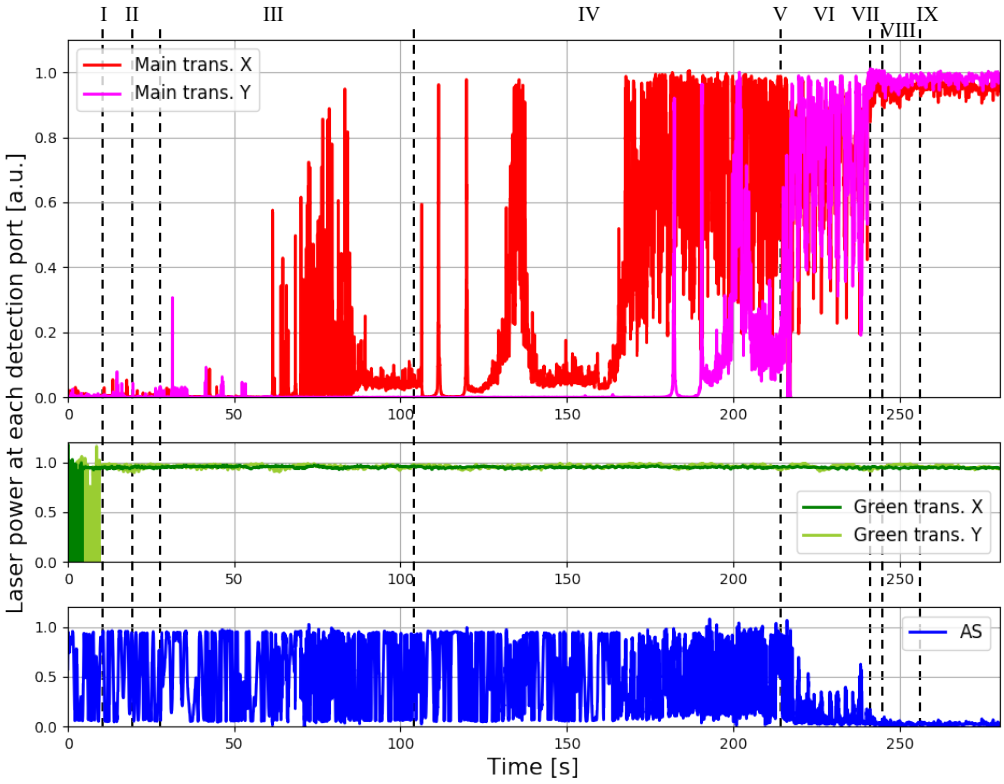

Figure 7.13: Time series of the optical power at various detection ports as the steps of the first lock acquisition scheme proceed. The top panel shows the main laser power at the transmission of the arm cavities. The middle shows the green laser power at the transmission of the arms. The bottom shows the main laser power at AS port. The Roman numerals from I to IX denote the steps of the lock acquisition sequence.

7.4.3 The second scheme: transmission lock

Figure 7.14 shows how the optical power of the main infrared or auxiliary green lasers at various detection ports evolved in time along with the steps taken throughout the lock acquisition process. Here, each step of the first lock acquisition scheme is explained.

(I) The resonance of the X arm cavity only for the green auxiliary laser was achieved by feeding the PDH error signal back to the corresponding VCO.

(II) The ALS CARM (frequency) control was engaged using only the IMC length as the actuator of the PSL frequency via the digital control system. The control bandwidth was about 100 Hz at this point.

(III) In this period, the main laser resonance of the X arm was searched by sweeping the LO frequency of the X arm PLL.

(IV) The PSL frequency control was handed over from the ALS system to the signals from the transmission power of the X arm, which is called TR CARM. This signal is the square root of the transmission power, which is realized by the real-time controllers.

(V) The resonance of the Y arm cavity only for the green auxiliary laser was similarly achieved.

(VI) In this period, the ALS DARM control was gradually engaged in the same way as described in the previous section. In addition, the MICH control was engaged by using REFL51Q as the error signal at the end of this period.

(VII) In this period, the main laser resonance of the Y arm was searched by sweeping the LO frequency of the Y arm PLL.

(VIII) In this period, the DARM control was handed over from the ALS system to the normalized PDH signal at AS port as described in the previous section.

(IX) In this period, the error signal of the CARM control was gradually switched from TR CARM to the normalized PDH signal at REFL port, which is named as REFL17I/(TRX+TRY). In this process, the locking point of the X arm gradually shifted from the middle to the top of the resonance as the error signals were changed.

(X) In this period, the CARM error signal was switched to the ordinary PDH signal (REFL45I) and successively the control bandwidth of CARM was increased to about 5 kHz by engaging the fast analogue feedback path to form the dual-loop CARM control.

(XI) The error signal of the DARM control was switched from AS17Q/TRY to the ordinary PDH signal (AS17Q).

(XII) The error signal of the MICH control was switched from REFL51Q to the 1f signal at REFL port (REFL17Q), to finish the lock acquisition sequence.

The whole process listed above was automated. We performed three times the demonstration in the procedure described above, and succeeded every time.

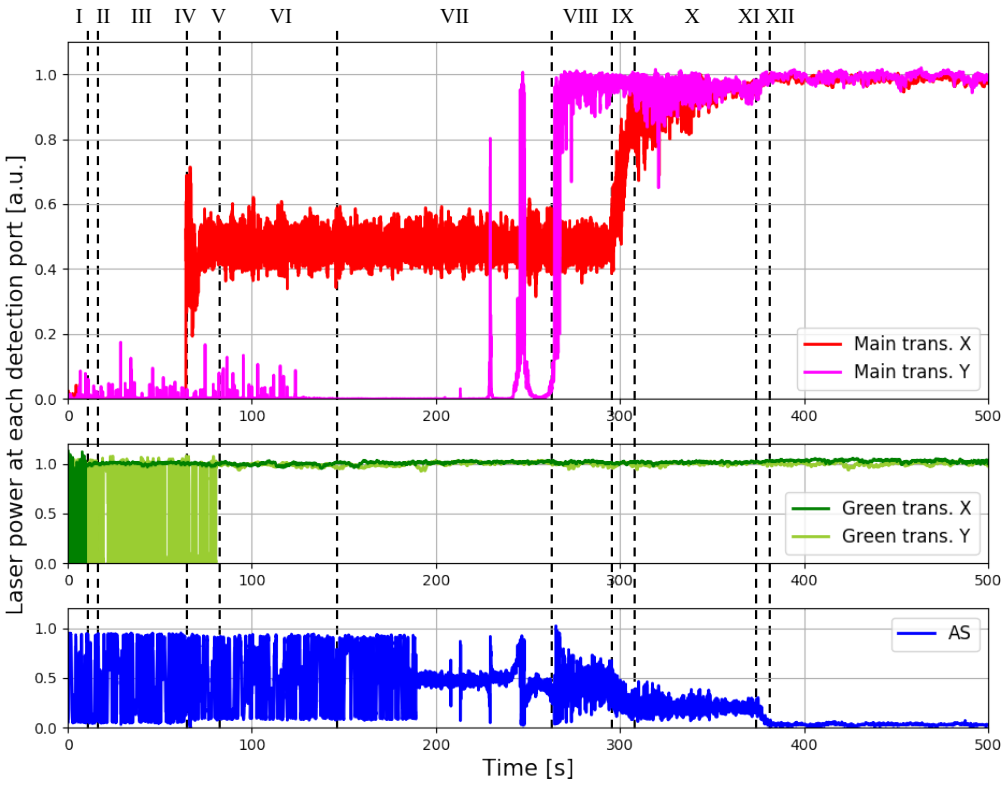

Figure 7.14: Time series of the optical power at various detection ports as the steps of the first lock acquisition scheme proceed. The top panel shows the main laser power at the transmission of the arm cavities. The middle shows the green laser power at the transmission of the arms. The bottom shows the main laser power at AS port. The Roman numerals from I to XII denote the steps of the lock acquisition sequence.

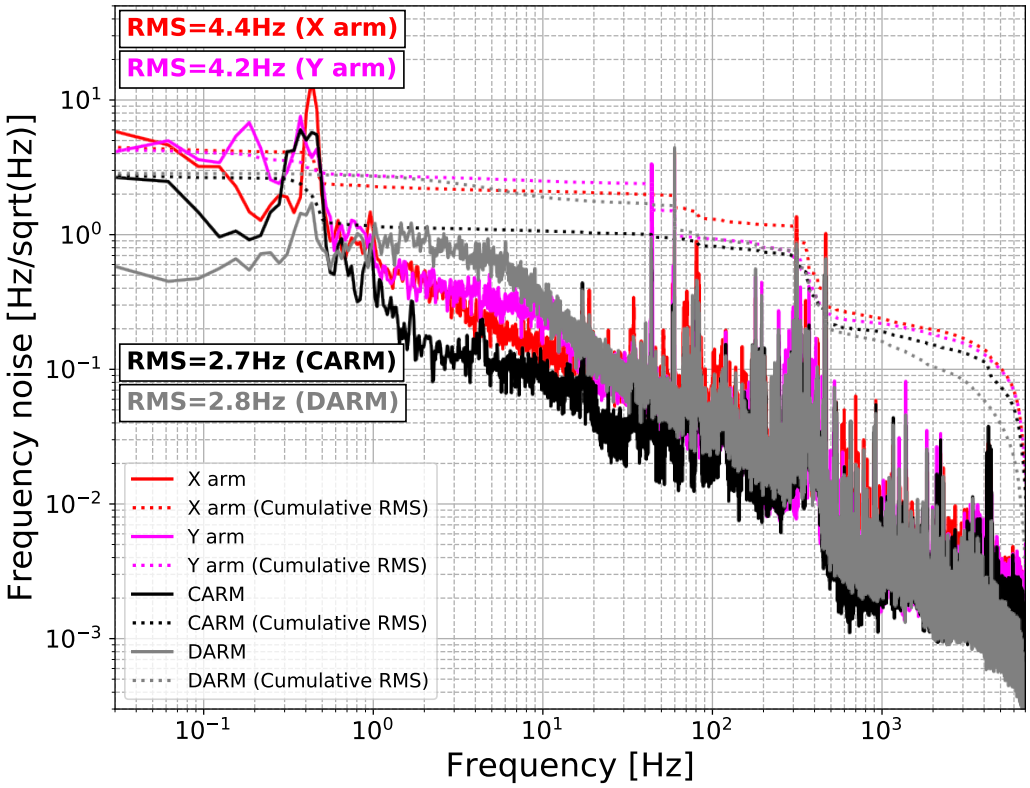

Figure 7.15: ASDs of sensing noise of the ALS system in the basis of the X and Y arms, and that of ALS CARM and DARM. The red solid trace shows the ASD of $\Delta f_{\rm res}(f;\kappa_{\rm ARM})$ of the X arm. The red dotted line shows its cumulative RMS. The magenta solid trace shows the ASD of the Y arm. The magenta dotted line shows its cumulative RMS. The black solid trace shows the ASD of ALS CARM. The black dotted line shows its cumulative RMS. The gray solid trace shows the ASD of ALS DARM. The gray dotted line shows its cumulative RMS.

7.5 Characterization

In order to quantitatively characterize the performance of the KAGRA ALS system, we have conducted the following measurements.

7.5.1 Sensing noise

The most important characteristic of ALS systems is the residual fluctuations of the arm DoFs, $\Delta f_{\mathrm{res}}(f;\kappa_{\mathrm{ARM}})$. If the control bandwidths of CARM and DARM are sufficiently large, which is usually the case, sensing noise of the ALS system limits $\Delta f_{\mathrm{res}}(f;\kappa_{\mathrm{ARM}})$. Therefore, we evaluated the sensing noise level of the ALS system in two sets of bases, (X arm, Y arm) and (CARM, DARM). The evaluation method was the following. For the evaluation on the basis of (X arm, Y arm), the PSL frequency was locked to the resonance of one arm cavity of interest by using REFL45I as the error signal while the mirrors of the other arm cavity was misaligned not to disturb the interested arm. At the same time, the frequency of the auxiliary green laser of the interested arm was locked to the resonance of the same arm without feeding any signals back to the main laser or test masses from the ALS system. In this configuration, sensing noise of the ALS system of the interested arm can be inferred by measuring the control signal of the PDH loop under the assumption that residual frequency fluctuations of the main laser with respect to the arm is small enough to be ignored for the noise estimation. For the evaluation on the basis of (CARM, DARM), the FPMI was locked only with the main laser signals as described in the previous section while the frequency of each auxiliary green laser was locked to the resonance of the corresponding arm. In the similar way, sensing noise of the ALS system of CARM and DARM can be obtained by measuring the ALS CARM and ALS DARM error signals, respectively. The data for the bases of X and Y arms and ALS CARM were acquired by digital controller after they were amplified by an analogue circuit. The measured signals were calibrated into frequency based on the efficiencies of the VCOs (Appendix F). From the measurement results of the efficiencies, calibration error of $\sim 3\,\%$ can be expected in the estimation.

We adopted this evaluation method to suppress the nonlinear effect in the main laser PDH signals, instead of a straightforward method where one measures the ASDs of the PDH signals while the interested DoFs are controlled by the ALS system so that the PDH signals are kept around the zero points, which are the center of their linear range. This is because the straightforward method may suffer from the nonlinear effect in the PDH signals if they are not confined sufficiently close to the zero points.

Figure 7.15 shows the ASDs of sensing noise of the ALS system measured in the two different bases, calibrated to $\Delta f_{\mathrm{res}}(f;\kappa_{\mathrm{ARM}})$. The sensing noise levels of the X arm and Y arm, and CARM and DARM are shown along with the corresponding cumulative RMS curves. They show that the RMSs of sensing

noise of the X and Y arms were 4.4 Hz and 4.2 Hz, respectively. Those of ALS CARM and ALS DARM were 2.7 Hz and 2.8 Hz, respectively. All of these RMS values were smaller than the linewidth of the arm cavities of KAGRA, 33 Hz, which supported the ALS system satisfied the noise requirements of KAGRA.

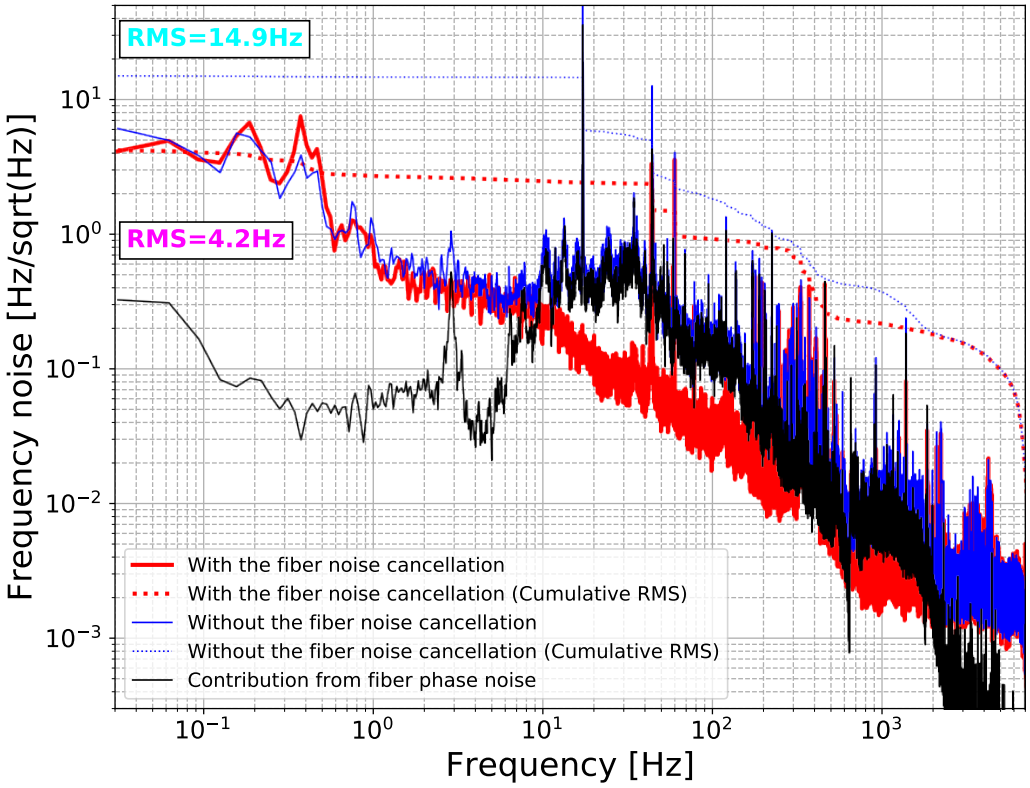

Figure 7.16: ASDs of sensing noise of the ALS system for the Y arm with and without the fiber noise cancellation loop engaged. The red solid trace shows the ASD of $\Delta f_{\mathrm{res}}(f;\kappa_{\mathrm{ARM}})$ with the fiber noise cancellation loop engaged. The red dotted line shows its cumulative RMS. The blue solid trace shows the ASD with the fiber noise cancellation loop disabled. The blue dotted line shows its cumulative RMS. The black solid line shows the estimated contribution from fiber phase noise to the blue trace. The sharp peak at 17 Hz came from vibration of the clean booths caused by air filter fan units, which then shook the fibers.

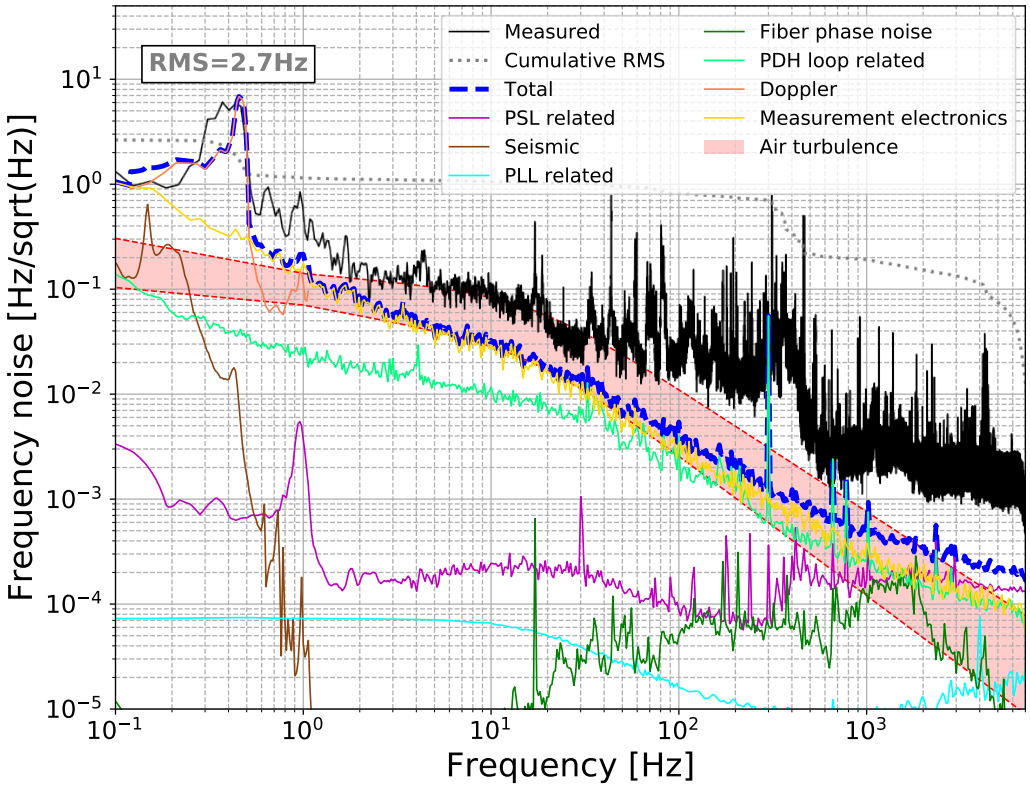

Figure 7.17: Noise budget plot of sensing noise of the ALS system for ALS CARM. The black trace is the measured ASD of sensing noise of ALS CARM $\Delta f_{\mathrm{res}}(f;\kappa_{\mathrm{ARM}})$, which is also plotted in Figure 7.15. The gray dotted trace is its cumulative RMS. The blue dashed line shows total noise, which is quadrature sum of the contributions of all the evaluated noise sources described in the following. The magenta trace shows sum of the contributions of noise sources related to the PSL and its frequency stabilization. The brown one shows the estimated residual contribution of arm length fluctuations due to seismic motion. The cyan one is the contribution of the noise sources associated with the PLLs of the auxiliary lasers including the free-run frequency noise of the lasers. The green one shows the contribution of fiber phase noise including electrical noise in the cancellation loops. The light green one is the contribution of noise from electronics involved in the PDH loops. The orange one is the contribution of the Doppler shifts caused by the BS, PR2, PR3, and SR3. The yellow one shows the noise level of the electronics involved in the sensing noise measurement. The above contributions are included in total noise. The red shaded belt shows the possible effect of air turbulence around the POP and POS table or the PSL table.

Figure 7.16 shows the ASDs of the sensing noise spectra of the Y arm ALS with and without the fiber noise cancellation loops engaged as an example. It also shows the estimated contributions from fiber phase noise to the sensing noise spectrum with the cancellation loop disabled. According to these plots, the fiber noise cancellation helped to improve the noise level in a broad frequency region of $\sim 10 - 2000\,\mathrm{Hz}$. The suppression of the noise level recorded its maximum of ~ 500 at 17 Hz and, as a result, the RMS was improved by a factor of ~ 3.5. It can be also said that the estimated contribution from fiber phase noise explains well the excess in the ASD without the fiber noise cancellation. The spectrum of fiber phase noise were measured in a separate preliminary measurement by closing the fiber noise cancellation loop. The situation was similar in the X arm.

In order to understand the sources of measured sensing noise of the ALS system, we performed a number of supplementary measurements. Figure 7.17 shows the contributions of the various noise sources on sensing noise in the ALS CARM signal, evaluated in such measurements. The black solid trace shows measured sensing noise of ALS CARM, while the blue dashed line is quadrature sum of the contributions of all the noise sources considered so far. In the frequency region above about 0.5 Hz, there is discrepancy between the measured noise level and the total noise level, which is discussed in Section 7.6. It is worth noting that this discrepancy is not a large issue because the RMS of sensing noise satisfied the requirement and noise in this frequency region did not limit the RMS. In contrast, below about 0.5 Hz, the Doppler shift caused by the BS, PR2, PR3, and SR3 can explain the measured noise level.

Doppler noise

When a laser beam gets reflected by a moving mirror, a Doppler shift is introduced to the laser frequency, which can be approximated in the Fourier domain as follows.

$$\Delta f_{\mathrm{Doppler}}(f) = \frac{2\pi}{\lambda} 2v(f) \tag{7.4}$$

$$= \frac{i4\pi f}{\lambda} x(f), \tag{7.5}$$

where $\Delta f_{\mathrm{Doppler}}(f)$ is the amount of the Doppler shift, λ is the wavelength of the laser, and $v(f)$ and $x(f)$ are the velocity and displacement of the mirror, respectively. If a mirror reflects only the main laser or the auxiliary laser, the Doppler shift caused by the mirror motion becomes a source of sensing noise of the ALS system. In contrast, if a mirror reflects both the main laser and the

auxiliary laser such as PR3 in the X arm ALS, the motion of the mirror is not a noise source; according to the equation, the auxiliary laser gets a Doppler shift exactly twice larger than that of the main laser.

As an example, we measured the transfer function from the displacement of PR2 measured by its local sensors [138] to sensing noise of the Y arm ALS, as shown in Figure 7.18. It shows the agreement between the measured transfer function and the theoretical line. We also performed another measurement where the Doppler couplings from the displacement of PR3 to sensing noise of the X arm ALS and Y arm ALS were measured for comparison. Measurement was done at a single frequency of 4.1 Hz, and it was observed that the coupling to the X arm ALS was suppressed by 20.3 dB than that to the Y arm ALS, which supports the expectation that the Doppler shift is not a noise source for a mirror that reflects both the main and auxiliary lasers.

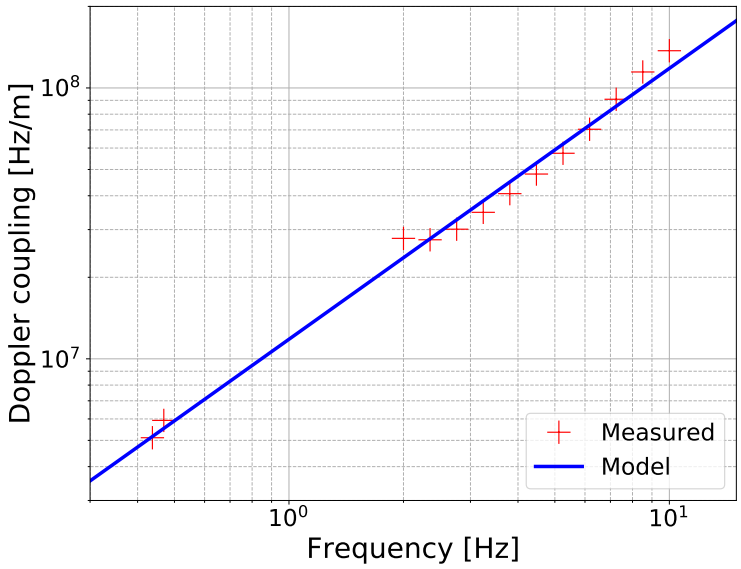

Figure 7.18: Doppler coupling of the longitudinal motion of PR2 to sensing noise of the Y arm ALS. The red plus marks show the measured transfer function from longitudinal motion of PR2 to sensing noise of the Y arm ALS. The data points above 1 Hz were obtained by an active measurement where the longitudinal motion of PR2 was excited by sinusoidal signals, while the other data points were obtained in a passive measurement where there were no intentional excitations. The blue line shows the theoretical Doppler frequency shift imposed on the main laser (Equation 7.5).

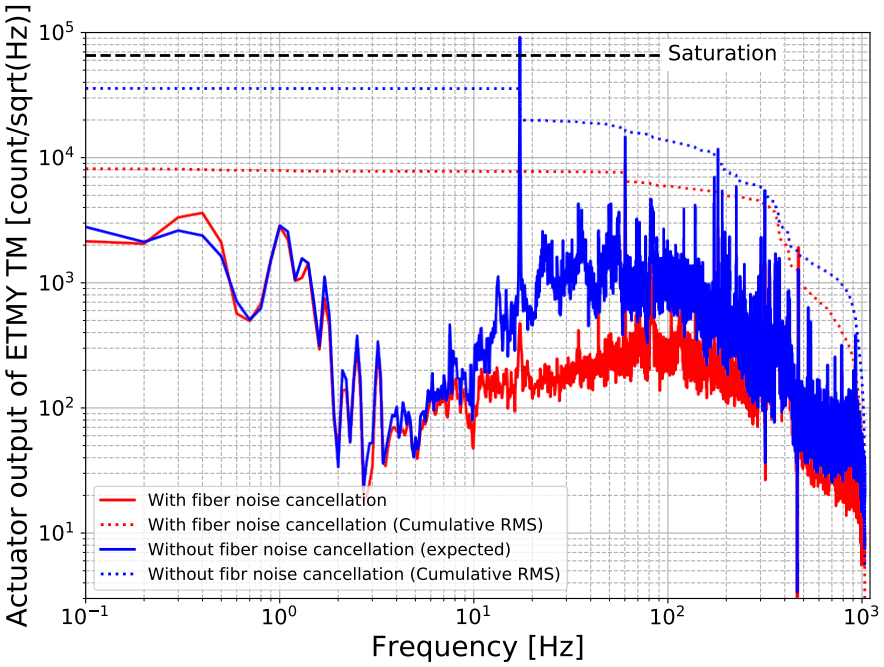

Figure 7.19: ASD of the control signal of ALS DARM applied to the actuators at TM stage of ETMY. The red solid trace shows the measured ASD of the output of the ETMY TM actuators from the digital system. The red dotted line is its cumulative RMS. The blue solid trace is the expected ASD if the fiber cancellation loops were disabled. The blue dotted line is its cumulative RMS. The black dashed line shows the level at which the actuators saturate.

Assuming the coupling mechanism described above, the contributions of the longitudinal motions of the BS, PR2, PR3 and SR3 were evaluated by utilizing their local sensors at the mirror stages. The evaluated contributions are shown in the noise budget plot, Figure 7.17.

This coupling mechanism was first mentioned and discussed in the literature [22, 162]. They treated the coupling mechanism as *nonlinear*,[‡9] but it should be noted here that this mechanism is *linear* as long as the associated sensing is linear, which is the case either for KAGRA or Advanced LIGO.

[‡9]The fact that they called this noise *fringe wrapping* also indicates that they considered this mechanism as nonlinear.

7.5.2 Actuator saturation

Figure 7.19 shows the ASD of the control signal of ALS DARM applied to the actuators at the TM stage of ETMY in the step (III) of the first lock acquisition scheme. It can be seen that the ASD was limited by sensing noise of the ALS system above about 4 Hz and its RMS was also limited by it. The RMS of the control signal was smaller than the full range of the actuators by a factor of ~ 8, which was small enough to avoid saturation of the actuators during the lock acquisition process. It also shows the estimated ASD of the control signal if the fiber noise cancellation loops are disabled. The estimation was done by comparing the sensing noise levels of ALS DARM with and without the cancellation loops. It can be seen that the RMS would be close to the saturation level without the cancellation loops. This comparison indicates that the cancellation helped to have the DARM control bandwidth of about 30 Hz without saturating the actuators of the test mass.

7.6 Discussion

The demonstration and characterization of the ALS system were performed in the FPMI configuration instead of the DRFPMI configuration, as described in the previous section. Here let us estimate the noise performance in the DRFPMI of KAGRA in near future, which makes the CARM linewidth even narrower due to the power recycling while that of DARM is widened. Thus the following discussion is focused on CARM.

Figure 7.20 shows the measured ASD of sensing noise of the ALS system calibrated to $\Delta f_{\rm res}(f;\kappa_{\rm CARM})$ along with the designed ASD. The RMS expected from the measured ASD is 2.2 Hz, which is larger than the full linewidth of CARM, 1.6 Hz. Therefore, improvement in the noise performance is required to satisfy the ambitious target so that the direct hand-over of the CARM control is realized also in the DRFPMI.

Here, let us discuss the discrepancy between the designed and measured noise performance, with a focus on the ambitious noise target. After the expected noise sources are overviewed (Section 7.6.1), then unexpected noise sources, which are Doppler noise (Section 7.6.2) and air turbulence (Section 7.6.3), are discussed.

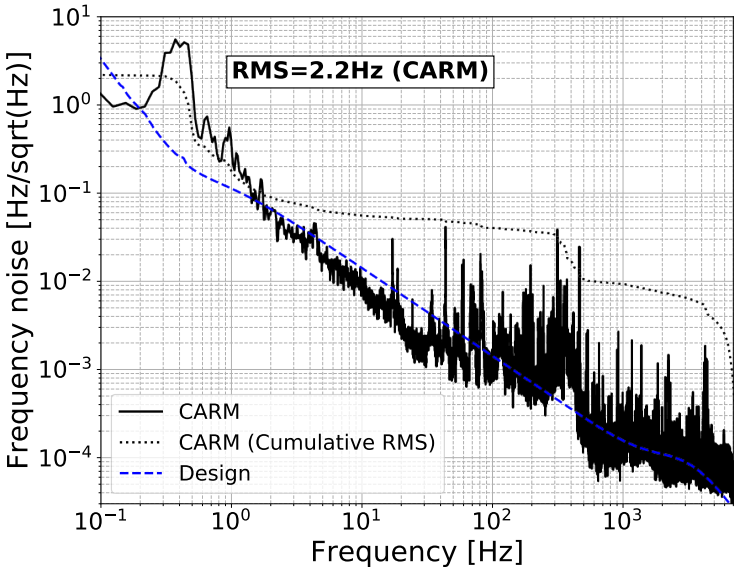

Figure 7.20: Expected ASD of sensing noise of the ALS system calibrated to $\Delta f_{\mathrm{res}}(f;\kappa_{\mathrm{CARM}})$ in the DRFPMI, along with the designed noise of the system. The black solid trace shows the measured ASD of the sensing noise. The black dotted line is its cumulative RMS. The blue dashed line is the simulated noise level in the design study, which is also shown in Figure 7.2.

7.6.1 Expected noise sources

Let us first review the noise sources that was expected in advance. Table 7.4 summarizes the comparison between the noise levels of each component expected at the time of the design study and those evaluated after the implementation of the components.

For phase noise from the optical fibers, it turned out that the noise level had been underestimated. However, the contribution from fiber phase noise was mitigated by engaging the fiber noise cancellation loops. The fiber phase noise is discussed below in more detail. For VCO noise, the achieved noise level was better than the conservative expectation. For arm length fluctuations, though we could not measure the fluctuations separately from the frequency fluctuations around 1 Hz, the upper bound shown in the table is sufficiently low for CARM; the noise design expects that the contribution from arm length fluctuations is more than 1000 times smaller than the total noise level at 1 Hz. For the frequency fluctuations of the auxiliary lasers, though the achieved level was slightly higher

Table 7.4: Comparison of the expected and achieved noise levels. The ASDs at 1 Hz are shown.

Noise source	Expected	Achieved
Optical fiber	$0.01\,\mathrm{Hz}/\sqrt{\mathrm{Hz}}$	$0.05\,\mathrm{Hz}/\sqrt{\mathrm{Hz}}$ (Figure 7.16)
VCO	$0.5\,\mathrm{Hz}/\sqrt{\mathrm{Hz}}$	$0.1\,\mathrm{Hz}/\sqrt{\mathrm{Hz}}$ (Appendix F)
Arm length fluctuations	$3\times10^{-9}\,\mathrm{m}/\sqrt{\mathrm{Hz}}$	$\leq 1\times10^{-7}\,\mathrm{m}/\sqrt{\mathrm{Hz}}$ [163]
Free-run frequency noise of the auxiliary laser	$1\times10^{5}\,\mathrm{Hz}/\sqrt{\mathrm{Hz}}$	$3\times10^{5}\,\mathrm{Hz}/\sqrt{\mathrm{Hz}}$ [164]
PSL frequency noise	$1\times10^{4}\,\mathrm{Hz}/\sqrt{\mathrm{Hz}}$	$1\times10^{4}\,\mathrm{Hz}/\sqrt{\mathrm{Hz}}$ [163]

than the expected level only around 1 Hz, it did not matter because their effect should be sufficiently suppressed by the PLLs as shown in Figure 7.17. For frequency noise of the main laser (PSL), the level was almost same as expected.

To summarize the above arguments, we can say that the expected noise sources did not degrade the designed noise performance. The fiber phase noise would have degraded the performance without the cancellation, but the fiber noise cancellation loops mitigated the contribution from this noise source.

Fiber phase noise

In the design study, it was expected that the contribution of fiber phase noise limited the overall noise level only below 0.4 Hz without the cancellation technique (Figure 7.2). However, it turned out that fiber phase noise limited the overall measured noise level in $\sim 10 - 2000$ Hz without the cancellation (Figure 7.16). This indicates that the the magnitude of fiber phase noise was significantly underestimated in the design study. As is mentioned in 7.2.2 (and Appendix F), the level of fiber phase noise in the KAGRA site was estimated based on a measurement of phase noise of an 5-meter long optical fiber that was gently placed on an optical table. Thus this discrepancy between the estimation and measurement of the fiber noise contribution is probably due to the different environments between the fiber testing setup and the KAGRA site. It indicates that the protection of the laid fibers from sounds or vibrations (Section 7.3.2) was not enough in terms of the phase noise.

Although the magnitude of fiber phase noise was significantly larger than the expectation, it turned out that this noise was not a critical issue; the fiber noise cancellation loops successfully mitigated the contributions of this noise. In fact, the cancellation loops were effective in terms of the residual RMS of the

ALS control of the arm DoFs and the range of the actuators of the test mass, as discussed in the previous section. With the cancellation loops engaged, the number of the optical sensing involved in the whole ALS system is six instead of four (Table 7.1). Thus it should be admitted that the number of the optical sensors is no longer an advantage of our configuration to that of Advanced LIGO.

We employed mirrors with piezoelectric transducers as actuators of the fiber noise cancellation loops. There was a minor issue that actuation range of the transducers limited the lock stretch of these loops (typically $30 - 60$ minutes). The drift of the fiber length caused the actuator saturation. In order to solve this issue, a possible approach is to use the combination of AOMs and VCOs as the actuators instead.[‡10] Since it can actuate the frequency of the laser as opposed to the phase, the actuation range at DC in terms of the optical phase is effectively infinite. The comparison and characterization of various schemes of the fiber noise cancellation, including the possible implementation to KAGRA ALS in the scope, are on-going as an independent research project [165].

7.6.2 Doppler noise

It turned out that Doppler noise limits the overall performance especially in the low frequency region. As can be seen from Figure 7.20, the measured noise level was significantly higher than the designed one in $\sim 0.2 - 1\,\mathrm{Hz}$, where the RMS was limited. Since the limiting noise source in this frequency region was Doppler noise caused by the suspended mirrors, it is likely that, by improving the Doppler noise coupling by a factor of a few, the ambitious noise target can be satisfied.

In order to deal with the Doppler noise coupling, it is necessary to reduce the motion of the mirrors or to sense the motion for online noise subtraction. Since the reduction of the motion of the mirrors is usually done by active controls, it is important to have good sensors for the BS, PR2, PR3, and SR3 in either case. It would be also useful to have such sensors for the steering mirrors behind PR2 or SR2 placed on the suspended breadboards. If we prepare and utilize sensors for them with the sensitivity level of $\sim 3 \times 10^{-7}\,\mathrm{m}/\sqrt{\mathrm{Hz}}$ around 0.5 Hz, improvement in the Doppler noise coupling can be expected by a factor of five, which should be sufficient.

[‡10] In this case, the readout scheme of the interferometers for the cancellation needs to be changed of course.

7.6.3 Air turbulence

A candidate of the noise source that could explain the discrepancy in the characterization of sensing noise of the ALS system (Figure 7.17) is turbulence of air. It has been reported that air turbulence introduces phase fluctuations in laser fields that propagate in air [166,167]. Since the auxiliary laser and the main laser take different paths in air, the air turbulence independently introduces phase fluctuations to the two laser beams, which leads to a noise source of the ALS system. Let us estimate its effect on the noise performance of the ALS in the following.

According to the Kolmogorov's theory, the PSD of phase fluctuations caused by air turbulence $S_\phi(f)$ scales as $S_\phi(f) \propto LV^{5/3}f^{-8/3}$ [166,167], while an experiment reported that $S_\phi(f) \propto f^{-7/3}$ [167]. Here, L is the optical path length and V is a constant wind speed. Therefore, the level of phase fluctuations in our case can be estimated by knowing L and V. L was about 10 m for our case. However, it is not obvious how we can estimate typical V in the beam paths.

It has been also known that angular jitter of the beam is caused by the air turbulence and its PSD $S_\alpha(f)$ is related to $S_\phi(f)$ by

$$S_\alpha(f) = (\lambda/V)^2 S_\phi(f) \tag{7.6}$$

in low frequency region, where λ is the wavelength of the laser beam [167,168]. The PSD of angular jitter has a cut-off frequency of approximately $0.3V/D$, where D is the diameter of the beam [168]. Therefore, the effective wind speed V can be estimated from the spectrum of angular jitter of the beam propagating in a clean booth in the KAGRA site. In the characterization of local sensors of mirrors called optical levers, the PSD of such angular jitter had been measured [169]. In this characterization measurement, the cut-off frequency was about 10 Hz with $D \sim 1$ mm, which leads to $V \sim 3 \times 10^{-2}$ mm.[‡11] Let us adopt this number for V. The magnitude of the PSD of the angular jitter was reported to be

$$\sqrt{S_\alpha(f = 1\,\mathrm{Hz})} \sim 0.4\,\mu\mathrm{rad}/\sqrt{\mathrm{Hz}} \tag{7.7}$$

with $L \sim 0.1$ m. Let us also use this number to estimate the level of phase fluctuations through Equation (7.6). By combining Equations (7.6) and (7.7)

[‡11] In the clean booth that housed POP and POS table, filter fan units were operating on the roof. The total volume of air per unit time by the filter fan units were 20 m^3/s and the area of the side of the clean booth, where the air escaped to outside, was about 240 m^2 [170]. The average wind speed can also be inferred from these numbers as 8×10^{-2} m/s, which is comparable to the number we adopt. It is reasonable that this number is larger than 3×10^{-2} m/s, because the wind probably leaks outside mainly from the area far and higher from the tables.

and $S_\phi \propto L$, S_ϕ in the ALS system can be inferred as

$$\sqrt{S_{\Delta f}(f = 1\,\mathrm{Hz})} = \sqrt{f^2 S_\phi(f = 1\,\mathrm{Hz})} \sim 1 \times 10^{-1}\,\mathrm{Hz}/\sqrt{\mathrm{Hz}}, \tag{7.8}$$

where $S_{\Delta f}$ is the corresponding PSD in terms of frequency fluctuations.

In Figure 7.17, the red shaded belt shows the possible effect of the air turbulence, which is estimated from the above discussion with allowance for estimation error of a factor of two. The area between two lines are filled. The upper line was calculated based on

$$\sqrt{S_{\Delta f}(f)} = 1 \times 10^{-1} \times \sqrt{2 \cdot f^2 \max\left[\left(\frac{f}{1\,\mathrm{Hz}}\right)^{-8/3}, \left(\frac{f}{1\,\mathrm{Hz}}\right)^{-7/3}\right]}\,\mathrm{Hz}/\sqrt{\mathrm{Hz}}, \tag{7.9}$$

while the lower one was on

$$\sqrt{S_{\Delta f}(f)} = 1 \times 10^{-1} \times \sqrt{\frac{1}{2} f^2 \min\left[\left(\frac{f}{1\,\mathrm{Hz}}\right)^{-8/3}, \left(\frac{f}{1\,\mathrm{Hz}}\right)^{-7/3}\right]}\,\mathrm{Hz}/\sqrt{\mathrm{Hz}}. \tag{7.10}$$

Here, the error of an overall factor of two is allowed, and both of the two different power laws of $f^{-8/3}$ and $f^{-7/3}$ in the literature are considered. From this plot, it can be said that the contribution from the air turbulence can account for the discrepancy in the frequency range of $\sim 2 - 100\,\mathrm{Hz}$.

Chapter 8
ALS IN THE THIRD GENERATION

In this chapter, after setting a possible configuration of an ALS system for the 3G detectors, the noise performance of the ALS system is numerically simulated based on the knowledges we have gained through the development and characterization of the KAGRA ALS. The results are discussed based on the requirements on the system. The feasibility of new techniques that will be essential in lock acquisition are also discussed. The works covered by the present chapter were done by the author of the dissertation.

8.1 Challenges

First, let us list expected challenges in lock acquisition of the 3G interferometers. Unless another technique is developed, ALS will be used also in the 3G detectors. The 3G detectors will employ the similar interferometer configuration to that of the 2G detectors, but the arm length will be about $3 - 10$ times longer. In addition, the wavelength of the main laser might be changed from 1064 nm to 1550 nm or even longer, for the use of silicon as a test mass. These differences will cause the following challenges in ALS systems in the 3G detectors.

- The linewidth of CARM will be much narrower. While the finesse of the single arm cavity depends on the detailed design of the interferometer,[‡1]

[‡1] The detector bandwidth (the linewidth of DARM) is determined by the combination of the finesse of the arm cavity and the reflectivity of the SRM. Thus fixing the detector bandwidth does not fix the arm finesse. It is determined by what the maximum signal recycling gain is and how much optical power in the central interferometer can be allowed considering the heat absorption of the ITM substrates.

Table 8.1: Parameter set of the Cosmic-Explorer-like detector. The parameters in the upper row are written in the reference [8], while those in the lower row are set here for the following discussion.

Arm length (L)	40 km
Test mass material	Silicon
Wavelength (λ_1)	1550 nm
Optical power in the arm ($P_{\rm arm}$)	2 MW
Detector bandwidth ($\kappa_{\rm DARM}$)	400 Hz
Finesse of the arm ($\mathcal{F}_{\rm arm}$)	519
Roundtrip loss of the arm ($T_{\rm loss}$)	100 ppm
Transmissivity of the PRM ($T_{\rm PRM}$)	3.33 %
Transmissivity of the SRM ($T_{\rm SRM}$)	3.50 %
Input laser power ($P_{\rm PRM}$)	400 W

the finesse of CARM is determined by roundtrip optical loss inside the arm cavities, which will not change drastically. Therefore, it is expected that the linewidth of CARM will be narrowed as the arm length gets longer.

- The bandwidth of a control loop related to the arm cavity will be limited by the FSR. As mentioned in Section 4.5.1, the frequency response exactly becomes zero at integer multiples of the FSR. Therefore, it is challenging to close a stable loop with the bandwidth larger than the FSR.

- The second harmonic laser could not be used for the sensing of the arm cavity length if the substrate of the test mass is silicon. The wavelengths of 1550 nm or around 2.0 μm are considered to be promising candidates as the main laser wavelength if silicon is adopted. Because it has been known that silicon is black for the laser with the wavelength of $\sim$ 800 nm or $\sim$ 1000 nm [171], the second harmonic field of the main laser could not propagate through the test mass.

8.2 Configuration

8.2.1 Main interferometer parameters

As a framework of the discussion on the ALS system in the 3G detectors, let us here set parameters of the main interferometer based on the proposal of Cosmic

Explorer [8]. Table 8.1 summarizes the parameters of the main interferometer. Here, realistic values are chosen for the parameters considering technical feasibility because the detailed parameters are not yet fixed except for those necessary for setting the detector sensitivity [8]. However, the values will not be drastically changed unless the optical loss inside the arm is significantly reduced. Let us assume that the property of input optics, such as the configuration of the IMC or the frequency stability of the PSL, is same as those of KAGRA for simplicity. From the above parameter set, the FSR is 3.75 kHz. The single arm linewidth κ_{ARM} and the CARM linewidth κ_{CARM} are calculated: $\kappa_{\mathrm{ARM}} = 3.6\,\mathrm{Hz}$ and $\kappa_{\mathrm{CARM}} = 6.0 \times 10^{-2}\,\mathrm{Hz}$.

8.2.2 ALS configuration

From its parameters, the noise requirement of the single arm ALS of the Cosmic-Explorer-like detector is set by the full linewidth of the arm cavity, $2\kappa_{\mathrm{ARM}} = 7.2\,\mathrm{Hz}$, while the ambitious noise target is by the full linewidth of CARM, $2\kappa_{\mathrm{CARM}} = 0.12\,\mathrm{Hz}$.

As shown in the previous chapter, the performance of the KAGRA-type ALS system was proven in two senses; the FPMI of KAGRA was locked using the ALS system, and the RMS of its sensing noise $\Delta f_{\mathrm{res}}(f;\kappa_{\mathrm{ARM}})$ was as low as about 4 Hz, which is smaller than 7.2 Hz. In addition, the design of the system is scalable to detectors with longer arm length such as the Cosmic-Explorer-like detector. Therefore, it is reasonable to set the configuration of the ALS system of the Cosmic-Explorer-like detector to the KAGRA-type, with some minor modifications. As the arm length becomes longer, the finesse of the arm for the auxiliary laser is kept at the same value and the actuator efficiency of the VCO is reduced by a factor of ten. Besides, considering from the expected challenges listed above, the necessary modifications can be raised as follows.

- Noise level in the low frequency region ($\lesssim 1\,\mathrm{Hz}$) needs to be improved. In particular, the Doppler noise coupling and the effect of air turbulence should be improved. For the Doppler noise coupling, it would be effective to improve the sensitivity of the local sensors of the suspended mirrors. For air turbulence, it would be effective to put the optics on the POP and POS tables in vacuum and to reduce the length of differential optical path of the main and auxiliary lasers on the PSL table. The effect of such changes has to be quantitatively evaluated by a numerical simulation (Section 8.3).

- The control bandwidth of the arm PDH loops of the auxiliary lasers needs

to be lowered below the FSR.[‡2] In the ALS system of KAGRA, the bandwidth of this loop was 20 kHz. The effect of the bandwidth should be included in the simulation.

- The wavelength of the auxiliary lasers that are injected to the arms has to be changed from a half of that of the main laser. Here let us set the wavelength of the auxiliary lasers to 1950 nm. Thus the optical configuration around the PLLs between the main laser and the auxiliary lasers needs to be changed, since the SHG cannot be simply utilized to lock the frequency of the auxiliary laser with respect to the main laser frequency.

Wavelength conversion

Here the possible configurations around the PLLs are proposed, with a focus on alternatives to the SHG for connecting two distant wavelengths.

Let us first discuss the relationship between the wavelengths of the main and auxiliary lasers (λ_1 and λ_2, respectively). If two lasers with the wavelengths of λ_1 and λ_2 are injected to the same optical cavity having the cavity length of L, the phase deviation from the resonance for each laser (δ_j) is expressed as

$$\delta_j = \frac{4\pi L}{\lambda_j}\left(\frac{\Delta\lambda_j}{\lambda_j} - \frac{\Delta L}{L}\right) \quad (j = 1, 2). \tag{8.1}$$

Therefore, in order to sense δ_1 from δ_2, the relation

$$\frac{\Delta\lambda_1}{\lambda_1} = \frac{\Delta\lambda_2}{\lambda_2} \tag{8.2}$$

needs to hold. In the ALS systems of KAGRA and Advanced LIGO, this relation approximately holds thanks to the SHG. The ALS CARM control actuates the frequency of the main laser in such a way that $\Delta\lambda_1 = 2\Delta\lambda_2$ to keep the resonance of the auxiliary laser, i.e. $\delta_2 = 0$. As a result,

$$\delta_1 = \frac{4\pi\Delta L}{\lambda_1}\left(\frac{2\lambda_2}{\lambda_1} - 1\right), \tag{8.3}$$

which sets the lower bound in the coupling of arm length fluctuation. In the case of KAGRA in fact, $(2\lambda_2/\lambda_1 - 1) \sim 4 \times 10^{-7}$ considering the frequency offsets

[‡2] Although it is not impossible to have broader bandwidth than the FSR, it is safer to restrict the bandwidth within the FSR in the following consideration

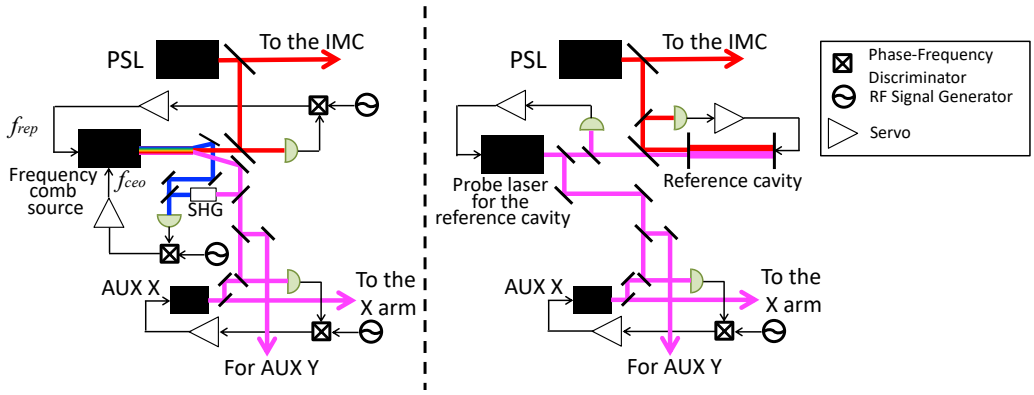

Figure 8.1: Possible configurations of the control of the auxiliary laser frequency. The left panel shows the configuration with an optical frequency comb for converting the wavelength of the main laser to that of the auxiliary laser. The right panel employs a dichroic reference cavity for the wavelength conversion.

introduced in the PLLs and the AOMs are at most 120 MHz. This number is small enough because, assuming $\Delta L \lesssim 10\,\mu$m,

$$\delta_1 \lesssim 2\pi \times 8 \times 10^{-6} \ll \frac{2\pi}{\mathcal{F}_{\rm carm}} = 2\pi \times 2 \times 10^{-4}, \tag{8.4}$$

which ensures the contribution of the arm length fluctuations in this mechanism is much smaller than the linewidth of CARM.

Equation (8.2) tells us that an alternative to the SHG has to connect two different wavelengths λ_1 and λ_2 as if it is a ruler of wavelength that stretches like a *rubber band*. The first example of the alternative is to utilize a technique called optical frequency comb [172]. The left panel of Figure 8.1 shows the possible application of the optical frequency comb to the 3G ALS. The optical field of a frequency comb consists of equidistant lines in the frequency domain. Each frequency can be expressed as

$$f_k = f_{\rm ceo} + k f_{\rm rep} \quad (f_{\rm ceo} < f_{\rm rep}). \tag{8.5}$$

$f_{\rm ceo}$ is called carrier envelope offset frequency and $f_{\rm rep}$ is called the pulse repetition rate. In the configuration depicted in Figure 8.1, the optical beat note between the main laser and the output of the frequency comb is detected and the phase of the beat note is controlled by feeding the demodulated beat note back to $f_{\rm rep}$. At the same time, $f_{\rm ceo}$ is kept constant by the f-$2f$ self-referencing scheme [173, 174]. In this way, $f_{\rm ceo}$ is fixed and $f_{\rm rep}$ varies in accordance with the

main laser frequency, and thus the frequency comb behaves like a rubber ruler. A fraction of the comb around the wavelength of λ_2 is guided so that it interferes with each auxiliary laser. The beat note between them is controlled so that the auxiliary laser frequency follows the frequency comb. As a whole, λ_2 follows λ_1 with the condition (8.2) satisfied, if the frequency of each optical beat note is not too large.[‡3] With the state-of-the-art technology, an optical frequency comb that covers spectrum in $\sim 1050 - 2100\,\mathrm{nm}$ with the frequency stability of 10^{-16} in 1 s is commercially available [175]. This stability corresponds to $\sim 3 \times 10^{-2}\,\mathrm{Hz}/\sqrt{\mathrm{Hz}}$ at 1 Hz, which should be stable enough; whether this stability level is enough or not is evaluated in the next section. Therefore, it is promising to apply this technique to the ALS system, though the research and development of applying it is lacking for now.

Another possible scheme to scale λ_1 to λ_2 is to use an optical cavity. The right panel of Figure 8.1 shows the configuration of such a scheme. A fraction of the main laser is sent to the reference cavity, and its length is controlled so that the main laser resonates in it. At the same time, a probe laser having wavelength of λ_2 is injected to the same cavity, with the frequency of the probe laser controlled at the resonance of the cavity. By the same mechanism that leads to Equation (8.2), the frequency of the probe laser scales as the main laser frequency varies. The beat note between the probe laser and the auxiliary laser is used to control the auxiliary laser frequency in the similar way. Let us next estimate the level of frequency noise introduced by this scheme. Sensing noise of the reference cavity of the two lasers becomes the noise source. The fundamental noise source is shot noise, whose ASD in terms of frequency, $\sqrt{S_{\mathrm{shot}}}$, can be written as

$$\sqrt{S_{\mathrm{shot}}(f)} = \frac{T}{2\pi L}\sqrt{\frac{hc^3}{8P_0\lambda}} \tag{8.6}$$

$$= 6 \times 10^{-5} \left(\frac{T}{3 \cdot 10^{-4}}\right) \left(\frac{0.1\,\mathrm{m}}{L}\right) \left(\frac{1.5\,\mu\mathrm{m}}{\lambda}\right)^{\frac{1}{2}} \left(\frac{0.1\,\mathrm{W}}{P_0}\right)^{\frac{1}{2}} \mathrm{Hz}/\sqrt{\mathrm{Hz}}, \tag{8.7}$$

where T is the transmissivity of the front and end mirror, L is the cavity length, λ is the wavelength of the laser, and P_0 is the incident optical power. Using the parameter set of $T = 3 \cdot 10^{-4}$, $L = 0.1\,\mathrm{m}$, and $P_0 = 0.1\,\mathrm{W}$, and considering shot noise in the sensing by both lasers, the shot-noise-limited noise level is

[‡3] As the discussion around Equation (8.4) shows, it would not be an issue if the beat note frequency is on the order of 100 MHz.

$\sim 1 \times 10^{-4}\,\mathrm{Hz}/\sqrt{\mathrm{Hz}}$. This number is low enough not to harm the overall noise performance of the ALS system. In fact, literature [176] reported the sensing noise level of $\lesssim 1 \times 10^{-2}\,\mathrm{Hz}/\sqrt{\mathrm{Hz}}$ at 1 Hz, which should also be stable enough though the sensing noise level was not limited by shot noise; if this level is enough or not is assessed in the next section. Thus the use of a dichroic reference cavity is also a promising candidate for the wavelength conversion.

In the above discussion, two configurations (optical frequency comb and dichroic reference cavity) are proposed and it seems that either is applicable. Let us assume the frequency noise level of $3 \times 10^{-2}\,\mathrm{Hz}/\sqrt{\mathrm{Hz}}$[‡4] for the following simulation of the overall noise performance to see if their noise performance will be sufficient.

8.3 Noise estimation

8.3.1 Methods

In order to extrapolate the characterization of the KAGRA ALS (Section 7.5) to the expected performance of the ALS system in the Cosmic-Explorer-like detector, the following two methods were taken.

The first method is to construct a noise simulation model of the 3G ALS as was done in the noise design of the KAGRA ALS (Section 7.2.2), by utilizing the noise spectrum of each component that was measured for the noise budget (Figure 7.17). By constructing the noise model, the contributions of all the considered noise sources are correctly evaluated. This method is flexible in the sense that the spectrum of each noise source can be individually adjusted; there is room for assuming improvement (or degradation) of each noise level. In the simulation, the following conditions and assumptions were adopted.

- The bandwidth of the arm cavity PDH loops was set to 2 kHz, which is smaller than the FSR of 3.75 kHz. The bandwidth of the ALS CARM loop was set to 1 kHz.

- An improvement by a factor of five in the Doppler noise coupling was assumed. For this improvement, it is necessary to have local sensors for the suspended mirrors such as PR2 with the sensitivity better than the level of $\sim 3 \times 10^{-7}\,\mathrm{m}/\sqrt{\mathrm{Hz}}$ around 0.5 Hz. This level is easily achievable with proper wind shields for the sensors [169].

[‡4]The use of SHG achieved $\lesssim 1 \times 10^{-4}\,\mathrm{Hz}/\sqrt{\mathrm{Hz}}$ around 1 Hz [177].

- It was assumed that the phase noise level due to air turbulence would be reduced by a factor of three from the upper edge of the red shaded area in Figure 7.17. As the ASD of the air-turbulence phase noise is proportional to the square root of the optical path length in air ($\sim 10\,\mathrm{m}$ was assumed for the KAGRA setup), shortening the path length to $\sim 1\,\mathrm{m}$ would be sufficient. It should be possible by putting the POP and POS optics in vacuum and making the optics related to the ALS in the PSL room as compact as possible.

- It was assumed that the frequency noise level associated with the wavelength conversion was $3 \times 10^{-2}\,\mathrm{Hz}/\sqrt{\mathrm{Hz}}$, as is mentioned in the previous section.

The obvious drawback of this method is that effect of unconsidered noise sources is ignored, which potentially leads to under-estimate of the overall noise level.

The second method is complementary to the first one. It is to simply recalibrate the measured sensing noise ASD of the KAGRA ALS to $\Delta f_{\mathrm{res}}(f;\kappa_{\mathrm{CARM}})$ or $\Delta f_{\mathrm{res}}(f;\kappa_{\mathrm{ARM}})$ using the 3G parameters. The advantage of this method is that contributions of noise sources that are not covered in the noise budget can be naturally included. This method is conservative in the sense that no improvement in each component is assumed. Meanwhile, this method has two drawbacks. One is that the effect of the narrowed control bandwidth cannot be taken into account. The other is that the contributions from some noise sources including the new scheme of the wavelength conversion will not be correctly included. However, these two can be assessed by the first method.

8.3.2 Results

Figure 8.2 shows the estimations of $\Delta f_{\mathrm{res}}(f;\kappa_{\mathrm{CARM}})$ by the first and second method, with a focus on the ALS CARM performance. The black trace shows the result of the second method; it was calculated in such a way that the sensing noise ASD of ALS CARM measured in KAGRA was simply calibrated to $\Delta f_{\mathrm{res}}(f;\kappa_{\mathrm{CARM}})$ of the Cosmic-Explorer-like detector. The RMS of the estimated ASD was 0.66 Hz, which is significantly larger than the CARM full linewidth of 0.12 Hz. This indicates that the ambitious target could not be achieved without any improvements.

The blue dashed line is the total noise level inferred by the first method, which is the quadrature sum of the contributions of all the considered noise sources that were numerically calculated using the noise model. The RMS of the total noise

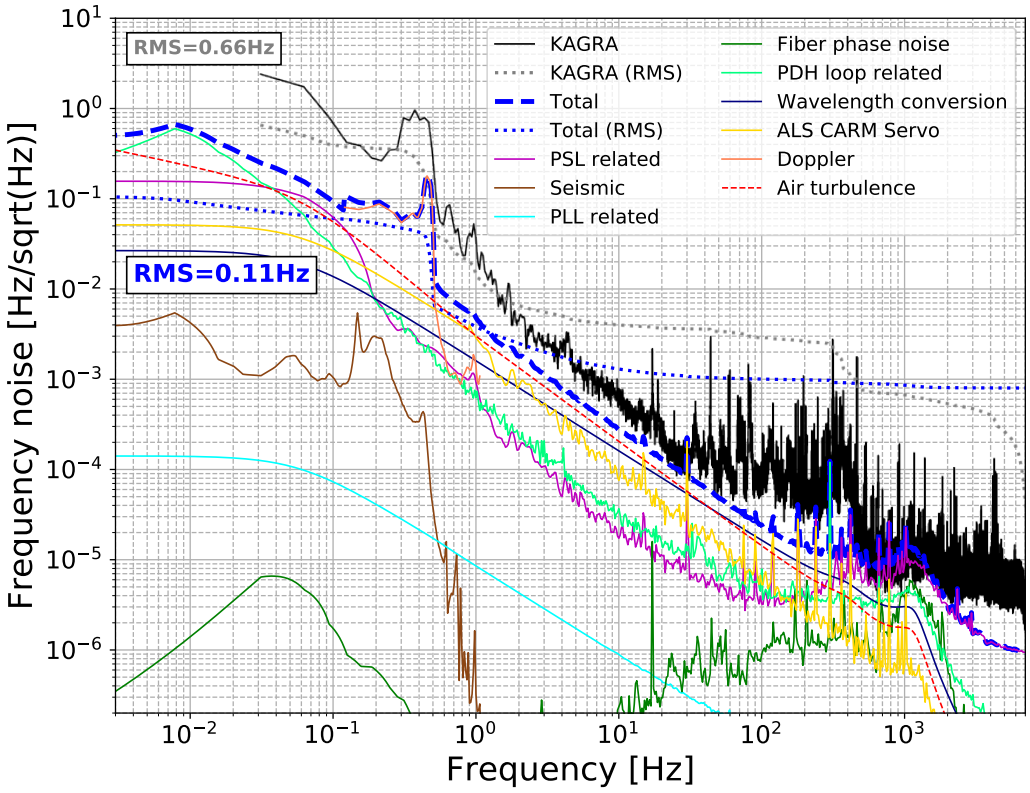

Figure 8.2: Expected ASDs of residual noise of CARM, $\Delta f_{\rm res}(f;\kappa_{\rm CARM})$, in the Cosmic-Explorer-like detector with CARM controlled by the ALS system. The black trace is simply calculated from the sensing noise level of ALS CARM measured in KAGRA (The second method). The gray dotted line is its cumulative RMS. The blue dashed line shows the quadrature sum of the contributions of all the considered noise sources (the first method). The blue dotted line shows its cumulative RMS. The descriptions of other traces are same as those for Figure 7.17, except for the navy line that shows the contribution of noise associated with the wavelength conversion.

spectrum was 0.11 Hz, which is slightly smaller than the CARM linewidth. Thus the ambitious target can be barely achieved in the Cosmic-Explorer-like detector by the ALS system. The noise spectrum is limited by three noise sources below ~ 10 Hz: (1) Doppler noise (orange line; $0.1 - 1$ Hz), (2) air turbulence (red line; $1 - 10$ Hz), and (3) electronics noise associated with the PDH loops (light green line; $0.03 - 0.3$ Hz), all of which contributed to the RMS. In particular, among the noise source (3), VCO noise was dominant.

The effect of the modification from the ALS system of KAGRA can also be extracted. The solid navy line shows the noise contribution from the wavelength conversion optics, which does not limit the total noise spectrum. It can be inferred that the effect of the narrowed bandwidth of the arm PDH loops was negligible by observing the following two points. One is that the structure in the total noise spectrum around 1 kHz, which is the unity gain frequency of the ALS CARM control loop, did not limit the RMS. This indicates that the overall control system of the ALS can be stably closed. The other is that the contributions of seismic noise (blown line) and PSL-related noise (magenta line) did not limit the total spectrum, which indicates that the suppression by the ALS control was sufficient in spite of the narrowed bandwidth of the control. Therefore, we can conclude that the effect of the modification on the overall noise performance will be negligible.

Let us move our attention to the single arm performance $\Delta f_{\rm res}(f;\kappa_{\rm ARM})$ with a focus on the primary noise requirement. Since it turned out that the effect of the modification would be negligible, $\Delta f_{\rm res}(f;\kappa_{\rm ARM})$ can be conservatively estimated by the second method. By converting the measurement results of sensing noise of the X and Y arm (shown in Figure 7.15), the RMS of $\Delta f_{\rm res}(f;\kappa_{\rm ARM})$ for the 3G ALS was obtained to be 1.9 Hz and 1.7 Hz, respectively (Figure 8.3). These numbers are smaller than the full linewidth of the single arm, 7.2 Hz. Therefore, it is expected, without any improvements assumed, that the primary noise requirement will be satisfied by the KAGRA-type ALS system in the Cosmic-Explorer-like detector.

The obtained results can be summarized as follows. The primary noise requirement of the ALS system in the Cosmic-Explorer-like detector can be satisfied by simply scaling up the KAGRA ALS with the minimum modifications: to change the wavelength conversion schemes, and to narrow the control bandwidth of the arm PDH loops. On the contrary, the estimation from the simple scaling did not reach the ambitious noise target. With modest improvement in the Doppler noise coupling and the air turbulence assumed, the simulation told us that the ambitious noise target can be barely achieved.

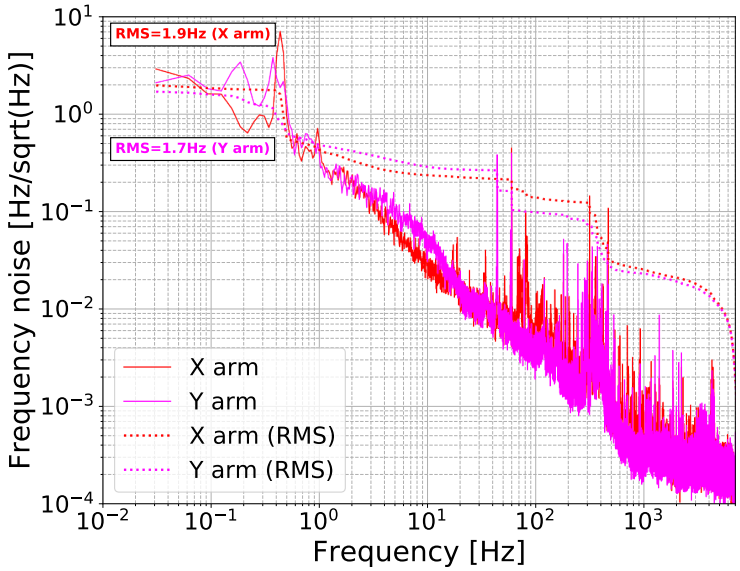

Figure 8.3: Expected noise performance of the single arm ALS in the Cosmic-Explorer-like detector (the second method). The measured ASDs of sensing noise of the single arm ALS in the KAGRA were simply converted by using the 3G parameters.

8.4 Discussion: sub-carrier CARM locking as common path ALS

According to the estimation results of the 3G ALS performance, the residual noise level of the arm DoFs controlled by the KAGRA-type system will be so small that the PSL frequency stays within the linewidth of a single arm cavity. Therefore, the control hand-over of DARM will be feasible, since the DARM linewidth is larger than that of the single arm. However, the direct hand-over of CARM might be challenging; the ambitious noise target can be slightly cleared even if the noise improvements are assumed.

In case that the direct hand-over is not feasible, the transmitted power of the arm cavities will be used as the CARM error signal in intermediate steps of the CARM hand-over. However, it is not trivial if the similar scheme is applicable to the 3G interferometers for the following reason. Since this scheme requires communication between digital controllers[‡5] in the end and corner stations, the

[‡5]This scheme is most likely to be realized by digital controllers, as one needs to calculate

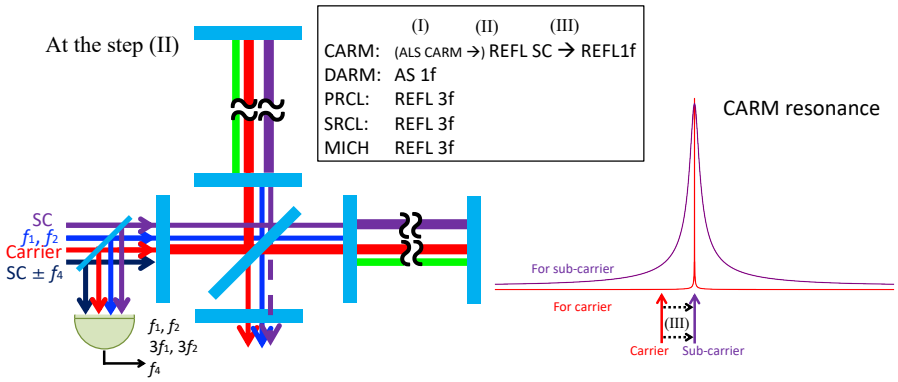

Figure 8.4: Conceptual diagram of the hand-over of the CARM control as the last step of lock acquisition. "SC" stands for sub-carrier.

sampling frequency of the transmission CARM will be limited by $\sim 3\,\mathrm{kHz}$[‡6] considering time delay due to the arm length (c.f. the FSR is 3.75 kHz). Therefore, the control bandwidth using this error signal will be narrower than that in the 2G detectors, which might result in lack of suppression gain for CARM. Here, apart from the conventional schemes, let us discuss a reliable locking scheme for CARM in the 3G detectors having ultra-narrow linewidth.

As mentioned in Section 5.3, an advantage of a conventional ALS scheme is closely related to an possible disadvantage in the following sense. Use of a different wavelength from the main laser enables us to sense the arm DoF independently and separately, by utilizing dichroic mirrors. However, at the same time, this feature makes it practically impossible that the main laser and the auxiliary laser propagate on the identical (or common) optical path. Due to this fact, a conventional ALS scheme suffers from the Doppler noise coupling and air turbulence, which will be problematic in locking CARM. Considering the above trade-off in a conventional ALS scheme, it would be helpful to have an auxiliary laser propagating on the common path for the purpose of CARM locking. Such a laser field can be regarded as a sub-carrier field. Researches discussed use of a sub-carrier field in the context of the control of the central interferometer [178–180]. Let us reconsider it as an extension of ALS.

Figure 8.4 shows a possible usage of the sub-carrier field in the DRFPMI with

the square root of the transmitted power.

[‡6]In the digital system commonly used in our field, sampling frequency is limited to 2^n Hz with n being integer. With this constraint, the sampling frequency would be limited by 2048 Hz.

the KAGRA-type ALS and sub-carrier field for lock acquisition. The outline of the proposed lock sequence is the following.

(I) While CARM is controlled by the ALS signals, the other DoFs are held by the main laser PDH signals, including the third harmonic demodulation signals. The PSL frequency is set slightly off from the CARM resonance so that the central DoFs are not disturbed.

(II) The CARM control is handed over from the ALS signal to the sub-carrier PDH signal (REFL f_4). The detail is described later.

(III) The operation point of the CARM control by the sub-carrier signal is gradually shifted to the CARM resonance for the carrier, and then the control is handed over to the carrier PDH signal at REFL port to complete CARM locking.

Figure 8.5 shows the schematic diagram of the interferometer and control configuration of the 3G detector focusing on the proposed lock acquisition scheme. The main laser, auxiliary lasers, and sub-carrier field are shown here, and all the associated control loops are also shown.

The frequency of the sub-carrier field with respect to the carrier field, $f_{\rm sc}$, should be chosen so that the sub-carrier field is close to the resonance of the PR cavity by itself when the carrier field satisfies the anti-resonant condition of it. By setting this condition, the CARM linewidth for the sub-carrier field is broadened by the PR cavity,[‡7] which will make the hand-over from the ALS control significantly easier. The frequency, $f_{\rm sc}$, should also be finely tuned so that it is close to an integer multiple of the FSR of the arm cavity. More practically, the frequency, $f_{\rm sc}$, should also be an integer multiple of the FSR of the IMC. It is possible to find such a frequency. In fact, assuming that the parameters of the central interferometer is same as those of KAGRA and the arm length is shortened by 174 mm from 40 km, $f_{\rm sc} = 225.077662\,\mathrm{MHz} \sim 5 \cdot f_2$ is an example of such a frequency offset from the carrier field; if $f_{\rm sc} \sim (2k+1) \cdot f_2$, where k is an integer, the sub-carrier field satisfies the resonant condition of the PR cavity. Figure 8.6 shows the structure of the resonances in the CARM cavity.

Figure 8.7 shows a possible optical layout on the PSL table for generating the sub-carrier field.[‡8] Phase-modulation at f_4 is separately applied to the sub-carrier

[‡7] In the same way as the SR cavity broadens the DARM linewidth for the carrier field.

[‡8] It should be beneficial to recombine the sub-carrier field before the IMC, since the IMC reduces the beam jitter (including higher order modes) of the sub-carrier field.

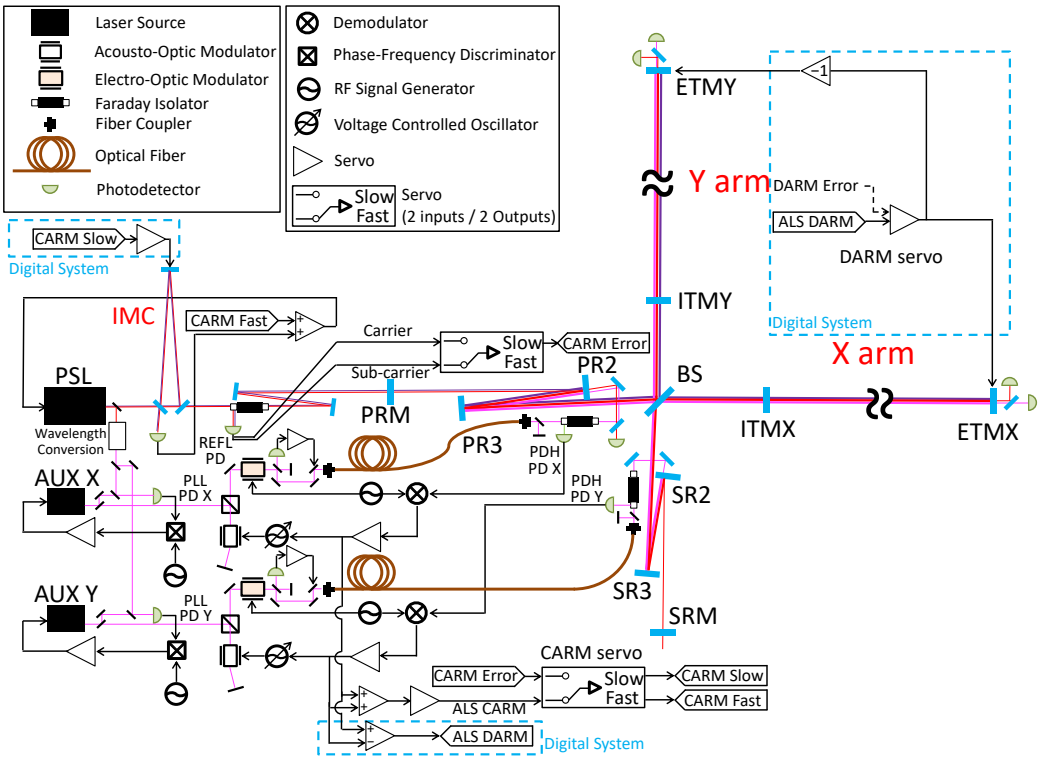

Figure 8.5: Schematic diagram of the interferometer and control configuration for a reliable lock acquisition scheme. All of the main laser (red), auxiliary lasers (magenta), and sub-carrier field (purple) are incorporated here.

field for the PDH technique of CARM sensing. By setting f_4 different from f_1 or f_2 (5.626946 MHz for example), the PDH signal associated with the sub-carrier can be independently extracted at REFL port. The beat note between the carrier and sub-carrier field is detected so that its phase is kept constant. This can be understood as a compact and complete extension of the combination of the PLL and the fiber noise cancellation loop in the KAGRA-type ALS system; this loop suppresses differential phase fluctuations between the main laser (carrier field) and the auxiliary laser (sub-carrier). Thus noise arising from the sub-carrier generation can be naturally included in our noise simulation model. The beat note detection can be performed on the PSL table, but it can also be done after the IMC, which would reduce the potential differential Doppler coupling between the carrier and sub-carrier field from the IMC.

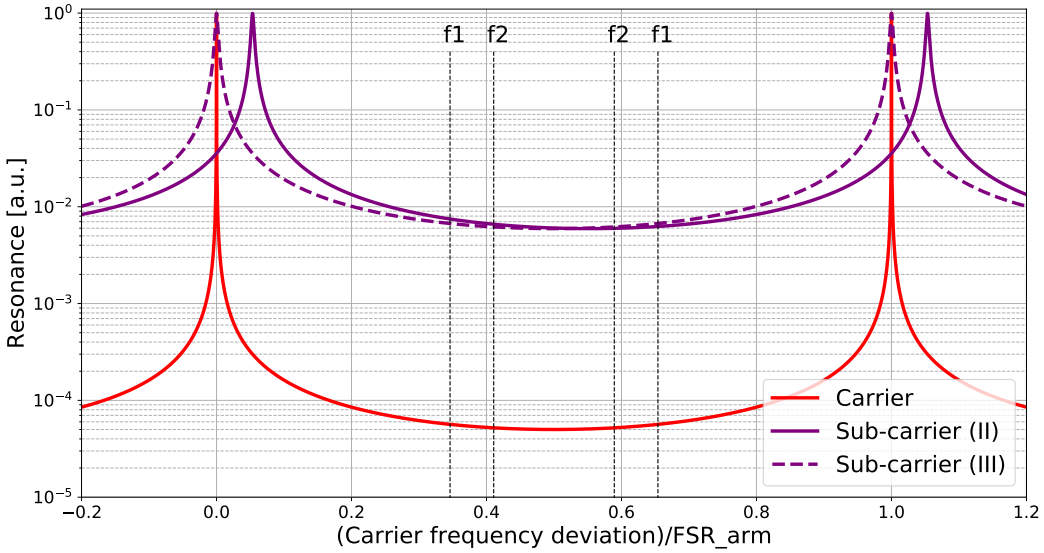

Figure 8.6: CARM resonance of the carrier and sideband fields in terms of the carrier frequency. The red line shows the resonance curve of the carrier field. The purple solid line shows that of the sub-carrier field in step (II), with $f_{\mathrm{sc}} = 225.077862\,\mathrm{MHz}$. The purple dashed line shows that of the sub-carrier field in step (III), with f_{sc} shifted by $-200\,\mathrm{Hz}$. The positions of the resonances of f_1 and f_2 sidebands are also shown for verifying that these resonances do not overlap with any other resonances.

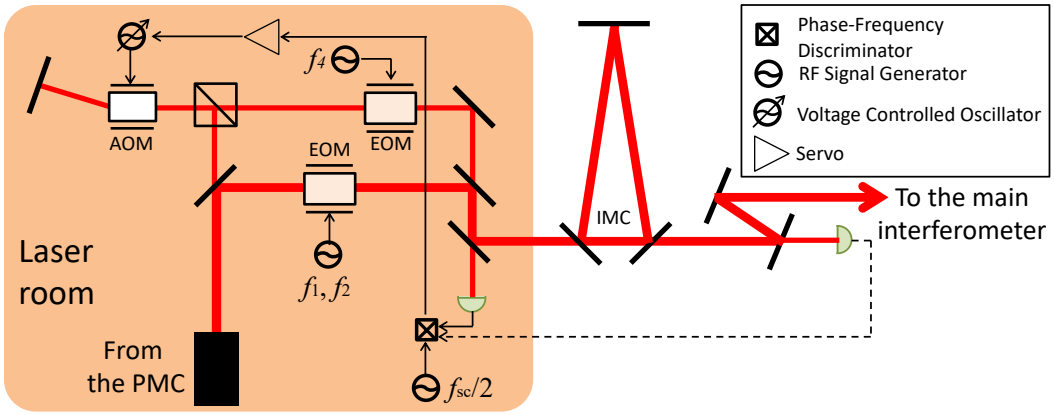

Figure 8.7: Layout of the optics for the generation of the sub-carrier field. A small fraction of the main laser is picked off, frequency-shifted, and then recombined.

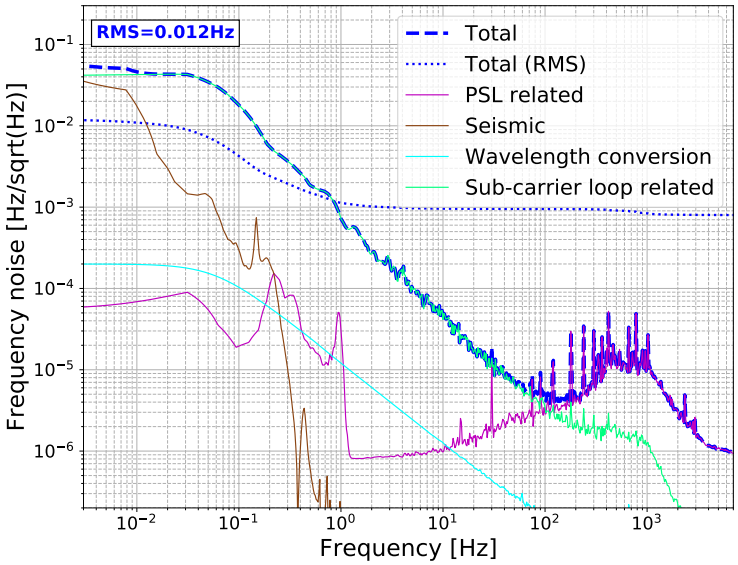

Figure 8.8: Noise budget plot of the sub-carrier scheme for the CARM control. Wavelength conversion corresponds to "PLL related" in the noise budget plot of the conventional ALS scheme. The Trace labeled as "Sub-carrier loop related" include shot noise, photodetector noise, and electronics noise associated with the sub-carrier sensing.

Let us estimate the noise level of the sub-carrier sensing for CARM. Since the sub-carrier sensing can be regarded as an extension of the KAGRA-type ALS, its noise performance can be estimated by using the similar noise simulation model. The differences from the noise budget (Figure 8.2) are that there will be no contributions from Doppler noise, air turbulence, and VCO noise, all of which are supposed to limit the overall noise performance of the 3G ALS system. Figure 8.8 show the result of the simulation for the sub-carrier control scheme. From the simulation result, the RMS is expected to be 1.2×10^{-2} Hz, which is significantly smaller than the CARM linewidth. Here, the optical power of the sub-carrier is assumed to be 100 mW.

In summary, we can expect that the use of sub-carrier will provide us with a smooth hand-over of the CARM control, since this scheme does not suffer from Doppler noise or air turbulence thanks to its common path feature. In addition, the sub-carrier CARM control can be realized with analogue circuits within the corner station. Thus it will be helpful for realization of the 3G interferometers.

Chapter 9
CONCLUSION

9.1 Summary of results

A new type of the ALS system was designed for interferometer locking of KAGRA. The new ALS scheme is scalable to the 3G GW detectors, thanks to the simplified configuration compared with the previous scheme. The study on the noise design told us that it can satisfy the noise requirement for lock acquisition of KAGRA that the RMS of residual frequency fluctuations of the main laser is smaller than the single arm linewidth. It was also expected that it can also potentially satisfy the ambitious noise target that the RMS of the residual frequency fluctuations is smaller than the CARM linewidth, which will simplify the lock acquisition sequence from what has been ever achieved before.

The new ALS system was implemented in KAGRA. By using the system, lock acquisition of the FPMI of KAGRA was achieved. Lock of the FPMI was demonstrated using the two different sequences; the CARM control was directly handed over from the ALS signal to the main laser PDH signal in the first one while the transmission power of the arm cavity was used as the CARM error signal in the intermediate step in the second one. The demonstration of locking the FPMI indicated that the performance of the ALS system was good enough for the full operation of the KAGRA interferometer, where the CARM linewidth is even narrower.

The noise performance of the ALS system was characterized in the KAGRA interferometer. The ASDs of sensing noise of the system were measured in the basis of the X and Y arm, and that of CARM and DARM. Their RMSs were 4.4 Hz for the X arm, 4.2 Hz for the Y arm, 2.7 Hz for CARM, and 2.8 Hz for DARM. All of them were smaller than the full linewidth of the single arm cavity, 33 Hz. The sensing noise ASD for CARM was intensively studied; the contributions of the possible noise sources on the overall noise performance of ALS

CARM were assessed, and the assessment showed that the improvement in the Doppler noise coupling is necessary for the system to satisfy the ambitious noise target. The effect of fiber phase noise was also studied, where the fiber noise cancellation helped the performance of the system, especially to broaden the DARM control bandwidth without the test mass actuators saturated.

Utilizing the results of the characterization of the KAGRA ALS system, the performance of the ALS system of a GW detector having as long arms as the 3G detectors was estimated for the first time. It was also indicated that a new scheme for converting wavelengths of lasers needs to be employed in the 3G ALS system. The possible candidates of the scheme, use of an optical frequency comb or a dichroic optical cavity, are raised and assessed. The estimation revealed that the primary noise requirement would be achieved by scaling up the KAGRA ALS system. It was also shown that it might be possible but challenging to achieve the ambitious noise target that the RMS of CARM fluctuations is smaller than 0.12 Hz. Thus the estimation results indicated that the lock acquisition process of 3G detectors can be achieved utilizing the KAGRA-type ALS system, but the CARM locking process might need a help from the transmission power of the arms as is done in Advanced LIGO if the ambitious target is not satisfied. To reinforce the CARM locking process, the use of a sub-carrier field was proposed and discussed from the viewpoint of ALS systems; this scheme can be regarded as an extension of ALS systems that has the auxiliary laser share exactly the same (common) path with the main laser. The noise estimation revealed that the proposed scheme can control the main laser frequency within the CARM linewidth.

9.2 Future prospects

As for the ALS system installed in KAGRA, the next thing to be done is to lock the DRFPMI, which is the final configuration of KAGRA, as soon as ITMs with good quality are ready. From the results shown in Chapter 7, it is feasible to lock the DRFPMI with the current performance, with a help of transmission signals as the CARM error signal. Meanwhile, by improving sensitivity of the local sensors of the BS, PR2, PR3, and SR3 by a factor of a few and fully utilizing them, it can be expected that reduction of the Doppler noise coupling leads to the improvement of the ALS system. This improvement will enable us to lock the DRFPMI in a simplified process, where the CARM control is directly handed over from the ALS signal to the main laser PDH signal even with the narrowed

linewidth of CARM.

Toward the realization of the 3G detectors from the viewpoint of lock acquisition, the following two things should be studied and developed. In preparation for the use of silicon as a test mass, the first thing is to develop schemes for the wavelength conversion, and to experimentally characterize the noise performance of them. The use of an optical frequency comb and the use of a dichroic optical cavity are raised as the candidates in Chapter 8. The second thing is to develop a sub-carrier lock scheme for CARM. The existing 2G detectors can probably be utilized for the development. After a system for sub-carrier generation is developed and evaluated, it can be implemented in the 2G detectors so that the lock acquisition scheme with sub-carrier sensing will be demonstrated and evaluated, in a similar way as the ALS system was characterized in KAGRA.

9.3 Conclusion

This work demonstrated that the KAGRA-type ALS system, where the auxiliary lasers are injected from the corner station, is an effective lock acquisition scheme of arm cavities in the 2G detectors. In particular, the performance of the system was better than the requirement of a 2G detector KAGRA, which showed that this scheme is capable of bringing the interferometer of the detector to the astrophysical observation mode. How the current performance can be improved was also clarified.

Utilizing the experimental results on the characterization of the system, this work also showed that the following issues, which had not been fully considered, will be critical in lock acquisition of the 3G detectors. The issues include Doppler noise, air turbulence, and alternatives to the SHG. By taking these issues into account, we proposed a realistic and reliable lock acquisition scheme applicable to the 3G detectors. Thus this work has paved the way for realizing the operation of the 3G GW detectors in the astrophysical observation mode.

Appendix A
SPECTRAL ANALYSIS

Let us prepare a formalism to treat probabilistic fluctuations of a time-varying physical quantity in frequency domain. Functions called power spectral density (PSD) and amplitude spectral density (ASD) are widely used. A PSD characterizes the contribution to the variance of the quantity at each frequency bin. An ASD is given by the square root of A PSD. The unit of a PSD for a physical quantity whose unit is [m], for example, is [m^2/Hz], while that of the ASD is [$m/\sqrt{Hz}$].

Let us consider the PSD of a quantity $x(t)$.[‡1] Let us assume that statistical property of x does not change in time, and the average of x is zero. By using the finite-time Fourier transform of $x(t)$, which is given by[‡2]

$$x_T(\Omega) = \int_{-T/2}^{T/2} dt\, x(t) \mathrm{e}^{-i\Omega t}, \tag{A.1}$$

the PSD[‡3] is defined by the following equation:

$$S_x(f) := \lim_{T\to\infty} \frac{1}{T} \left\langle x_T^\dagger(2\pi f) x_T(2\pi f) + x_T(2\pi f) x_T^\dagger(2\pi f) \right\rangle. \tag{A.2}$$

Here, $\langle\cdot\rangle$ denotes the expectation value of a quantity. A PSD has the following relation with the auto-correlation function $C_x(\tau)$ [181]:

[‡1] x can either be a classical probabilistic variable or a quantum observable in the Heisenberg picture.

[‡2] If the sampling frequency is finite, the integral is replaced by a summatoin.

[‡3] This is called the one-sided (single-sided) PSD, more specifically, because the interval of integration in Equation (A.6) is one side of the frequency space.

$$C_x(\tau) = \frac{1}{2}\langle x(t)x(t+\tau) + x(t+\tau)x(t)\rangle, \tag{A.3}$$

$$S_x(f) = 2\int_{-\infty}^{\infty} d\tau\, C_x(\tau)\mathrm{e}^{-2\pi i f\tau}, \tag{A.4}$$

$$C_x(\tau) = \frac{1}{2}\int_{-\infty}^{\infty} df\, S_x(f)\mathrm{e}^{2\pi i f\tau} = \int_0^{\infty} df\, S_x(f)\cos(2\pi f\tau). \tag{A.5}$$

Substituting $\tau = 0$, the relation between the variance $\langle x^2(t)\rangle$ and the PSD is obtained:

$$\langle x^2(t)\rangle = \int_0^{\infty} df\, S_x(f). \tag{A.6}$$

This relation shows that the PSD is the contribution to the variance of the quantity at each frequency bin.

Similarly, a cross spectral density of $x(t)$ and $y(t)$ is defined by

$$S_{xy}(f) := \lim_{T\to\infty}\frac{1}{T}\left\langle x_T^{\dagger}(2\pi f)y_T(2\pi f) + y_T(2\pi f)x_T^{\dagger}(2\pi f)\right\rangle, \tag{A.7}$$

which includes the definition of a PSD. The similar relation between the cross spectral density and the cross-correlation function $C_{xy}(\tau)$ holds [181]:

$$C_{xy}(\tau) = \frac{1}{2}\langle x(t)y(t+\tau) + y(t+\tau)x(t)\rangle, \tag{A.8}$$

$$S_{xy}(f) = 2\int_{-\infty}^{\infty} d\tau\, C_{xy}(\tau)\mathrm{e}^{-2\pi i f\tau}, \tag{A.9}$$

$$C_{xy}(\tau) = \frac{1}{2}\int_{-\infty}^{\infty} df\, S_{xy}(f)\mathrm{e}^{2\pi i f\tau} = \int_0^{\infty} df\, S_{xy}(f)\cos(2\pi f\tau). \tag{A.10}$$

Equations

$$S_{xy}(f) = S_{yx}^{*}(f), \tag{A.11}$$

$$C_{xy}(\tau) = C_{yx}(-\tau) \tag{A.12}$$

also hold. Equation (A.7) can be formally expressed as

$$\delta(f-f')S_{xy}(f) = \left\langle x^{\dagger}(2\pi f)y(2\pi f') + y(2\pi f')x^{\dagger}(2\pi f)\right\rangle, \tag{A.13}$$

where

$$x(\Omega) := \lim_{T\to\infty} x_T(\Omega). \tag{A.14}$$

Appendix B
CLASSICAL CONTROL THEORY

B.1 Linear system

Let us consider a system (Figure B.1 (a)) that has an input $x(t)$ and an output $y(t)$. Let us assume that $y(t)$ is written as

$$y(t) = \int_0^\infty d\tau\, T(\tau)x(t-\tau), \tag{B.1}$$

which makes the system linear. By utilizing the Laplace transformation, which is defined by

$$x(s) = \int_0^\infty dt\, x(t)\mathrm{e}^{-st}, \tag{B.2}$$

Equation (B.1) leads to

$$y(s) = T(s)x(x). \tag{B.3}$$

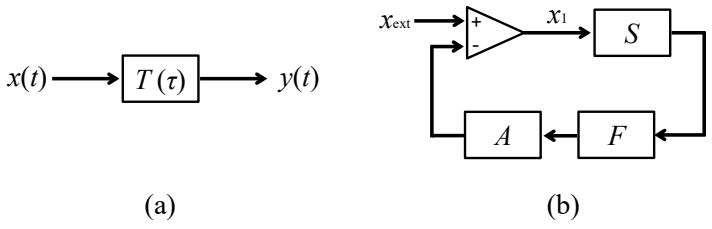

Figure B.1: (a) Linear system with a transfer function T. (b) Feedback control system.

Here $T(s)$ is called transfer function of the system. We often use angular frequency $\Omega\,(=-is)$ as the argument instead of s.

When $T(s)$ is written in a form of rational function,

$$T(s) = kN(s)/D(s), \tag{B.4}$$

$$N(s) = \prod_l (s - z_l), \tag{B.5}$$

$$D(s) = \prod_m (s - p_l), \tag{B.6}$$

where k is a numerical factor, z_l and p_l are called zeros and poles of the system. For example, a system with a single pole at $p\,(<0)$ shows characteristic of a low-pass filter with a corner frequency of $|p|$. If the system has a pole whose real part is positive, the system is unstable; arbitrary small input would lead to infinite output [182]. This is because the inverse-Laplace transform of $1/(s-a)$ is e^{at}.

B.2 Feedback loop and its stability

Let us consider a series of systems, which forms a loop (Figure B.1 (b)). From a straightforward calculation, we obtain

$$x_1(s) = \frac{1}{1+G(s)} x_{\mathrm{ext}}(s), \tag{B.7}$$

$$G(s) = A(s)F(s)S(s), \tag{B.8}$$

where $G(s)$ is called the open loop transfer function. In particular, $|G(s)|$ is called the open loop gain.

This system is a primitive example of a feedback control system. Let us interpret x_{ext} as external disturbances to the system, and S as the transfer function of a sensor for x. By taking the open loop gain arbitrary large, x_1 can be arbitrary small, which is how a feedback control works. Even if the linear range of the sensor is smaller than the range of x_{ext}, the feedback control makes it possible for the sensor to always sense it.

Although large gain is desirable for suppressing the disturbed motion of x, there is a limitation to the open loop transfer function coming from the stability condition of the whole system. On the assumption that each of S, F, and A is stable, if and only if 1/(1+G) does not have a pole whose real part is positive, the

whole system is stable. It is known that there is a useful criterion to topologically judge the stability, which is called the Nyquist stability criterion. Let C be an infinitely large semicircular arc on the right side of the complex plane, and D be the trajectory of $G(s)$ with $s \in C$. The condition can be described as: the system is unstable if and if only D rotates around the point -1 on the complex plane more than once [182] (Figure B.2 (a)). If the shape of G is simple, the stability can be judged from a Bode plot of G by looking at the phase at unity gain frequency (Figure B.2 (b)).[‡1]

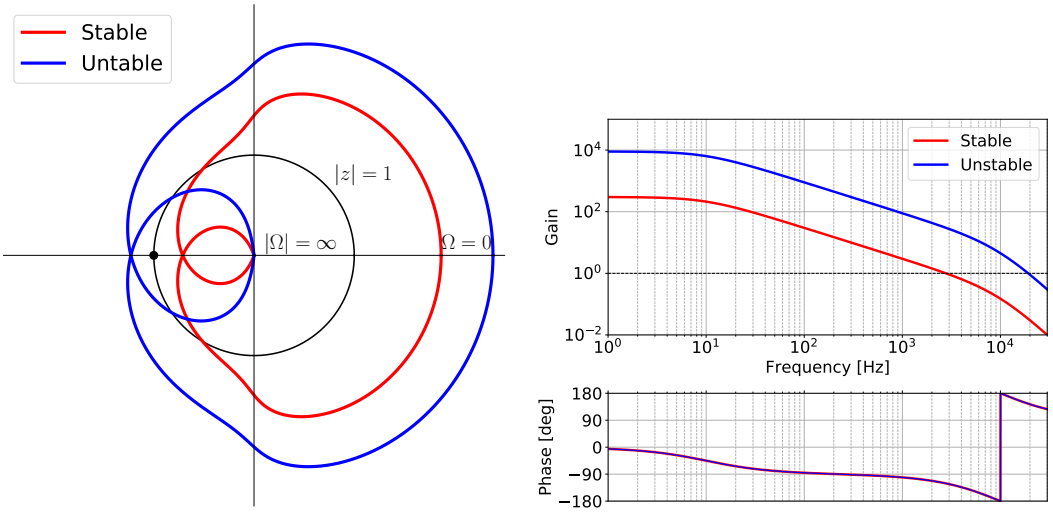

(a) (b)

Figure B.2: (a) Nyquist diagrams of the open loop transfer functions G in stable and unstable cases. The blue line rotates around the point -1, while the red one does not. (b) Bode plot of G in stable and unstable cases. The blue one crosses the line of $|G| = 1$ with the phase being lower than -180 deg, while the red one crosses with the phase being higher than -180 deg.

[‡1]Unity gain frequency is the frequency at which the open loop gain is unity.

Appendix C
FABRY–PEROT CAVITY

A Fabry–Perot cavity is an optical cavity composed of two parallel reflecting mirrors. A light field propagates in the cavity many times and then it is amplified inside. Here let us summarize the equations describing how a light field behaves in a Fabry–Perot cavity.

Let us calculate static field associated with a cavity shown in Figure C.1. The field in the cavity E_{cav} can be calculated by an infinite series:

$$E_{\mathrm{cav}}(t) = \sum_{n=0}^{\infty} t_1 E_{\mathrm{i}}(t) \left(r_1 r_2 \mathrm{e}^{-i\phi}\right)^n \tag{C.1}$$

$$= \frac{t_1}{1 - r\mathrm{e}^{-i\phi}} E_{\mathrm{i}}(t), \tag{C.2}$$

where $r = r_1 r_2$, and ϕ is roundtrip phase of the cavity. The reflection and the transmission can also be calculated, by using this, as

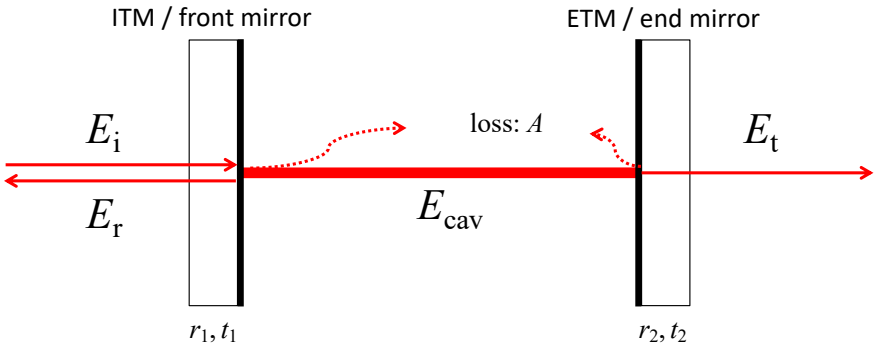

Figure C.1: Schematic view of a Fabry–Perot cavity and associated electric fields.

$$E_{\mathrm{t}}(t) = \frac{t_1 t_2}{1 - r\mathrm{e}^{-i\phi}} E_{\mathrm{i}}(t), \tag{C.3}$$

$$E_{\mathrm{r}}(t) = \left[-r_1 + \frac{t_1^2 r_2 \mathrm{e}^{-i\phi}}{1 - r\mathrm{e}^{-i\phi}} \right] E_{\mathrm{i}}(t). \tag{C.4}$$

It is worth noting that, if we set $\phi \equiv 0 \,(\mathrm{mod}\, 2\pi)$, $r_1 = r_2$, and $A = 0$, it follows that $E_{\mathrm{t}}(t) = E_{\mathrm{i}}(t)$, and $E_{\mathrm{t}}(r) = 0$. This regime is utilized for cavies called mode cleaners.

From Equation (C.2), the optical power in the cavity can be calculated as

$$P_{\mathrm{in}} = \frac{T_1}{(1-r)^2 + 4r \sin^2(\phi/2)} P_0 \tag{C.5}$$

$$\simeq \frac{4T_1}{(1-R)^2 + 4\delta\phi^2} P_0, \quad (1 - R \ll 1,\ |\delta\phi| \ll 1), \tag{C.6}$$

where $R = r^2$, $T_1 = t_1^2$, and $\delta\phi \equiv \phi \,(\mathrm{mod}\, 2\pi)$, $-\pi < \delta\phi \leq \pi$. Figure C.2 describes how the optical power in the cavity changes as ϕ changes. The half width at the half maximum of the resonance of the cavity is called cavity pole frequency f_{cav}, which can be expressed as

$$f_{\mathrm{cav}} := \frac{c}{2\pi L} \arcsin \frac{1-r}{2\sqrt{r}} \simeq \frac{c}{8\pi L}(1 - R). \tag{C.7}$$

The finesse $\mathcal{F}$ of the cavity is defined by a ratio of the FSR ($= c/2L$) to the full width at the half maximum ($= 2f_{\mathrm{cav}}$), which is

$$\mathcal{F} := \frac{2\pi}{4 \arcsin[(1-r)/2\sqrt{r}]} \simeq \frac{2\pi}{1-R}. \tag{C.8}$$

An average number of roundtrips in the cavity N_{avg} can be expressed using the finesse:

$$N_{\mathrm{avg}} = \sum_{n=0}^{\infty} n \cdot (1-R) R^n \tag{C.9}$$

$$= \frac{R}{1-R} \simeq \frac{\mathcal{F}}{2\pi}. \tag{C.10}$$

Similarly, the average storage time of the cavity τ_s can be expressed as

$$\tau_s \simeq \frac{2L}{c} \frac{\mathcal{F}}{2\pi}. \tag{C.11}$$

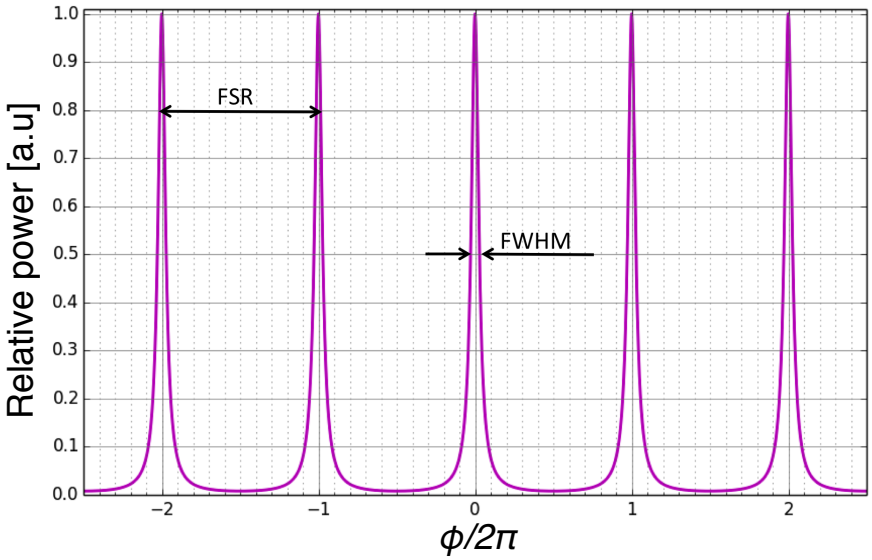

Figure C.2: Optical power in a cavity and roundtrip phase.

These equations show the physical meanings of finesse.

Let us then consider the dynamical property of a cavity around the resonance. For simplicity, let us set $r_2 = 1$ and $A = 0$. For time-dependent variations of roundtrip phase around $\phi \equiv 0$, the reflection field can be written as

$$
\begin{aligned}
E_{\mathrm{r}}(t)/E_{\mathrm{i}}(t) &= -\left[1 - iC_{\mathrm{FP}}\delta\phi_{\mathrm{cav}}(f)\right], \\
C_{\mathrm{FP}}(\Omega) &= \frac{r^{1/2}(1+r)}{2\sinh\left[\frac{|\ln r|}{2}\left(1 + i\Omega/\Omega_{\mathrm{cav}}\right)\right]} \qquad (4.22) \\
&\simeq \frac{2\mathcal{F}}{\pi}\frac{1}{1 + i\Omega/\Omega_{\mathrm{cav}}} \quad \left(1 - r \ll 1,\ \frac{\Omega}{2\pi} \ll f_{\mathrm{FSR}}\right). \qquad (4.23)
\end{aligned}
$$

Similarly, in the presence of dynamical change of input laser phase (or equivalently frequency), the reflection field can be written as

$$E_{\mathrm{r}}(t)/E_{\mathrm{i}}(t) = -\left[1 + iD_{\mathrm{FP}}\delta\phi_{\mathrm{i}}(f)\right], \tag{C.12}$$

$$D_{\mathrm{FP}}(\Omega) = \frac{(1+r)(\mathrm{e}^{-2iL\Omega/c} - 1)}{1 - r\mathrm{e}^{-2iL\Omega/c}} \tag{C.13}$$

$$\simeq -\frac{2\mathcal{F}}{\pi}\frac{1}{1 + i\Omega/\Omega_{\mathrm{cav}}}\frac{2Li\Omega}{c} \quad \left(1 - r \ll 1,\ \frac{\Omega}{2\pi} \ll f_{\mathrm{FSR}}\right). \tag{C.14}$$

Here $\delta\phi_{\mathrm{cav}}$ is the deviation of the roundtrip phase inside the cavity, $\delta\phi_{\mathrm{i}}$ is phase fluctuations of the incident laser, and $\Omega_{\mathrm{cav}} = 2\pi f_{\mathrm{cav}}$. Note that $i\Omega\delta\phi_{\mathrm{i}}$ corresponds to (angular) frequency fluctuations of the incident laser. From these equations, a Fabry–Perot cavity has a low-pass response with the corner frequency of f_{cav}. Figure 4.9 shows the typical shape of the transfer function of Equation (C.13).

Appendix D
SIDEBAND PICTURE AND MODULATION

Let us consider a electrical field with phase and amplitude modulations applied to it, which can be written as

$$E = A(1 + \beta_{\mathrm{am}} \cos(\Omega_{\mathrm{m}} t + \phi_{\mathrm{am}})) \exp\left[i\omega_0 t + i\beta_{\mathrm{pm}} \cos(\Omega_{\mathrm{m}} t + \phi_{\mathrm{pm}})\right]. \tag{D.1}$$

Here, ω_0 is the angular frequency of the field without modulations, Ω_{m} is modulation frequency, and β is modulation amplitude, which we assumed to be significantly smaller than one. The expression of the field can be written in the following form:

$$E = A\mathrm{e}^{i\omega_0 t} + A_u \mathrm{e}^{i(\omega_0+\Omega_{\mathrm{m}})t} + A_l \mathrm{e}^{i(\omega_0-\Omega_{\mathrm{m}})t}, \tag{D.2}$$

$$A_u = \frac{A}{2}\left(\beta_{\mathrm{am}} \mathrm{e}^{i\phi_{\mathrm{am}}} + i\beta_{\mathrm{pm}} \mathrm{e}^{i\phi_{\mathrm{pm}}}\right), \tag{D.3}$$

$$A_l = \frac{A}{2}\left(\beta_{\mathrm{am}} \mathrm{e}^{-i\phi_{\mathrm{am}}} + i\beta_{\mathrm{pm}} \mathrm{e}^{-i\phi_{\mathrm{pm}}}\right). \tag{D.4}$$

This expression indicates that the modulated field is equivalent to the combination of three monochromatic fields at frequencies of ω_0 and $\omega_0 \pm \Omega_{\mathrm{m}}$ (Figure D.1). The field having the frequency of ω_0 is called carrier field, and the field with $\omega_0 \pm \Omega_{\mathrm{m}}$ are called upper and lower sidebands, respectively. Similarly, a combination of the upper and lower sidebands can be interpreted as a certain combination of amplitude and phase modulations.

By employing the sideband picture for modulations, we can understand that the modulation frequencies for the main interferometer sensing should be set to integer multiples of the FSR of the IMC; otherwise no modulations appear after the IMC. The term *resonant sideband extraction* can also be understood with

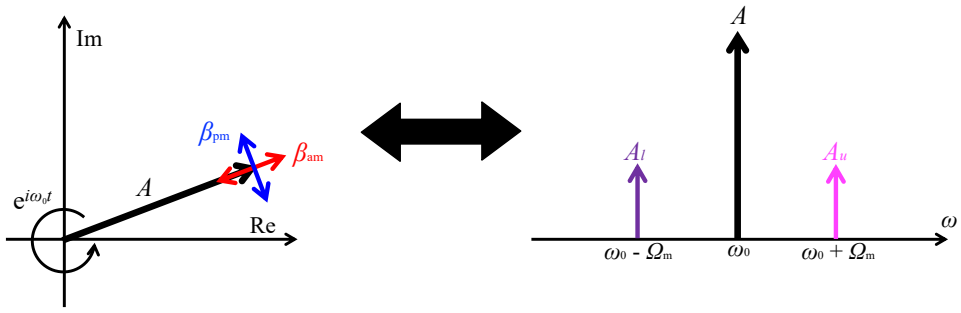

Figure D.1: Modulation picture and sideband picture.

the sideband picture. The GWs modulate the laser field in the arm cavities, and this modulation can be expressed as audio-band sidebands. The SR cavity tunes the finesse of the arm cavity for these GW sidebands. A sub-carrier field is a single sideband so it can also be understood as a combination of amplitude and phase modulation to the carrier field.

Appendix E
QUANTUM STATE OF LIGHT

Let us summarize commonly used quantum states of light field for describing laser fields in the interferometer [183, 184].

E.1 Vacuum state

Let $\hat{a}_\omega$ be an annihilation operator of electromagnetic field in the fundamental Hermite-Gauss mode. Quadrature operators $\hat{a}_j(z,t)$, $(j=1,2)$ are defined by

$$\hat{a}_1(\Omega) = \frac{1}{\sqrt{2}}\left(\hat{a}_{\omega_0+\Omega} + \hat{a}^\dagger_{\omega_0-\Omega}\right), \tag{E.1}$$

$$\hat{a}_2(\Omega) = \frac{1}{i\sqrt{2}}\left(\hat{a}_{\omega_0+\Omega} - \hat{a}^\dagger_{\omega_0-\Omega}\right), \tag{E.2}$$

$$\hat{a}_j(z,t) = \int_0^\infty \frac{\mathrm{d}\Omega}{2\pi}\left(\hat{a}_j(\Omega)\mathrm{e}^{i\Omega(z/c-t)} + \hat{a}^\dagger_j(\Omega)\mathrm{e}^{-i\Omega(z/c-t)}\right), \quad (j=1,2). \tag{E.3}$$

Here, ω_0 can be understood as the carrier frequency while Ω as the sideband frequency. The interpretations of the quadrature operators are given later.

The vacuum state $|0\rangle$ is defined by the equation

$$\hat{a}_\omega |0\rangle = 0. \tag{E.4}$$

This leads to

$$\left\langle \hat{a}^\dagger_j(\Omega)\hat{a}_k(\Omega') + \hat{a}_k(\Omega')\hat{a}^\dagger_j(\Omega)\right\rangle = 2\pi\delta_{jk}\delta(\Omega-\Omega'). \tag{E.5}$$

Therefore, according to Equation (A.13), the PSDs and cross spectral densities of $\hat{a}_j(z,t)$ in the vacuum state are written as

$$S_{jk}(f) = \delta_{jk}, \quad (j,k=1,2). \tag{E.6}$$

E.2 Coherent state

A coherent state $|\alpha\rangle$ is defined by applying a displacement operator $\hat{D}[\alpha]$ to the vacuum state:

$$|\alpha\rangle = \hat{D}[\alpha]\,|0\rangle =: \exp\left[\int_0^\infty \frac{d\omega}{2\pi}\,\alpha(\omega)\hat{a}_\omega^\dagger - \alpha^\dagger(\omega)\hat{a}_\omega\right]|0\rangle\,. \tag{E.7}$$

A coherent state is an eigenstate of the annihilation operator satisfying

$$\hat{a}_\omega|\alpha\rangle = \alpha(\omega)|\alpha\rangle. \tag{E.8}$$

When calculating expectation values in a coherent state, instead of applying $\hat{D}[\alpha]$ to the vacuum state, we can displace the operator $\hat{O}$ by

$$\hat{O} \to \hat{D}^\dagger[\alpha]\hat{O}\hat{D}[\alpha]. \tag{E.9}$$

For example, the annihilation operator can be transformed by

$$\hat{a}_\omega \to \alpha(\omega) + \hat{a}_\omega. \tag{E.10}$$

Because this form is so simple, let us employ this convention of displacing the operator instead of the vacuum state.

If we set $\alpha(\omega)$ specifically by

$$\alpha(\omega) = \frac{A}{\sqrt{2}}2\pi\delta(\omega - \omega_0), \tag{E.11}$$

the coherent state describes the following electric field:

$$\hat{E}(\boldsymbol{x},t) \propto u_{00}(\boldsymbol{x})\left\{[A + \hat{a}_1(z,t)]\cos\left(\omega_0 t - \frac{\omega_0 z}{c}\right) + \hat{a}_2(z,t)\sin\left(\omega_0 t - \frac{\omega_0 z}{c}\right)\right\}, \tag{E.12}$$

where $u_{00}(\boldsymbol{x})$ describes the spatial distribution of the fundamental Hermite-Gauss mode. This expression of the electric field provides the physical interpretation of the coherent state and quadrature operators. The coherent state describes a monochromatic electric field of laser light. $\hat{a}_1(z,t)$ corresponds to quantum fluctuations of amplitude modulation to the monochromatic light, while $\hat{a}_2(z,t)$ corresponds to quantum fluctuations of phase modulation. According to Equation (E.6), the variances of quantum fluctuations of amplitude and phase modulation are same, and they are uncorrelated.

E.3 Squeezed state

In a similar way to a coherent state, a squeezed state is given by applying a squeezing operator $\hat{S}[\chi]$ to the vacuum state:

$$|\chi\rangle = \hat{S}[\chi]\,|0\rangle =: \exp\left[\int_0^\infty \frac{d\Omega}{2\pi}\,\chi(\Omega)\hat{a}^\dagger_{\omega_0+\Omega}\hat{a}^\dagger_{\omega_0-\Omega} - \chi^\dagger(\Omega)\hat{a}_{\omega_0+\Omega}\hat{a}_{\omega_0-\Omega}\right]|0\rangle\,. \tag{E.13}$$

Here again, let us apply $\hat{S}[\chi]$ to operators instead. By setting $\chi(\Omega) = \xi_\Omega \mathrm{e}^{-2i\phi_\Omega}$, the quadrature operators are transformed as

$$S^\dagger \hat{a}_1 S = \hat{a}_1(\cosh\xi + \sinh\xi\cos 2\phi) - \hat{a}_2 \sinh\xi \sin 2\phi, \tag{E.14}$$

$$S^\dagger \hat{a}_2 S = -\hat{a}_1 \sinh\xi \sin 2\phi + \hat{a}_2(\cosh\xi - \sinh\xi\cos 2\phi). \tag{E.15}$$

This transformation can be re-arranged, by using

$$\hat{a}_\zeta = \hat{a}_1 \cos\zeta + \hat{a}_2 \sin\zeta, \tag{E.16}$$

into

$$S^\dagger \hat{a}_{-\phi}\, S = \hat{a}_{-\phi}\,\mathrm{e}^{\xi}, \tag{E.17}$$

$$S^\dagger \hat{a}_{\frac{\pi}{2}-\phi}\, S = \hat{a}_{\frac{\pi}{2}-\phi}\,\mathrm{e}^{-\xi}. \tag{E.18}$$

Quantum fluctuations in the direction of $-\phi$ are amplified by a factor of e^{ξ}, while those in the direction of $\pi/2-\phi$ are squeezed by a factor of e^{ξ}. Figure E.1 illustrates quantum fluctuations of quadrature operators $\hat{a}_j(z,t)$ in the vacuum or a squeezed state. Note that ϕ and ξ can be dependent on Ω. Such a case is called frequency-dependent squeezing.

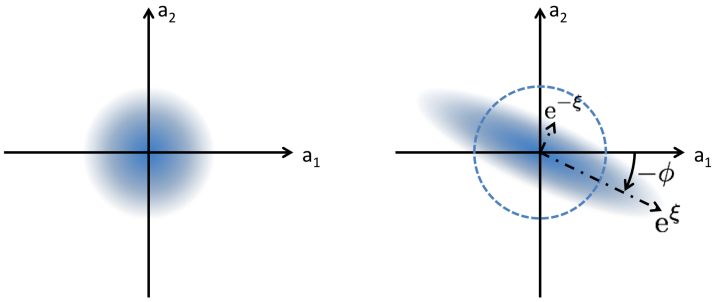

Figure E.1: Schematic diagram of quantum fluctuations of the vacuum state (left panel) and a squeezed state (right).

Appendix F
PRELIMINARY MEASUREMENTS

F.1 Fiber phase noise measurement

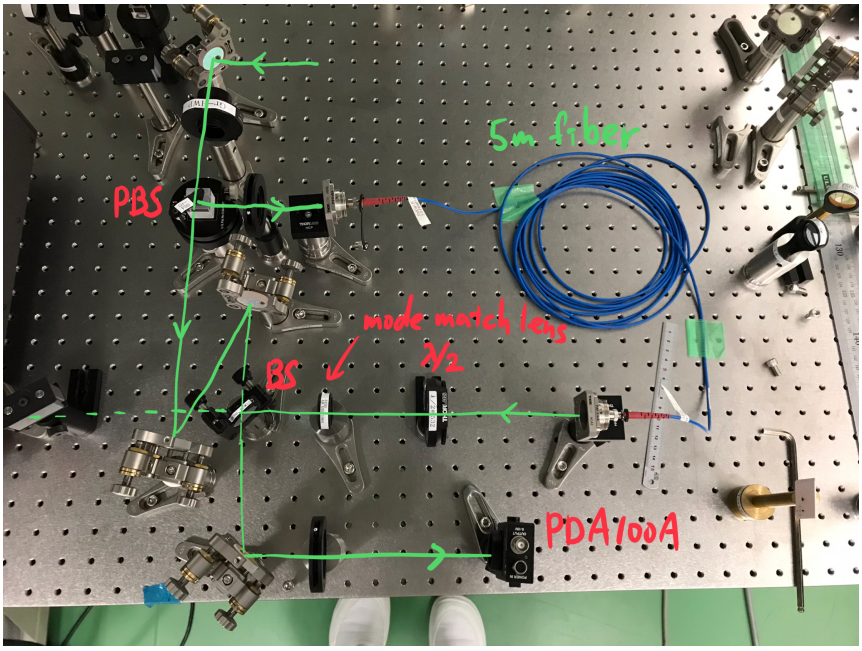

Figure F.1: Picture of the experimental setup for the preliminary measurement of fiber phase noise.

Figure F.1 shows the experimental setup for the preliminary measurement of fiber phase noise. This measurement was done on an optical table in the

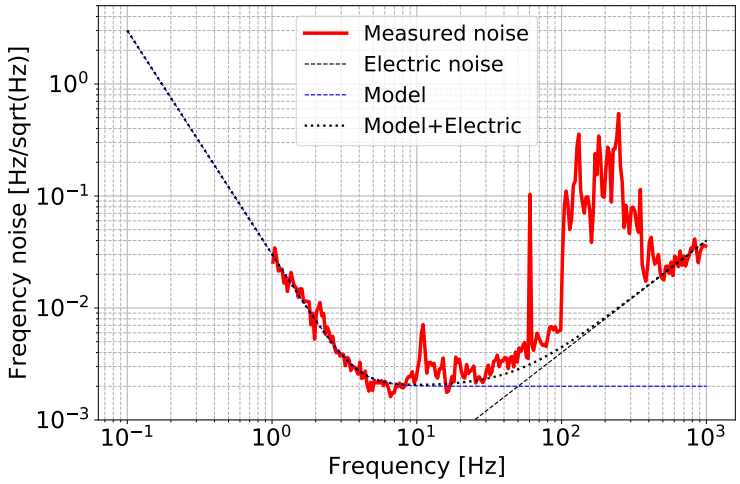

Figure F.2: ASD of fiber frequency noise in the preliminary measurement.

University of Toyama. A Mach–Zehnder interferometer was formed in such a way that one path is free space, while the other path has a 5-m long optical fiber. The Mach–Zehnder interferometer was kept at the mid-fringe simply by using the output optical power as the error signal. The error signal was fed back to the laser frequency to close the control. Figure F.2 shows the obtained ASD of fiber frequency noise. Because we considered that, in the high frequency region ($f > 40\,\mathrm{Hz}$), the measured ASD was limited by noise from measurement electronics and vibrations of free-space optics, we adopted the noise model of $2 \cdot 10^{-3} + 3 \cdot 10^{-2} \cdot (1\,\mathrm{Hz}/f)^2\,\mathrm{Hz}/\sqrt{\mathrm{Hz}}$ for the ASD of fiber frequency noise.

F.2 Measurements on the VCOs

F.2.1 Actuation efficiency

Figure F.3 shows the measured relations between the input voltage to the VCO and the output frequency. When used in the ALS system, the operation point of the VCOs were set to around 2 V. Actuation efficiencies around there was 0.42(1) MHz/V and 0.43(1) MHz/V for the X and Y arms, respectively.

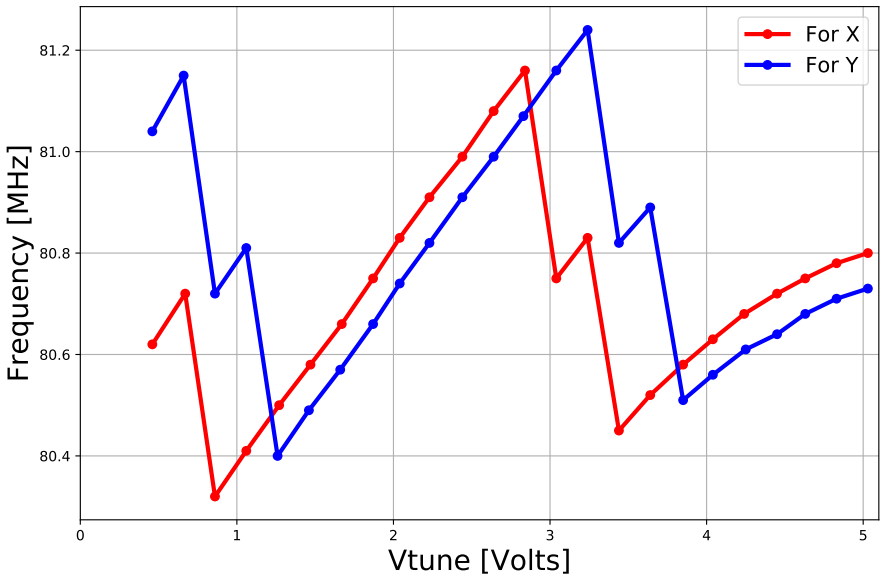

Figure F.3: Measured VCO responses to the input voltage. The red line shows the response of the VCO for the X arm PDH loop, while the blue one is for the Y arm PDH loop.

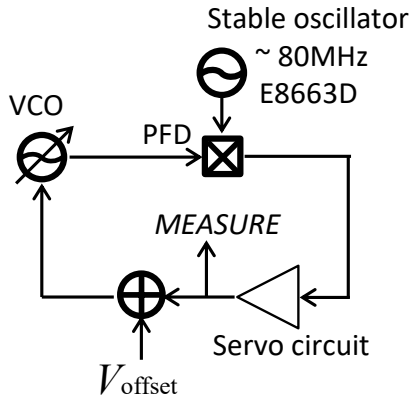

Figure F.4: Setup for the measurement of the VCO frequency noise.

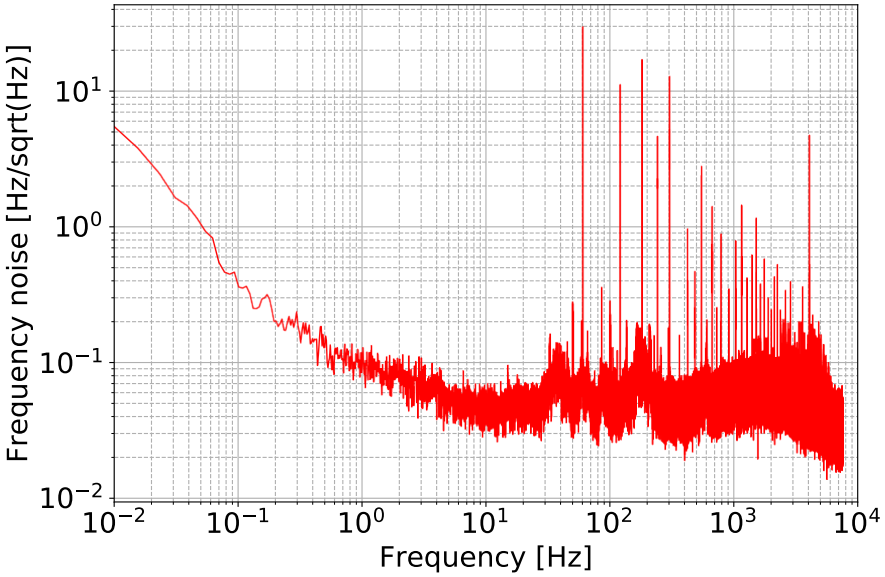

Figure F.5: Measured ASD of the output of the VCO.

F.2.2 Frequency noise of the output signal

Figure F.4 shows the experimental setup for the measurement of the output frequency noise of the VCO. The output of the VCO was demodulated at a phase-frequency discriminator by a stable sinusoidal signal at $\sim 80\,\mathrm{MHz}$. After processed by an analogue filter, the demodulated signal was fed back to the input of the VCO to close the PLL. From the feedback signal, the frequency fluctuations of the VCO output were measured, with respect to the stable oscillator output. This measurement was done for the VCO for the X arm as a representative. Figure F.5 shows the result.

Appendix G
LIST OF DEVICES

Table G.1: List of devices (optics) [164].

Device	Name	Note
Mirror (1064 nm)	PYD-10	Autex
Mirror (532 nm)	10D20DM.11	Newport
	05D20DM.11	Newport
HWP[a] (1064 nm)	WPH05M-1064	Thorlabs
HWP[a] (532 nm)	ZOWP-532-15mm-2-mntd	Autex
	WPH10M-532	Thorlabs
QWP[b] (532 nm)	ZOWP-532-15mm-4-mntd	Autex
	WPQ10M-532	Thorlabs
PBS[c] (1064 nm)	PBS-20-10640	Opto Sigma
PBS[c] (532 nm)	PBS-20-5320	Cube type, Opto Sigma
	PBSW-532	Plate type, Thorlabs
BS (532 nm)	BSX10	Plate type, Thorlabs
Dichroic mirror	DRX-1064/532-45P-UF-2038	In-air, LEO[d]
	TFVMQ-50.8C10-20-W1D -532/1064-ARS-30-45D	In-vacuum, Opto Sigma
HBS[e]	LWP-45-R532-T1064-UF-2038	LEO[d]
lens (1064 nm)	N-BK7 Plano-Convex C-series	Thorlabs
lens (532 nm)	N-BK7 Plano-Convex A-series	Thorlabs
FI[f] (1064 nm)	IO-5-1064-HP	Thorlabs
FI[f] (532 nm)	IO-5-532-HP	Thorlabs
Optical fiber	PM-S405-XP	Nufern
Fiber coupler	PAF-X-5-A	Thorlabs

[a] half-wave plate, [b] quarter-wave plate, [c] polarizing beam splitter, [d] Lattice Electro Optics Inc., [e] harmonic beam splitter, [f] Faraday isolator

Table G.2: List of devices (opto-electronics) [164].

Device	Name	Note
EOM[g] (532 nm)	EO-T38M3-VIS	CUBIC
AOM[h] (532 nm)	3080-125	Crystal Technology
PD[i] (PLL, 1064 nm)	818-BB-21A	Newport
PD[i] (PDH, 532 nm)	KAGRA RFPD [157]	Special made (Figure G.1)
PD[i] (DC, 1064/532 nm)	PDA100A	For fiber noise loops, Thorlabs
	PDA100A-2	For fiber noise loops, Thorlabs

[g] electro-optical modulator, [h] acousto-optical modulator, [i] photodetector

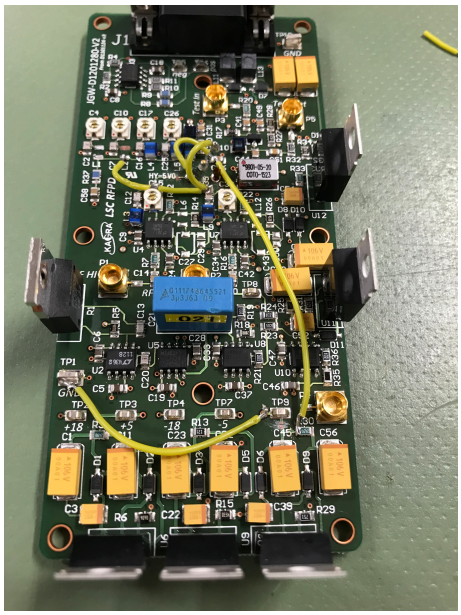

Figure G.1: Picture of special modifications on the RF PDs for the arm PDH sensing. The modifications were needed because the pin assignment of the photodetector used in the ordinary version is different from that in this special version.

Table G.3: List of devices (opto-mechanics).

Device	Name	Note
Picomotor-actuated mirror mount	8822	In air, Newport
	8822-UHV	In vacuum, Newport
Piezoelectric transducer	PC4QR	Thorlabs

Table G.4: List of devices (Electronics).

Device	Name	Note
PFD[j]	Special made [185]	
Demodulator	I&Q demodulator [186]	High-bandwidth version
Servo circuit	Common mode servo [187]	
VCO[k]	Special made	Prototype version (Figure G.2)
Signal generator	E8663D	For PLL, Keysight
	N5181B	For PDH, Keysight
	33611A-OCX	For VCO reference, Keysight
Piezo driver	MDT693B	Thorlabs

[j] phase-frequency discriminator, [k] voltage-controlled oscillator

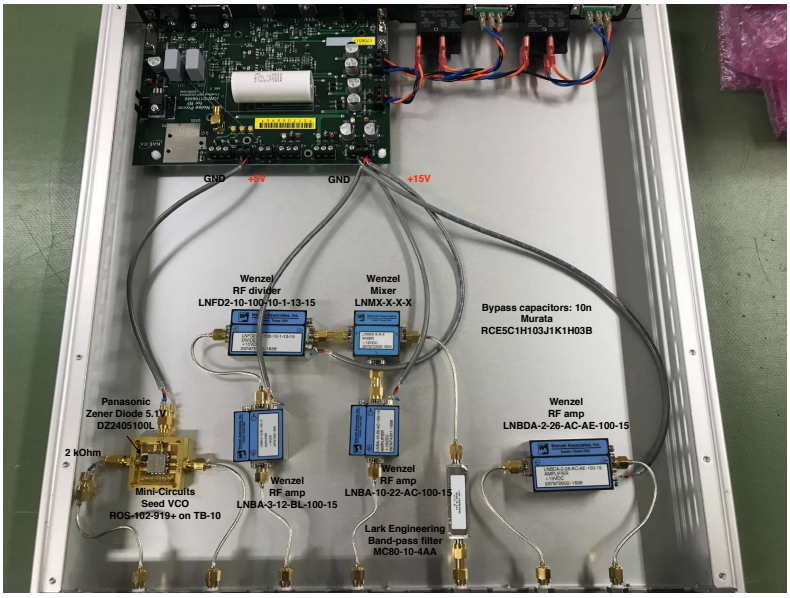

Figure G.2: Top view of the prototype low noise VCO circuit.

BIBLIOGRAPHY

[1] A. Einstein, *Näherungsweise Integration der Feldgleichungen der Gravitation.* Sitzungsber. K. Preuss. Akad. Wiss., **1** 688, (1916).

[2] A. Einstein, *Über Gravitationswellen.* Sitzungsber. K. Preuss. Akad. Wiss., **1** 154, (1918).

[3] J. D. Creighton and W. G. Anderson. *Gravitational-Wave Physics and Astronomy.* John Wiley & Sons, (2012).

[4] M. Maggiore. *Gravitational Waves. Vol.1, Theory and Experiments.* Oxford Univ. Press, (2008).

[5] B. P. Abbott *et al.* , *Observation of Gravitational Waves from a Binary Black Hole Merger.* Phys. Rev. Lett., **116** 061102, (2016).

[6] B. P. Abbott *et al.* , *GW170817: Observation of Gravitational Waves from a Binary Neutron Star Inspiral.* Physical Review Letters, **119**(16) 161101, (2017).

[7] M. Punturo *et al.* , *The Einstein Telescope: A third-generation gravitational wave observatory.* Classical and Quantum Gravity, **27**(19) 194002, (2010).

[8] B. P. Abbott *et al.* , *Exploring the sensitivity of next generation gravitational wave detectors.* Classical and Quantum Gravity, **34**(4) 044001, (2017).

[9] B. P. Abbott *et al.* , *GWTC-1: A Gravitational-Wave Transient Catalog of Compact Binary Mergers Observed by LIGO and Virgo during the First and Second Observing Runs.* Physical Review X, **9**(3) 031040, (2019).

[10] J. M. Corral-Santana *et al.* , *BlackCAT: A catalogue of stellar-mass black holes in X-ray transients.* Astronomy & Astrophysics, **587** A61, (2016).

[11] LIGO Scientific Collaboration, Virgo Collaboration, Fermi Gamma-Ray Burst Monitor, and INTEGRAL, *Gravitational Waves and Gamma-rays from a Binary Neutron Star Merger: GW170817 and GRB 170817A*. The Astrophysical Journal Letters, **848**(2) L13, (2017).

[12] T. Hinderer, B. D. Lackey, R. N. Lang, and J. S. Read, *Tidal deformability of neutron stars with realistic equations of state and their gravitational wave signatures in binary inspiral*. Physical Review D, **81**(12) 123016, (2010).

[13] K. Hotokezaka, K. Kyutoku, Y.-i. Sekiguchi, and M. Shibata, *Measurability of the tidal deformability by gravitational waves from coalescing binary neutron stars*. Physical Review D, **93**(6) 064082, (2016).

[14] C. D. Ott, *The gravitational-wave signature of core-collapse supernovae*. Classical and Quantum Gravity, **26**(6) 063001, (2009).

[15] V. Roma, J. Powell, I. S. Heng, and R. Frey, *Astrophysics with core-collapse supernova gravitational wave signals in the next generation of gravitational wave detectors*. Physical Review D, **99**(6) 063018, (2019).

[16] J. Meidam, M. Agathos, C. Van Den Broeck, J. Veitch, and B. S. Sathyaprakash, *Testing the no-hair theorem with black hole ringdowns using TIGER*. Physical Review D, **90**(6) 064009, (2014).

[17] H. Takeda *et al.* , *Prospects for gravitational-wave polarization tests from compact binary mergers with future ground-based detectors*. Physical Review D, **100**(4) 042001, (2019).

[18] J. Aasi *et al.* , *Advanced LIGO*. Classical and Quantum Gravity, **32**(7) 074001, (2015).

[19] F. Acernese *et al.* , *The Advanced Virgo detector*. Journal of Physics: Conference Series, **610** 012014, (2015).

[20] K. Somiya, *Detector configuration of KAGRA–the Japanese cryogenic gravitational-wave detector*. Classical and Quantum Gravity, **29**(12) 124007, (2012).

[21] K. Izumi *et al.* , *Multicolor cavity metrology*. Journal of the Optical Society of America A, **29**(10) 2092, (2012).

[22] A. Staley *et al.* , *Achieving resonance in the Advanced LIGO gravitational-wave interferometer.* Classical and Quantum Gravity, **31**(24) 245010, (2014).

[23] KAGRA Collaboration, LIGO Scientific Collaboration and Virgo Collaboration *et al.* , *Prospects for observing and localizing gravitational-wave transients with Advanced LIGO, Advanced Virgo and KAGRA.* Living Reviews in Relativity, **21**(1) 3, (2018).

[24] T. Akutsu *et al.* , *Construction of KAGRA: An underground gravitational-wave observatory.* Prog. Theor. Exp. Phys., **2018**(1) 013F01, (2018).

[25] T. Akutsu *et al.* , *First cryogenic test operation of underground km-scale gravitational-wave observatory KAGRA.* Classical and Quantum Gravity, **36**(16) 165008, (2019).

[26] R. A. Hulse and J. H. Taylor, *Discovery of a pulsar in a binary system.* The Astrophysical Journal, **195** L51, (1975).

[27] J. H. Taylor and J. M. Weisberg, *A new test of general relativity - Gravitational radiation and the binary pulsar PSR 1913+16.* The Astrophysical Journal, **253** 908, (1982).

[28] B. P. Abbott *et al.* , *GW170814: A Three-Detector Observation of Gravitational Waves from a Binary Black Hole Coalescence B.* Physical Review Letters, **119**(14) 1–16, (2017).

[29] W. M. Farr *et al.* , *Distinguishing spin-aligned and isotropic black hole populations with gravitational waves.* Nature, **548**(7668) 426–429, (2017).

[30] B. P. Abbott *et al.* , *Binary Black Hole Population Properties Inferred from the First and Second Observing Runs of Advanced LIGO and Advanced Virgo.* The Astrophysical Journal, **882**(2) L24, (2019).

[31] D. Gerosa and E. Berti, *Are merging black holes born from stellar collapse or previous mergers?* Physical Review D, **95**(12) 124046, (2017).

[32] M. Zevin *et al.* , *Constraining Formation Models of Binary Black Holes with Gravitational-wave Observations.* The Astrophysical Journal, **846**(1) 82, (2017).

[33] B. P. Abbott *et al.* , *Multi-messenger Observations of a Binary Neutron Star Merger*. The Astrophysical Journal Letters, **848**(2) L12, (2017).

[34] A. Goldstein *et al.* , *An Ordinary Short Gamma-Ray Burst with Extraordinary Implications:* Fermi *-GBM Detection of GRB 170817A*. The Astrophysical Journal, **848**(2) L14, (2017).

[35] V. A. Villar *et al.* , *The Combined Ultraviolet, Optical, and Near-infrared Light Curves of the Kilonova Associated with the Binary Neutron Star Merger GW170817: Unified Data Set, Analytic Models, and Physical Implications*. The Astrophysical Journal, **851**(1) L21, (2017).

[36] B. S. Sathyaprakash and B. F. Schutz, *Physics, astrophysics and cosmology with gravitational waves*. Living Reviews in Relativity, **12**, (2009).

[37] C. D. Ott, *Probing the core-collapse supernova mechanism with gravitational waves*. Classical and Quantum Gravity, **26**(20) 204015, (2009).

[38] B. P. Abbott *et al.* , *Searches for Gravitational Waves from Known Pulsars at Two Harmonics in 2015–2017 LIGO Data*. The Astrophysical Journal, **879**(1) 10, (2019).

[39] S. M. Koushiappas and A. R. Zentner, *Testing Models of Supermassive Black Hole Seed Formation through Gravity Waves*. The Astrophysical Journal, **639**(1) 7–22, (2006).

[40] C. Caprini and D. G. Figueroa, *Cosmological backgrounds of gravitational waves*. Classical and Quantum Gravity, **35**(16) 163001, (2018).

[41] H. Yu *et al.* , *Prospects for Detecting Gravitational Waves at 5 Hz with Ground-Based Detectors*. Physical Review Letters, **120**(14) 141102, (2018).

[42] P. Amaro-Seoane, *Laser Interferometer Space Antenna*, (2017). arxiv:1702.00786.

[43] S. Kawamura *et al.* , *The Japanese space gravitational wave antenna—DECIGO*. Classical and Quantum Gravity, **23**(8) S125–S131, (2006).

[44] J. Weber, *Gravitational-Wave-Detector Events*. Physical Review Letters, **20**(23) 1307–1308, (1968).

[45] O. D. Aguiar, *Past, present and future of the Resonant-Mass gravitational wave detectors.* Research in Astronomy and Astrophysics, **11**(1) 1–42, (2011).

[46] M. Ando *et al.* , *Torsion-Bar Antenna for Low-Frequency Gravitational-Wave Observations.* Physical Review Letters, **105**(16) 161101, (2010).

[47] S. Dimopoulos, P. W. Graham, J. M. Hogan, M. A. Kasevich, and S. Rajendran, *Atomic gravitational wave interferometric sensor.* Physical Review D, **78**(12) 122002, (2008).

[48] B. Canuel *et al.* , *Exploring gravity with the MIGA large scale atom interferometer.* Scientific Reports, **8**(1) 14064, (2018).

[49] M.-S. Zhan *et al.* , *ZAIGA: Zhaoshan long-baseline atom interferometer gravitation antenna.* International Journal of Modern Physics D, page 1940005, (2019).

[50] D. Gao, J. Wang, and M. Zhan, *Atomic Interferometric Gravitational-wave Space Observatory (AIGSO).* Communications in Theoretical Physics, **69**(1) 37, (2018).

[51] W. Qin, K. K. Boddy, M. Kamionkowski, and L. Dai, *Pulsar-timing arrays, astrometry, and gravitational waves.* Physical Review D, **99**(6) 063002, (2019).

[52] C. J. Moore, S. R. Taylor, and J. R. Gair, *Estimating the sensitivity of pulsar timing arrays.* Classical and Quantum Gravity, **32**(5) 055004, (2015).

[53] R. Weiss, *Electromagnetically Coupled Broadband Gravitational Antenna*, (1972). LIGO DCC, P720002-01-R.

[54] H. Takeda *et al.* , *Polarization test of gravitational waves from compact binary coalescences.* Physical Review D, **98**(2) 022008, (2018).

[55] G. Losurdo *et al.* , *An inverted pendulum preisolator stage for the VIRGO suspension system.* Review of Scientific Instruments, **70**(5) 2507–2515, (1999).

[56] G. Cella, V. Sannibale, R. DeSalvo, S. Márka, and A. Takamori, *Monolithic geometric anti-spring blades.* Nuclear Instruments and Methods in Physics Research Section A: Accelerators, Spectrometers, Detectors and Associated Equipment, **540**(2-3) 502–519, (2005).

[57] C. Gardiner and M. Collett, *Input and output in damped quantum systems: Quantum stochastic differential equations and the master equation.* Physical Review A, **31**(6) 3761–3774, (1985).

[58] Y. Levin, *Internal thermal noise in the LIGO test masses: A direct approach.* Physical Review D, **57** 659, (1998).

[59] K. Komori *et al.* , *Direct approach for the fluctuation-dissipation theorem under nonequilibrium steady-state conditions.* Physical Review D, **97**(10) 102001, (2018).

[60] T. Uchiyama *et al.* , *Reduction of Thermal Fluctuations in a Cryogenic Laser Interferometric Gravitational Wave Detector.* Physical Review Letters, **108**(14) 141101, (2012).

[61] F. Acernese *et al.* , *Advanced Virgo: A second-generation interferometric gravitational wave detector.* Classical and Quantum Gravity, **32**(2) 024001, (2015).

[62] C. M. Caves, *Quantum-Mechanical Radiation-Pressure Fluctuations in an Interferometer.* Physical Review Letters, **45**(2) 75–79, (1980).

[63] E. Oelker *et al.* , *Audio-Band Frequency-Dependent Squeezing for Gravitational-Wave Detectors.* Physical Review Letters, **116**(4) 041102, (2016).

[64] E. Capocasa *et al.* , *Measurement of optical losses in a high-finesse 300 m filter cavity for broadband quantum noise reduction in gravitational-wave detectors.* Physical Review D, **98**(2) 022010, (2018).

[65] J. Cripe *et al.* , *Radiation-pressure-mediated control of an optomechanical cavity.* Physical Review A, **97**(1) 013827, (2018).

[66] M. J. Yap *et al.* , *Broadband reduction of quantum radiation pressure noise via squeezed light injection.* Nature Photonics, (2019).

[67] K. Komori, *Optomechanical Torsion Pendulum for Measurement of Quantum Radiation Pressure Fluctuation.* Ph.D. thesis, Univ. of Tokyo, Tokyo, (2019).

[68] K. Nagano, Y. Enomoto, M. Nakano, A. Furusawa, and S. Kawamura, *Mitigation of radiation-pressure-induced angular instability of a Fabry–Perot cavity consisting of suspended mirrors.* Physics Letters A, **11**(12) 261–5, (2016).

[69] H. Miao, R. X. Adhikari, Y. Ma, B. Pang, and Y. Chen, *Towards the Fundamental Quantum Limit of Linear Measurements of Classical Signals.* Physical Review Letters, **119**(5) 1–6, (2017).

[70] B. Pang and Y. Chen, *Fundamental relations between measurement, radiation, and decoherence in gravitational wave laser interferometer detectors.* Physical Review D, **99**(12) 124016, (2019).

[71] B. P. Abbott *et al.* , *Tests of General Relativity with GW150914.* Physical Review Letters, **116**(22) 221101, (2016).

[72] M. Isi, M. Giesler, W. M. Farr, M. A. Scheel, and S. A. Teukolsky, *Testing the No-Hair Theorem with GW150914.* Physical Review Letters, **123**(11) 111102, (2019).

[73] P. S. Cowperthwaite *et al.* , *The Electromagnetic Counterpart of the Binary Neutron Star Merger LIGO/Virgo GW170817. II. UV, Optical, and Near-infrared Light Curves and Comparison to Kilonova Models.* The Astrophysical Journal, **848**(2) L17, (2017).

[74] D. Kasen, B. Metzger, J. Barnes, E. Quataert, and E. Ramirez-Ruiz, *Origin of the heavy elements in binary neutron-star mergers from a gravitational-wave event.* Nature, **551**(7678) 80–84, (2017).

[75] M. Nicholl *et al.* , *The Electromagnetic Counterpart of the Binary Neutron Star Merger LIGO/Virgo GW170817. III. Optical and UV Spectra of a Blue Kilonova from Fast Polar Ejecta.* The Astrophysical Journal, **848**(2) L18, (2017).

[76] B. P. Abbott *et al.* , *A gravitational-wave standard siren measurement of the Hubble constant.* Nature, **551** 85–88, (2017).

[77] K. Hotokezaka *et al.* , *A Hubble constant measurement from superluminal motion of the jet in GW170817.* Nature Astronomy, (2019).

[78] *Updated Advanced LIGO sensitivity design curve*, (2018). Data from LIGO DCC, T1800044-v5.

[79] *Prospects for observing and localizing gravitational-wave transients with advanced LIGO, advanced virgo and KAGRA*, (2018). Data from LIGO DCC, P1200087-v47.

[80] *Latest estimated sensitivity of KAGRA*, (2017). Data from JGWdoc, T1707038-v9.

[81] A. Abramovici *et al.* , *LIGO: The Laser Interferometer Gravitational-Wave Observatory*. Science, **256**(5055) 325–333, (1992).

[82] B. P. Abbott *et al.* , *LIGO: The Laser Interferometer Gravitational-Wave Observatory*. Reports on Progress in Physics, **72**(7) 076901, (2009).

[83] C. S. Unnikrishnan, *IndIGO AND LIGO-INDIA: SCOPE AND PLANS FOR GRAVITATIONAL WAVE RESEARCH AND PRECISION METROLOGY IN INDIA*. International Journal of Modern Physics D, **22**(01) 1341010, (2013).

[84] *India Approves Construction of Third LIGO Observatory!*, Web page. https://www.ligo.caltech.edu/news/ligo20160217.

[85] LLO aLIGO logbook 46825. Technical report, (2019). https://alog.ligo-la.caltech.edu/aLOG/index.php?callRep=46825.

[86] T. Accadia *et al.* , *Virgo: A laser interferometer to detect gravitational waves*. Journal of Instrumentation, **7**(03) P03012–P03012, (2012).

[87] N. Tominaga *et al.* , *Subaru Hyper Suprime-Cam Survey for an optical counterpart of GW170817‡*. Publications of the Astronomical Society of Japan, **70**(2), (2018).

[88] L. Wen and Y. Chen, *Geometrical expression for the angular resolution of a network of gravitational-wave detectors*. Physical Review D, **81**(8) 082001, (2010).

[89] S. Hild *et al.* , *Sensitivity studies for third-generation gravitational wave observatories*. Classical and Quantum Gravity, **28**(9) 094013, (2011).

[90] M. A. Bizouard, *LIGO-Virgo status: O3 observing run and beyond*. Presented at Transient Sky 2020, Paris, France, (2019).

[91] S. Haino and Y.-J. Huang, *O3 simulation (N=2, 3, 4 cases)*, (2019). JGWdoc, JGW-G1910190-v14.

[92] M. Punturo, *ET letter of intent*, Web page, (2018). http://www.et-gw.eu/index.php/letter-of-intent.

[93] D. Reitze *et al.* , *Cosmic Explorer: The U.S. Contribution to Gravitational-Wave Astronomy beyond LIGO*, (2019). arxiv:1907.04833.

[94] D. Lai, F. A. Rasio, and S. L. Shapiro, *Hydrodynamic Instability and Coalescence of Binary Neutron Stars*. The Astrophysical Journal, **420** 811, (1994).

[95] E. R. Most, L. R. Weih, L. Rezzolla, and J. Schaffner-Bielich, *New Constraints on Radii and Tidal Deformabilities of Neutron Stars from GW170817*. Physical Review Letters, **120**(26) 261103, (2018).

[96] K. Hotokezaka *et al.* , *Remnant massive neutron stars of binary neutron star mergers: Evolution process and gravitational waveform*. Physical Review D, **88**(4) 044026, (2013).

[97] H. Yang *et al.* , *Gravitational wave spectroscopy of binary neutron star merger remnants with mode stacking*. Physical Review D, **97**(2) 024049, (2018).

[98] D. M. Eardley, D. L. Lee, and A. P. Lightman, *Gravitational-Wave Observations as a Tool for Testing Relativistic Gravity*. Physical Review D, **8**(10) 3308–3321, (1973).

[99] D. M. Eardley, D. L. Lee, A. P. Lightman, R. V. Wagoner, and C. M. Will, *Gravitational-Wave Observations as a Tool for Testing Relativistic Gravity*. Physical Review Letters, **30**(18) 884–886, (1973).

[100] Planck Collaboration *et al.* , Planck *2015 results: XIII. Cosmological parameters*. Astronomy & Astrophysics, **594** A13, (2016).

[101] A. G. Riess *et al.* , *A 2.4% Determination of the Local Value of the Hubble Constant*. The Astrophysical Journal, **826**(1) 56, (2016).

[102] B. F. Schutz, *Determining the Hubble constant from gravitational wave observations*. Nature, **323**(6086) 310–311, (1986).

[103] J. Mendonça and R. Sturani, *Cosmological model selection from standard siren detections by third generation gravitational wave obervatories*. arXiv:1905.03848 [astro-ph, physics:gr-qc], (2019).

[104] X.-N. Zhang, L.-F. Wang, J.-F. Zhang, and X. Zhang, *Improving cosmological parameter estimation with the future gravitational-wave standard siren observation from the Einstein Telescope*. Physical Review D, **99**(6) 063510, (2019).

[105] M. Du, W. Yang, L. Xu, S. Pan, and D. F. Mota, *Future constraints on dynamical dark-energy using gravitational-wave standard sirens*. Physical Review D, **100**(4) 043535, (2019).

[106] *Unofficial sensitivity curves (ASD) for aLIGO, kagra, virgo, voyager, cosmic explorer and ET*, (2015). Data from LIGO DCC, T1500293-v12.

[107] T. T. Fricke *et al.* , *DC readout experiment in Enhanced LIGO*. Classical and Quantum Gravity, **29**(6) 065005, (2012).

[108] H. J. Kimble, Y. Levin, A. B. Matsko, K. S. Thorne, and S. P. Vyatchanin, *Conversion of conventional gravitational-wave interferometers into quantum nondemolition interferometers by modifying their input and/or output optics*. Physical Review D, **65**(2) 022002, (2002).

[109] J. Miller *et al.* , *Prospects for doubling the range of Advanced LIGO*. Physical Review D, **91**(6) 062005, (2015).

[110] LIGO Scientific Collaboration, *Instrument Science White Paper 2018*, (2018). LIGO DCC, T1800133–v3.

[111] L. Schnupp, *Internal modulation schemes*. Presneted at European Collaboration Meeting on Interferometric Detection of Gravitational Waves, Sorrento, Italy, (1988).

[112] R. W. P. Drever *et al.* , *Laser phase and frequency stabilization using an optical resonator*. Applied Physics B Photophysics and Laser Chemistry, **31**(2) 97–105, (1983).

[113] B. J. Meers, *Recycling in laser-interferometric gravitational-wave detectors*. Physical Review D, **38**(8) 2317–2326, (1988).

[114] J. Mizuno *et al.* , *Resonant sideband extraction: A new configuration for interferometric gravitational wave detectors*. Physics Letters A, **175**(5) 273–276, (1993).

[115] D. Walls, *Squeezed states of light*. Nature, **306**(10) 141–146, (1983).

[116] M. Tse *et al.* , *Quantum-Enhanced Advanced LIGO Detectors in the Era of Gravitational-Wave Astronomy.* Physical Review Letters, **123**(23) 231107, (2019).

[117] F. Acernese *et al.* , *Increasing the Astrophysical Reach of the Advanced Virgo Detector via the Application of Squeezed Vacuum States of Light.* Physical Review Letters, **123**(23) 231108, (2019).

[118] J. Degallaix, *Adv+.* Presented at Gravitational Wave Advanced Detector Workshop 2019, Elba Island, Italy, (2019).

[119] A. Buonanno and Y. Chen, *Quantum noise in second generation, signal-recycled laser interferometric gravitational-wave detectors.* Physical Review D, **64**(4) 1–21, (2001).

[120] A. Buonanno and Y. Chen, *Scaling law in signal recycled laser-interferometer gravitational-wave detectors.* Physical Review D, **67**(6) 062002, (2003).

[121] Z. Li, R. Bennett, and G. Stedman, *Swept-frequency induced optical cavity ringing.* Optics Communications, **86**(1) 51–57, (1991).

[122] J. Poirson, F. Bretenaker, M. Vallet, and A. Le Floch, *Analytical and experimental study of ringing effects in a Fabry–Perot cavity Application to the measurement of high finesses.* Journal of the Optical Society of America B, **14**(11) 2811, (1997).

[123] M. Rakhmanov, R. L. Savage, D. H. Reitze, and D. B. Tanner, *Dynamic resonance of light in Fabry-Perot cavities.* Physics Letters, Section A: General, Atomic and Solid State Physics, **305**(5) 239–244, (2002).

[124] M. Ando, *Power Recycling for an Interferometric Gravitational Wave Detector.* Ph.D. thesis, Univ. of Tokyo, (1998).

[125] K. Arai and TAMA Collaboration, *Sensing and controls for power-recycling of TAMA300.* Classical and Quantum Gravity, **19**(7) 1843–1848, (2002).

[126] M. Evans *et al.* , *Lock acquisition of a gravitational-wave interferometer.* Optics Letters, **27**(8) 598, (2002).

[127] F. Acernese *et al.* , *The variable finesse locking technique.* Classical and Quantum Gravity, **23**(8) S85–S89, (2006).

[128] A. J. Mullavey *et al.* , *Arm-length stabilisation for interferometric gravitational-wave detectors using frequency-doubled auxiliary lasers*. Optics Express, **20**(1) 81, (2012).

[129] T. Akutsu *et al.* , *An arm length stabilization system for KAGRA and future gravitational-wave detectors*, (2019). arxiv:1910.00955, Accepted by Classical and Quantum Gravity.

[130] L. Barsotti, *The Control of the Virgo Interferometer for Gravitational Wave Detection*. Ph.D. thesis, University of Pisa, (2006).

[131] D. A. Shaddock, *Digitally enhanced heterodyne interferometry*. Optics Letters, **32**(22) 3355, (2007).

[132] O. P. Lay, S. Dubovitsky, D. A. Shaddock, and B. Ware, *Coherent range-gated laser displacement metrology with compact optical head*. Optics Letters, **32**(20) 2933, (2007).

[133] M. Mantovani, Personal communication, (2019).

[134] A. Staley, K. Izumi, and S. Ballmer, *ALS Noise Measurements and Model for HIFO-Y*, (2013). LIGO DCC, LIGO-T1300688.

[135] D. Martynov, *Lock Acquisition and Sensitivity Analysis of Advanced LIGO Interferometers*. Ph.D. thesis, (2015).

[136] K. Okutomi, *Development of 13.5-Meter-Tall Vibration Isolation System for the Main Mirrors in KAGRA*. Ph.D. thesis, SOKENDAI University, Kanagawa, (2019).

[137] T. Sekiguchi, *A Study of Low Frequency Vibration Isolation System for Large Scale Gravitational Wave Detectors*. Ph.D. thesis, The University of Tokyo, (2015).

[138] Y. Akiyama *et al.* , *Vibration isolation system with a compact damping system for power recycling mirrors of KAGRA*. Classical and Quantum Gravity, **36**(9) 095015, (2019).

[139] M. Nakano, *Development of input optics for the gravitational wave detector KAGRA*. Ph.D. thesis, The University of Tokyo, (2018).

[140] K. Yamamoto *et al.* , *Design and experimental demonstration of a laser modulation system for future gravitational-wave detectors*. Classical and Quantum Gravity, **36** 205009, (2019).

[141] Y. Aso *et al.* , *Interferometer design of the KAGRA gravitational wave detector*. Physical Review D, **88**(4) 043007, (2013).

[142] Y. Enomoto and Y. Miyazaki. KAGRA logbook 7332. Technical report, (2018). http://klog.icrr.u-tokyo.ac.jp/osl/?r=7332.

[143] Y. Enomoto. KAGRA logbook 9505. Technical report, (2019). http://klog.icrr.u-tokyo.ac.jp/osl/?r=9505.

[144] T. Yokozawa and Y. Enomoto. KAGRA logbook 9052, 9211, 9496. Technical report, (2019). http://klog.icrr.u-tokyo.ac.jp/osl/?r=9052, http://klog.icrr.u-tokyo.ac.jp/osl/?r=9211, http://klog.icrr.u-tokyo.ac.jp/osl/?r=9496.

[145] *Optical parameters*, Web page. http://gwwiki.icrr.u-tokyo.ac.jp/JGWwiki/LCGT/subgroup/ifo/MIF/OptParam, visited in 2019.

[146] E. Hirose, Personal communication, (2019), Reflectivity of each test mass at 532 nm was given.

[147] Y. Enomoto, M. Nakano, and K. Kokeyama. KAGRA logbook 9276. Technical report, (2019). http://klog.icrr.u-tokyo.ac.jp/osl/?r=9276.

[148] E. Capocasa, Y. Enomoto, and S. Ballmer. KAGRA logbook 9246. Technical report, (2019). http://klog.icrr.u-tokyo.ac.jp/osl/?r=9246.

[149] Y. Enomoto and T.-L. T. Tsang. KAGRA logbook 9073. Technical report, (2019). http://klog.icrr.u-tokyo.ac.jp/osl/?r=9073.

[150] *IOO optical parameters*, Web page. http://gwwiki.icrr.u-tokyo.ac.jp/JGWwiki/KAGRA/Subgroups/IOO/OptParam, visited in 2019.

[151] Y. Michimura. KAGRA logbook 618. Technical report, (2016). http://klog.icrr.u-tokyo.ac.jp/osl/?r=618.

[152] K. Miyo, *Seismic noise of KAGRA mine*, (2019). JGWdoc, JGW-T1910436-v5 (Internal).

[153] S. Nagano *et al.* , *Development of a multistage laser frequency stabilization for an interferometric gravitational-wave detector*. Review of Scientific Instruments, **74**(9) 4176–4183, (2003).

[154] *Green Lock Noise Budget*, Web page. https://granite.phys.s.u-tokyo.ac.jp/svn/LCGT/trunk/kagranoisebudget/GreenLock/.

[155] D. Sigg, *Low noise VCO specifications*, (2011). LIGO DCC, E1101019-v1.

[156] N. Uehara and K. Ueda, *Ultrahigh-frequency stabilization of a diode-pumped Nd : YAG laser with a high-power-acceptance photodetector*. **19**(10) 728–730, (1994).

[157] Y. Aso and M. Kamiizumi, *KAGRA LSC RFPD*, (2012). JGWdoc, JGW-D1201280-v2 (Internal).

[158] Keysight Technologies, *Keysight E8663D PSG RF Analog Signal Generator data sheet*. http://literature.cdn.keysight.com/litweb/pdf/5990-4136EN.pdf, visited in 2019.

[159] Y. Enomoto and K. Shimode. KAGRA logbook 9550. Technical report, (2019). http://klog.icrr.u-tokyo.ac.jp/osl/?r=9550.

[160] Y. Enomoto, *Polarization issue in the central IFO*, (2019). JGWdoc, JGW-G1910388-v1.

[161] M. Leonardi, *MIR subsystem report*, (2019). JGWdoc, JGW-G1910635-v1 (Internal).

[162] A. Staley, *Locking the Advanced LIGO Gravitational Wave Detector : With a Focus on the Arm Length Stabilization Technique*. Ph.D. thesis, Columbia University, (2015).

[163] Y. Enomoto. KAGRA logbook 7265. Technical report, (2018). http://klog.icrr.u-tokyo.ac.jp/osl/?r=7265.

[164] K. Yokogawa. *Development of interferometer control system with green lasers in KAGRA*. Master's thesis, University of Toyama, (2019). Written in Japanese.

[165] R. Sugimoto. *Development of Auxiliary Locking System in Gravitational Wave Telescope KAGRA*. Master's thesis, University of Toyama, (2020). Written in Japanese, in preparation.

[166] S. F. Clifford, G. M. B. Bouricius, G. R. Ochs, and M. H. Ackley, *Phase Variations in Atmospheric Optical Propagation.* Journal of the Optical Society of America, **61**(10) 1279, (1971).

[167] L. C. Sinclair *et al.* , *Optical phase noise from atmospheric fluctuations and its impact on optical time-frequency transfer.* Physical Review A, **89**(2) 023805, (2014).

[168] J.-M. Conan, G. Rousset, and P.-Y. Madec, *Wave-front temporal spectra in high-resolution imaging through turbulence.* Journal of the Optical Society of America A, **12**(7) 1559, (1995).

[169] T. Akutsu and K. Kokeyama. KAGRA logbook 3352. Technical report, (2017). http://klog.icrr.u-tokyo.ac.jp/osl/?r=3352.

[170] S. Miyoki, Personal communication, (2019).

[171] J. Komma, *Optische Eigenschaften von Substratmaterialien Für Zukünftige Kryogene Gravitationswellendetektoren.* Ph.D. thesis, Jena, Jena, (2016).

[172] T. Udem, R. Holzwarth, and T. W. Hänsch, *Optical frequency metrology.* Nature, **416** 233–237, (2002).

[173] D. J. Jones, *Carrier-Envelope Phase Control of Femtosecond Mode-Locked Lasers and Direct Optical Frequency Synthesis.* Science, **288**(5466) 635–639, (2000).

[174] R. Holzwarth *et al.* , *Optical Frequency Synthesizer for Precision Spectroscopy.* Physical Review Letters, **85**(11) 2264–2267, (2000).

[175] Menlo Systems, *FC1500-250-ULN.* https://www.menlosystems.com/assets/datasheets/Optical-Frequency-Combs/Menlo_FC1500-250-ULN_D-EN_2019-08-02_3w.pdf, visited in 2019.

[176] T. Ushiba, *Laser Frequency Stabilization with a Cryogenic Optical Cavity.* Ph.D. thesis, Univ. of Tokyo, (2015).

[177] D. Yeaton-Massey and R. X. Adhikari, *A new bound on excess frequency noise in second harmonic generation in PPKTP at the 10^-19 level.* Optics Express, **20**(19) 21019, (2012).

[178] J. A. Giaime, *Studies of Laser Interferometer Design and a Vibration Isolation System for Interferometric Gravitational Wave Detectors*. Ph.D. thesis, Massachusetts Institute of Technology, (1995).

[179] R. Flaminio and H. Heitmann, *Longitudinal control of an interferometer for the detection of gravitational waves*. Physics Letters A, **214**(3-4) 112–122, (1996).

[180] D. Sigg, N. Mavalvala, J. Giaime, P. Fritschel, and D. Shoemaker, *Signal extraction in a power-recycled Michelson interferometer with Fabry–Perot arm cavities by use of a multiple-carrier frontal modulation scheme*. Applied Optics, **37**(24) 5687, (1998).

[181] J. S. Bendat and A. G. Piersol. *Random Data: Analysis and Measurement Procedures*. Wiley, (2010). The fourth edition.

[182] G. H. Fett. *Feedback Control Systems*. Prentice Hall, (1954).

[183] K. J. Blow, R. Loudon, and S. J. D. Phoenix, *Continuum fields in quantum optics*. Phys. Rev. A, **42**(7) 4102–4114, (1990).

[184] H. Miao, *Exploring Macroscopic Quantum Mechanics in Optomechanical Devices*. Ph.D. thesis, the University of Western Australia, (2010).

[185] K. Doi, *Phase Frequency Discriminator*, (2018). JGWdoc, JGW-D1809187-v3.

[186] Y. Aso and M. Kamiizumi, *I&Q demodulator board*, (2014). JGWdoc, JGW-D1402413-v1 (Internal).

[187] K. Awai, *CM servo board*, (2015). JGWdoc, JGW-D1503567-v4 (Internal).